

Computational Studies of Strongly Correlated Quantum Matter

Hao Shi

Rugao, China

Bachelor of Science, Nanjing University, 2008

A Dissertation presented to the Graduate Faculty  
of The College of William & Mary in Candidacy for the Degree of  
Doctor of Philosophy

Department of Physics

College of William & Mary  
May 2017

©2017  
Hao Shi  
All rights reserved.

## APPROVAL PAGE

This Dissertation is submitted in partial fulfillment of  
the requirements for the degree of

Doctor of Philosophy



Hao Shi

Approved by the Committee, March, 2017



Committee Chair

Professor Shiwei Zhang, Physics

College of William & Mary



Associate Professor Seth Aubin, Physics

College of William & Mary



Professor Henry Krakauer, Physics

College of William & Mary



Associate Professor Konstantinos Orginos, Physics

College of William & Mary



Professor Andreas Stathopoulos, Computer Science

College of William & Mary

## ABSTRACT

The study of strongly correlated quantum many-body systems is an outstanding challenge. Highly accurate results are needed for the understanding of practical and fundamental problems in condensed-matter physics, high energy physics, material science, quantum chemistry and so on. Our familiar mean-field or perturbative methods tend to be ineffective. Numerical simulations provide a promising approach for studying such systems. The fundamental difficulty of numerical simulation is that the dimension of the Hilbert space needed to describe interacting systems increases exponentially with the system size. Quantum Monte Carlo (QMC) methods are one of the best approaches to tackle the problem of enormous Hilbert space. They have been highly successful for boson systems and unfrustrated spin models. For systems with fermions, the exchange symmetry in general causes the infamous sign problem, making the statistical noise in the computed results grow exponentially with the system size. This hinders our understanding of interesting physics such as high-temperature superconductivity and metal-insulator phase transitions. In this thesis, we present a variety of new developments in the auxiliary-field quantum Monte Carlo (AFQMC) methods, including the incorporation of symmetry in both the trial wave function and the projector, developing the constraint release method, using the force-bias to drastically improve the efficiency in Metropolis framework, identifying and solving the infinite variance problem, and sampling the Hartree-Fock-Bogoliubov wave function. With these developments, some of the most challenging many-electron problems are now under control. We obtain an exact numerical solution of the two-dimensional strongly interacting Fermi atomic gas, determine the ground state properties of the 2D Fermi gas with Rashba spin-orbit coupling, provide benchmark results for the ground state of the two-dimensional Hubbard model, and establish that the Hubbard model has a stripe order in the underdoped region.

## TABLE OF CONTENTS

Acknowledgments . . . . .	v
Dedication . . . . .	vi
CHAPTER	
1    Introduction . . . . .	1
2    Generic AFQMC Methods . . . . .	7
2.1    Hubbard Model . . . . .	7
2.2    Projection Method . . . . .	8
2.3    Openended Random Walk . . . . .	10
2.3.1    Unconstrained Free Projection (FP) . . . . .	11
2.3.2    Constraint Path (CP) . . . . .	13
2.3.3    Release Constraint (RC) . . . . .	16
2.4    Metropolis Algorithm . . . . .	17
3    Symmetry Improved AFQMC . . . . .	21
3.1    Hubbard-Stratonovich Transformation . . . . .	22
3.2    Symmetry of the Trial Wave Function . . . . .	29
3.2.1    Trial Wave Function in FP Calculations . . . . .	30
3.2.2    Trial Wave Function in CP Calculations . . . . .	33
3.2.3    Trial Wave Function in RC Calculations . . . . .	36
3.3    Conclusion . . . . .	40

4	Infinite Variance in QMC . . . . .	44
4.1	Symptoms and Origin of the Problem . . . . .	45
4.2	Illustration from a Toy Model . . . . .	49
4.3	Solution . . . . .	55
4.4	Discussion . . . . .	65
4.5	Conclusion . . . . .	71
5	AFQMC in Hartree-Fock-Bogoliubov Space . . . . .	73
5.1	HFB Basics . . . . .	75
5.2	Method . . . . .	76
5.2.1	Product State . . . . .	77
5.2.2	Thouless State . . . . .	82
5.3	Illustrative Results . . . . .	85
5.3.1	Kitaev Model . . . . .	85
5.3.2	Hubbard Model . . . . .	88
5.4	Discussion and Summary . . . . .	92
6	Strongly Interacting Fermi Gases in Two Dimensions . . . . .	95
6.1	Introduction . . . . .	95
6.2	Model and Method . . . . .	97
6.3	Results . . . . .	99
6.3.1	Equation of State . . . . .	99
6.3.2	Contact . . . . .	103
6.3.3	Pair Wave Function . . . . .	104
6.3.4	Condensate Fraction . . . . .	106
6.4	Summary . . . . .	107

7	Two-Dimensional Fermi Gas with Rashba Spin-orbit Coupling . . . . .	109
7.1	Introduction . . . . .	109
7.2	Model . . . . .	111
7.3	Results . . . . .	114
7.3.1	Equation of State . . . . .	114
7.3.2	Momentum Distributions and Helicity Bands . . . . .	115
7.3.3	Pair Wave Function . . . . .	117
7.3.4	Spin Nematic Order . . . . .	120
7.4	Summary . . . . .	121
8	Ground State Properties of the Two-dimensional Hubbard Model . . . . .	122
8.1	Introduction . . . . .	122
8.2	Results at Half Filling . . . . .	124
8.2.1	Energy, Double Occupancy, and Effective Hopping . . . . .	124
8.2.2	Spin Correlations and Magnetization . . . . .	129
8.3	Results Away from Half-filling . . . . .	132
8.3.1	Low to Medium Density . . . . .	133
8.3.2	$n = 0.875$ . . . . .	136
8.4	Conclusion . . . . .	137
9	Conclusion and Outlook . . . . .	139
APPENDIX A		
	HFB Additional Notations and Formulas . . . . .	144
APPENDIX B		
	The Special Case of an HFB Wave Function and a Slater Determinant . . . . .	149
APPENDIX C		
	Generalized Metropolis with Force Bias . . . . .	153
APPENDIX D		
	Extrapolation to the Continuum Limit in Fermi Gases . . . . .	157

Bibliography . . . . .	159
Vita . . . . .	175

## ACKNOWLEDGMENTS

Foremost, I would like to thank my advisor Prof. Shiwei Zhang for his support during my Ph.D. study. Shiwei has been patient and has given me the freedom to pursue various projects. He is my primary resource for getting my science questions answered and provided insightful discussions and guidance about the research. I am also thankful for his helpful writing, presenting, and career advice. Thank you for being a great advisor and a sincere friend.

I am grateful for the rest of my committee members: Prof. Henry Krakauer, Prof. Kostas Orginos, Prof. Seth Aubin, and Prof. Andreas Stathopoulos, for their insightful comments and suggestions, which help to shape and polish the dissertation from different perspectives.

I would like to thank my fellow doctoral students and Postdoctoral Researchers for their cooperation and friendship. With a special mention to Dr. Simone Chiesa, Dr. Fengjie Ma, Dr. Mingpu Qin, Dr. Ettore Vitali, Mr. Peter Rosenberg, Dr. Mario Motta, Dr. Eric J. Walter, and Dr. Wirawan Purwanto, thank you for the discussion and collaboration, especially for answering my science questions.

I am grateful to my wife, my parents and my sister who have supported me emotionally and spiritually. Special thanks to my son: Lawrence and Frank, for bringing me so many joyous moments. I am also grateful to my other family members and friends along the way.

Last but not the least, I would like to thank everyone in the condensed matter group, it was great to share the working environment with all of you.

I dedicate this thesis to my parents, my wife, and my sons  
for their constant support and unconditional love.

COMPUTATIONAL STUDIES OF STRONGLY CORRELATED QUANTUM  
MATTER

# CHAPTER 1

## Introduction

The study of interacting quantum many-fermion systems remains an outstanding challenge, especially for systems with strong particle interactions, where perturbative approaches are ineffective. In particular, phenomena such as high-T<sub>c</sub> superconductivity [1], colossal magnetic resistance [2] as well as superconductivity in the iron-based compounds [3, 4], require us to better understand the nature of the electron-electron correlations and their impact on the resulting properties of the considered quantum systems.

Numerical simulations provide a promising approach for studying such systems. For sufficiently small lattices, exact diagonalization is possible. However, due to its exponential cost, such an exact diagonalization becomes impossible beyond a given system size. One can then resort to other approaches such as variational Monte Carlo [5, 6, 7] (VMC), Coupled Cluster [8] (CC) and Density Matrix Renormalization Group [9, 10, 11] (DMRG) methods etc, each of which has its own strengths and weaknesses.

Auxiliary-field quantum Monte Carlo [12, 13, 14] (AFQMC) is one of the most popular methods to extract collective properties of quantum many-body systems, which are applied in condensed matter physics, nuclear physics, high-energy physics, and quantum chemistry. These methods allow essentially exact calculations of ground-state and finite-temperature equilibrium properties of interacting many fermion systems. As is well known, however, they suffer from the sign/phase problem which severely limits their applicability [15, 16]. This problem fundamentally changes the (low) algebraic scaling of the computational time with respect to system size or inverse temperature [17], making the statistical noise in the computed results grow exponentially.

For some classes of fermion problems, however, the calculations can be formulated to be free of the sign problem. Examples span multiple areas in physics, and range from the half-filled repulsive Hubbard model for magnetism and possible spin liquid states [18, 19], to spin-balanced fermions with attractive interaction describing atomic Fermi gases, to Kane-Mele models [20] and spinless fermion models [21, 22] for topological phases, to zero-density lattice QCD calculations [23, 24, 25]. By exploiting certain symmetries of the problems, the integrand in the many-dimensional integral, despite fermion antisymmetry, can be made non-negative in this method. These classes of fermion problems are growing in number and in impact, as more problems are being discovered and more models are being proposed and studied [26, 27, 22, 21, 28] where the sign problem can be made absent in a similar manner. In these situations, quantum Monte Carlo (QMC) calculation is relied upon to provide definitive answers for our understanding of fundamental models

or systems, much like in boson systems, unfrustrated quantum spin models, or in classical Monte Carlo (MC) simulations. In this thesis, we show that the commonly employed forms of the determinantal QMC approach, as applied to such situations, have MC variances that diverge. A method is then proposed to solve the problem.

For systems where there is a sign problem (for example, Hubbard-like models where the local interactions lead to auxiliary-fields that are real), considerable progress has been achieved by constraining the random walks in sampling the space of auxiliary-fields. These methods have come under the name of constrained path auxiliary-field quantum Monte Carlo (CPMC). For electronic systems where there is a phase problem (as the Coloumb interaction leads to complex fields), the methods [29, 30, 31] have been referred to as phaseless or phase-free auxiliary-field QMC. In both cases, the idea is to constrain the sign or phase of the overlap of the sampled Slater determinants with a trial wave function. It eliminates the sign or phase instability and restores low-power (typically to the third power of system size) computational scaling. Applications to a variety of systems have shown that the methods are very accurate, even with simple trial wave functions taken directly from mean-field calculations (see, e.g. Refs [14] and references therein). However, these methods are approximate. For example, open-shell situations often result in larger systematic errors. It is thus important to understand and develop ways to improve the quality of the constraint.

In this thesis, we present a variety of new developments in the AFQMC methods, both for cases without and with sign problems include the incorporation of symmetry in both

the trial wave function and the projector, developing the constraint release method, using force-bias to improve the efficiency in Metropolis framework, identifying and solving the infinite variance problem, and formulating the AFQMC method in Hartree-Fock-Bogoliubov space. With these advances in the computational algorithm, we are able to provide exact numerical results for the ground state of the strongly interacting 2D spin-balanced uniform Fermi gas and the 2D Fermi gas with strong attractive interactions and Rashba Spin-orbit coupling. We also obtain benchmark results for the two-dimensional repulsive Hubbard model and establish that the Hubbard model has a stripe order in the underdoped region. This progress demonstrates that we now have the ability to study some of the most challenging many-electron problems.

The rest of this dissertation is organized as follows.

In Chapter 2, we describe the key features of ground state AFQMC methods. Using the Hubbard model as a concrete example, we introduce AFQMC for both open-ended random walks and the Metropolis framework.

In Chapter 3, we present approaches to impose symmetry in AFQMC calculations and study the effects on computational efficiency and on the sign problem. We consider symmetry in the Hubbard-Stratonovich transformation and the trial wave function. Three flavors of AFQMC in open-ended random walk framework will be discussed.

In Chapter 4, we show that the commonly employed Metropolis forms of the determinantal QMC approach have MC variances that diverge. We illustrate the infinite variance problem, discuss its origin, and examine ways to detect it. A method is then proposed to

solve the problem, which is straightforward to implement within the standard algorithms. This work can potentially be useful in many other MC simulations.

In Chapter 5, we propose a QMC method for handling many-fermion Hamiltonians without  $U(1)$  symmetry. The method evaluates the path integral in auxiliary-field space to produce a ground-state wave function by sampling Hartree-Fock-Bogoliubov states. It is a generalization of the AFQMC method from the space of Slater determinants to that of Hartree-Fock-Bogoliubov states. The method is useful for interacting fermion systems in the presence of pairing fields or systems with strong pair order.

In Chapter 6, we obtain exact numerical results on the ground state of the strongly interacting 2D spin-balanced uniform Fermi gas. We employ two AFQMC approaches: one based on the branching random walk method, and the other on a novel approach in the Metropolis path-integral framework that dramatically improves efficiency. Their combination allows us to calculate the thermodynamics and pairing properties exactly in the entire range of interaction strengths. Our results provide valuable benchmarks for future studies and allow precise comparisons with experiments as the latter rapidly develop in 2D.

In Chapter 7, we present the first exact results on the ground state of the 2D Fermi gas with strong attractive interactions and Rashba spin-orbit coupling. We show how spin-orbit coupling effects in many-fermion systems can be treated by AFQMC, formulated as random walks of general Slater determinants consisting of spin-orbitals. These *ab initio* precision many-body results provide benchmark for theory and can serve as a calibration

for experiments.

In Chapter 8, we describe results of the two-dimensional repulsive Hubbard model studied by AFQMC method. At half-filling, our results are numerically exact and serve as a benchmark for other numerical algorithms in the Simons collaboration [32]. Away from half-filling, we employ the CPMC method, which removes the sign problem and allows us to systematically reach large system sizes. We establish the ground state to be a spin density wave (stripe order) in the underdoped region.

In Chapter 9, we present our conclusion and comment on the future direction of this research.

Finally, the Appendices contain additional technical details of the methods used in this dissertation.

# CHAPTER 2

## Generic AFQMC Methods

We summarize the key features of ground state AFQMC methods that are relevant to the studies to follow. We will use the Hubbard model as a concrete example; however most of our discussions will apply to other Hamiltonians, including more realistic materials Hamiltonians.

### 2.1 Hubbard Model

The Hubbard model is written in second-quantized form as [33]:

$$\hat{H} = \hat{K} + \hat{V} = -t \sum_{\langle i,j \rangle \sigma}^L c_{i\sigma}^\dagger c_{j\sigma} + U \sum_i^L n_{i\uparrow} n_{i\downarrow}. \quad (2.1)$$

Here  $L$  is the number of lattice sites,  $c_{i\sigma}^\dagger$  and  $c_{i\sigma}$  are creation and annihilation operators of an electron of spin  $\sigma$  on the  $i$ -th lattice site,  $t$  is the nearest-neighbor hopping energy,

$U$  is the interaction strength, and  $n_\sigma$  is the density operator for spin  $\sigma$ . Throughout this thesis, we will use  $t$  as units of energy and set  $t = 1$ . We assume that there are  $N_\uparrow$  spin-up electrons and  $N_\downarrow$  spin-down electrons on the lattice.

The Hamiltonian in Eq. (2.1), whose Hilbert space grows exponentially in size with  $L$ , presents an enormous challenge. Questions remain open about its properties.

## 2.2 Projection Method

Projection with MC sampling is one of the candidates to find the ground state  $|\psi_0\rangle$ .

The projection method is:

$$|\psi_0\rangle \propto \lim_{\beta \rightarrow \infty} e^{-\beta(\hat{H}-E_T)} |\psi_T\rangle, \quad (2.2)$$

where  $E_T$  and  $|\psi_T\rangle$  are guesses of the ground state energy and wave function, and  $\langle\psi_0|\psi_T\rangle \neq 0$  in order for the projection to yield the ground state asymptotically. To target a lowest energy excited state of a different symmetry from  $|\psi_0\rangle$  is similar to doing a ground-state calculation, except one would choose a  $|\psi_T\rangle$  which is not orthogonal to the targeted excited state but satisfies  $\langle\psi_0|\psi_T\rangle = 0$ .

The propagator can be evaluated using a Trotter-Suzuki breakup [34, 35]:

$$(e^{-\Delta\tau(\hat{K}+\hat{V})})^n = (e^{-\frac{1}{2}\Delta\tau\hat{K}} e^{-\Delta\tau\hat{V}} e^{-\frac{1}{2}\Delta\tau\hat{K}})^n + O(\Delta\tau^2). \quad (2.3)$$

Here we have  $\Delta\tau n = \beta$ , and a Trotter error arises from the omission of the higher order terms. We will not be concerned with the Trotter error here, other than to note that it

can be controlled by extrapolating to  $\Delta\tau \rightarrow 0$  with separate calculations using different  $\Delta\tau$  values. We can either perform such an extrapolation explicitly, or check via separate calculations that the Trotter error is within the statistical error. We also mention that, for the Hubbard interaction, decompositions without Trotter errors are possible [36].

The two-body propagator is then decoupled into a one-body propagator by auxiliary fields, using the Hubbard-Stratonovich (HS) transformation [37, 38]. The general form is:

$$e^{-\Delta\tau\hat{V}} = \sum_x p(x) e^{\hat{o}(x)}, \quad (2.4)$$

where  $\hat{o}(x)$  is a one-body operator that depends on the auxiliary field  $x$ ,  $p(x)$  is a probability density function with the normalization  $\sum_x p(x) = 1$ . In general, the sum in Eq. (2.4) is an integral, and  $x$  is a many-dimensional vector whose dimension is of the order of the size of the one-particle basis. In the Hubbard model,  $x$  typically has  $L$  components, one for each lattice site. By setting:

$$\hat{B}(x) = e^{-\frac{1}{2}\Delta\tau\hat{K}} e^{\hat{o}(x)} e^{-\frac{1}{2}\Delta\tau\hat{K}}, \quad (2.5)$$

we rewrite the projection as

$$|\psi_0\rangle = \lim_{\Delta\tau \rightarrow 0} \sum_{\vec{X}} P(\vec{X}) \prod_{i=1}^n \hat{B}(x_i) |\psi_T\rangle. \quad (2.6)$$

The vector  $\vec{X}$  means  $(x_1, x_2, \dots, x_n)$ , and  $P(\vec{X}) = \prod_i p(x_i)$ .

Then the ground state properties can be evaluated by:

$$\langle \hat{A} \rangle_0 = \frac{\langle \psi_0 | \hat{A} | \psi_0 \rangle}{\langle \psi_0 | \psi_0 \rangle}, \quad (2.7)$$

which are many-dimensional integrals (e.g.,  $2nL$ -dimensions in the Hubbard model). MC methods are used to calculate the high dimension integrals, by sampling the probability density function using the open-ended random walk approach or the Metropolis algorithm [39] which will be talked about in the following sections. The sign problem emerges because the integrand in the denominator,  $P(\vec{X})\langle \psi_T | \prod \hat{B}(x_i) | \psi_T \rangle$  is not always positive, which causes the MC signal to be eventually lost in the sampling noise.

## 2.3 Openended Random Walk

The many-dimensional integrals can be sampled by the open-ended random walk approach, where a population of  $N_w$  random walkers is carried. These walkers are typically initialized by the trial wave function and will have a weight  $w$  whose value is set as one at the beginning of the projection. In this approach, the imaginary time  $\beta$  is not fixed and a branching (or birth/death) scheme is applied to random walkers.

### 2.3.1 Unconstrained Free Projection (FP)

The FP calculation [40, 29, 41] carries walkers at the beginning of the projection:

$$|\psi^{(0)}\rangle = \sum_i^{N_w} w_i^{(0)} |\phi_i^{(0)}\rangle, \quad (2.8)$$

where  $|\phi_i^{(0)}\rangle$  is Slater determinant wave function.

We apply the projection in Eq. (2.6) by random walks in Slater determinant space. In each step, we sample the auxiliary field  $x$  according to  $p(x)$  by MC, and apply  $\hat{B}(x)$  to the Slater determinant wave function. Since the operators only contain one-body terms, they will generate another Slater determinant [42]:

$$\begin{aligned} |\psi^{(1)}\rangle &= \sum_i^{N_w} \sum_{x_i} p(x_i) \hat{B}(x_i) w_i^{(0)} |\phi_i^{(0)}\rangle \\ &= \sum_i^{N_w} w_i^{(1)} |\phi_i^{(1)}\rangle. \end{aligned} \quad (2.9)$$

During the projection we multiply the constant (non-operator) values of the formula, e.g., the overall normalization  $e^{\Delta\tau E_T}$ , to the weight of the walker. The weight of each walker will fluctuate in the random walk and after a few steps, some walkers can have large weights and some walkers will have small weights. We apply a population control procedure, splitting the walkers with large weights and eliminating walkers with small weights with the appropriate probability [43], such that the overall probability distribution is preserved but the weights are made more uniform. It will introduce a population control bias [15],

however it can be controlled by increasing the number of walkers. Modified Gram-Schmidt orthogonalization is applied to each walker periodically as well [44].

The FP framework does not have any ergodicity issues [45], and it is straightforward to project to longer imaginary-time in order to approach the ground state. We typically turn off importance sampling in FP, sampling the fields according to  $P(\vec{X})$  instead of using either the force bias [29, 41] or direct importance-sampling of discrete fields [15]. Empirically we find that this tends to give smaller statistical errors than invoking importance sampling and then lifting the constraint. The use of population control helps to reduce the noise but ultimately the shortcoming of this approach is that the lack of importance sampling will cause large noises as system size or  $n$  increases. Since in these situations the sign problem, when uncontrolled, tends to overwhelm the calculation anyway, the shortcoming is not of major practical relevance, and we find this mode of sampling to often be the more efficient in practice.

At the  $n^{\text{th}}$  step in the propagation, we measure the energy by:

$$E = \frac{\sum_i^{N_w} w_i^{(n)} \langle \psi_T | H | \phi_i^{(n)} \rangle}{\sum_i^{N_w} w_i^{(n)} \langle \psi_T | \phi_i^{(n)} \rangle}. \quad (2.10)$$

If the projection has equilibrated, we can combine the populations at multiple  $n$  values in the estimator above to improve statistics on the ground-state energy. The energy measure

in Eq. (2.10) is variational if we set  $|\psi^{(0)}\rangle = |\psi_T\rangle$ , since

$$E = \frac{\langle\psi_T|He^{-\beta H}|\psi_T\rangle}{\langle\psi_T|e^{-\beta H}|\psi_T\rangle} = \frac{\langle\psi_T|e^{-\beta H/2}He^{-\beta H/2}|\psi_T\rangle}{\langle\psi_T|e^{-\beta H/2}e^{-\beta H/2}|\psi_T\rangle}. \quad (2.11)$$

To calculate the expectation value of an observable which does not commute with the Hamiltonian, we can use back-propagation [15, 30] using part of the path and projecting the trial wave function  $\langle\psi_T|$ . Because of the lack of importance sampling, back-propagation will tend to be very noisy in FP, and large population size will typically be needed.

### 2.3.2 Constraint Path (CP)

The constrained path (CP) approximation allows one to eliminate the sign problem present in FP. During the FP steps, the overlap between the ground state and the projected wave function,  $\langle\psi_0|\psi^{(l)}\rangle$ , will in general approach zero, because intrinsically the projection is symmetric about  $|\psi^{(l)}\rangle$  and  $-|\psi^{(l)}\rangle$ . In other words, at any given imaginary time  $l$ , the projection would proceed identically if each random walker  $|\phi^{(l)}\rangle$  were switched to  $-|\phi^{(l)}\rangle$ , for example by a permutation of two of its orbitals. This means that, unless the random walks are somehow strictly confined to only one kind of “sign”, it will invariably become a random and equal mixture of both, given sufficiently large  $l$ . Thus measurements from the MC sampling will eventually have infinite variance. This is how the sign problem appears in an FP calculation.

The CP approach is based on the observation that [15], if any particular walker has

the zero overlap with the ground state at imaginary time  $\tau_l \equiv l\Delta\tau$  in the projection:

$$\langle \psi_0 | \phi^{(l)} \rangle = 0 \quad (2.12)$$

this walker will contribute zero at any future time  $\beta > \tau_l$ , because

$$\langle \psi_0 | e^{-(\beta-\tau_l)\hat{H}} | \phi^{(l)} \rangle = 0. \quad (2.13)$$

Then we are able to discard the walker once its path reaches a point where the overlap becomes zero. With this constraint the sign problem is eliminated, and the projection will still lead to the exact ground state. However, we obviously do not know the exact ground state wave function. In CP calculations, a trial wave function,  $|\psi_T\rangle$ , is chosen for determining the sign of the overlap. A walker which develops a zero overlap with  $|\psi_T\rangle$  during the projection is discarded.

Importance sampling can be introduced in CP calculations both as a natural way to impose the constraint and for variance reduction [15, 29, 30]. With importance sampling, the wave function during the projection can be written as:

$$|\psi^{(l)}\rangle = \sum_i^{N_w} w_i^{(l)} \frac{|\phi_i^{(l)}\rangle}{\langle \psi_T | \phi_i^{(l)} \rangle}. \quad (2.14)$$

Instead of  $p(x)$ , one samples the auxiliary-fields from

$$\tilde{p}(x) = p(x) \frac{\langle \psi_T | \hat{B}(x) | \phi_i^{(l)} \rangle}{\langle \psi_T | \phi_i^{(l)} \rangle}, \quad (2.15)$$

which can be accomplished either directly for discrete fields using a heat bath-like approach [15] or more generally via a force bias [29, 30]. This will automatically prevent the random walks from sampling any determinants with zero (or negative) overlap with the trial wave function. Those with larger overlap will be sampled more, although the weight from importance sampling will ensure that the exact distribution defined by Eq. (2.14) is sampled. The energy can be calculated by the mixed estimate similar to Eq. (2.10), although now with importance sampling it has the form:

$$E = \frac{\sum_i^{N_w} w_i^{(n)} \frac{\langle \psi_T | H | \phi_i^{(n)} \rangle}{\langle \psi_T | \phi_i^{(n)} \rangle}}{\sum_i^{N_w} w_i^{(n)}}. \quad (2.16)$$

Following diffusion Monte Carlo (DMC), we refer to the quantity in the numerator,  $E_L(\phi) \equiv \langle \psi_T | H | \phi \rangle / \langle \psi_T | \phi \rangle$  as the local energy. An important characteristic of the constrained path approximation is that the mixed estimate in Eq. (2.16) is not variational [46].

The CP approximation has proved very accurate in the Hubbard model, especially for closed shell systems [15]. For instance, the energy at  $U = 4$  is typically within  $< 0.5\%$  of the exact diagonalization result [47]. It is, however, approximate. The systematic error

in the energy tends to be larger in open-shell systems. We will show that this error can be significantly reduced with trial wave functions which observe the correct symmetry and by the using the self-consistent constraint method [48].

### 2.3.3 Release Constraint (RC)

From a converged CP calculation, one can release the constraint and continue with the projection. Calculations of similar character have been done in the framework of DMC, under the name of released node [49]. Since the CP result is already very close to the ground state and FP in AFQMC tends to have a reduced sign problem in general, one can expect that releasing the constraint in AFQMC will be effective and will allow the removal or reduction of systematic bias in more systems.

In principle the idea of releasing the constraint is straightforward. As mentioned, the RC calculation can theoretically be viewed as an FP calculation, with a much better starting point. Technically, however, the implementation of RC can be challenging. The initial population, namely that from CP, is obtained with importance sampling, which automatically imposes the constraint. The importance function must be modified in RC to allow the random walks to have a significant chance to sample the region with  $\langle \psi_T | \phi^{(l)} \rangle$  being negative (or develop different phases in the more general case).

A key aspect is our use of different forms of the HS transformation in the CP and the RC portions of the calculations. That is, we switch to a different HS decomposition in the RC in order to impose exact symmetry properties which drastically change the behavior

of the RC calculations, as described below.

In RC calculations, we will use a mixed estimator similar to Eq. (2.10) to measure the energy:

$$E_{\text{RC}}(\beta) = \frac{\sum_i^{N_w} w_i^{\text{CP}} \langle \psi_T | H e^{-\beta \hat{H}} | \phi_i^{\text{CP}} \rangle}{\sum_i^{N_w} w_i^{\text{CP}} \langle \psi_T | e^{-\beta \hat{H}} | \phi_i^{\text{CP}} \rangle}. \quad (2.17)$$

Thus  $E_{\text{RC}}(\beta = 0) = E_{\text{CP}}$ . As mentioned, the mixed estimate in CP is not variational. The RC energy will asymptotically converge to the exact ground-state energy. However, it can converge from below or above. Indeed, as we further discuss below, the convergence can be non-monotonic for poorer trial wave functions.

## 2.4 Metropolis Algorithm

We outline the standard metropolis algorithm to sample the many-dimensional integrals. In this approach, the imaginary time  $\beta$  is fixed and auxiliary fields  $\vec{X}$  are sampled by sweeping along the path. The algorithm is very efficient for the sign problem free case, while it is not easy to impose the constraint as in the open-ended random walk approach.

For fixed timeslices  $2n$ , the equation in (2.7) is

$$\langle \hat{O} \rangle = \frac{\int \cdots \int dx_1 dx_2 \dots dx_{2n} p(x_1) \dots p(x_{2n}) \langle \psi_T | \hat{B}(x_{2n}) \dots \hat{B}(x_{n+1}) \hat{O} \hat{B}(x_n) \dots \hat{B}(x_1) | \psi_T \rangle}{\int \cdots \int dx_1 dx_2 \dots dx_{2n} p(x_1) \dots p(x_{2n}) \langle \psi_T | \hat{B}(x_{2n}) \hat{B}(x_{2n-1}) \dots \hat{B}(x_1) | \psi_T \rangle}. \quad (2.18)$$

In Eq. (2.18) we have inserted  $\hat{O}$  in the middle of the path, as we had done in Eq. (2.7).

Of course a measurement can be made anywhere along the path provided it is sufficiently far away from either end to ensure that convergence to the ground state has been reached by the projection from  $|\psi_T\rangle$ . We will use Eq. (2.18) when the explicit formula is needed, with no loss of generality.

If the initial wave function  $|\psi_T\rangle$  is chosen to be a Slater determinant, the propagation by each auxiliary-field path, i.e., each string of  $\hat{B}$  operators, keeps it in the form of a single Slater determinant. For brevity let us introduce the following notation:

$$|\phi^r(\vec{X}_r)\rangle \equiv \hat{B}(x_n)\hat{B}(x_{n-1})\dots\hat{B}(x_1)|\psi_T\rangle \quad (2.19)$$

and

$$\langle\phi^l(\vec{X}_l)| \equiv \langle\psi_T|\hat{B}(x_{2n})\hat{B}(x_{2n-1})\dots\hat{B}(x_{n+1}) \quad (2.20)$$

where the shorthand  $\vec{X}_r$  and  $\vec{X}_l$  denote the collection of auxiliary-fields with indices from 1 to  $n$  (inclusive) and from  $n + 1$  to  $2n$ , respectively.

The integrand in the denominator in Eq. (2.18) is given by

$$f(\mathbf{X}) = P(\mathbf{X}) \langle\phi^l(\mathbf{X}_l)|\phi^r(\mathbf{X}_r)\rangle, \quad (2.21)$$

where the inner product can be conveniently evaluated as the determinant of the product of the matrices corresponding to the "left" and "right" wave functions [14]. Similarly, the

integrand in the numerator is given by

$$g(\mathbf{X}) = P(\mathbf{X}) \langle \phi^l(\mathbf{X}_1) | \hat{O} | \phi^r(\mathbf{X}_r) \rangle, \quad (2.22)$$

so that Eq. (2.18) reduces to a generic form:

$$\langle \hat{O} \rangle = \frac{\int g(\mathbf{X}) d\mathbf{X}}{\int f(\mathbf{X}) d\mathbf{X}}. \quad (2.23)$$

For general fermion problems, the determinant in Eq. (2.21) can be both positive and negative as a function of  $\mathbf{X}$  — indeed it is complex for problems with realistic electronic interactions [29]. However, as mentioned earlier, in many important classes of problems,  $f(\mathbf{X})$  turns out to be non-negative. For instance, in the repulsive half-filled Hubbard Hamiltonian of Eq. (2.1), there is no sign problem as long as we choose a  $|\psi_T\rangle$  which ensures partial particle-hole symmetry. This is one example where  $f(\mathbf{X})$  can be written as the square or complex conjugation product of two determinants. More generally, in these sign-problem-free situations  $f(\mathbf{X})$  can often be thought of as the determinant of a matrix whose eigenvalues appear in pairs, either degenerate real values or complex conjugates.

For any problem with  $f(\mathbf{X}) \geq 0$ , it is straightforward to sample the probability density function (PDF):  $f(\mathbf{X}) / \int f(\mathbf{X}) d\mathbf{X}$  by Metropolis [50] and use MC to evaluate Eq. (2.23):

$$\langle \hat{O} \rangle \doteq \left\langle \frac{g(\mathbf{X})}{f(\mathbf{X})} \right\rangle_f, \quad (2.24)$$

where the average is with respect to the configurations sampled from  $f(\mathbf{X})$ . The estimator  $g/f$  reduces to  $\langle \phi^l(\mathbf{X}_l) | \hat{O} | \phi^r(\mathbf{X}_r) \rangle / \langle \phi^l(\mathbf{X}_l) | \phi^r(\mathbf{X}_r) \rangle$ , which is conveniently evaluated by the corresponding Green functions if  $\hat{O}$  is a one-body operator and by combinations of Green functions via Wick's theorem if  $\hat{O}$  is a two-body correlation function [50, 14]. This is the standard metropolis determinantal QMC approach.

## CHAPTER 3

# Symmetry Improved AFQMC

In this chapter, we describe approaches to impose symmetry in AFQMC calculations, and study their effects on computational efficiency and, more importantly, on the sign problem. We divide the discussion into two parts: the choice of the HS transformation and its effect on symmetry, and symmetry in the trial wave function. While we will consider all three flavors of AFQMC introduced in Sec. 2.3, our focus will be on CP and RC, since these are the most general methods which will allow calculations to scale to large system sizes. This chapter shows that the use of symmetry can lead to large reductions in statistical and systematic errors, and alleviate the sign problem.

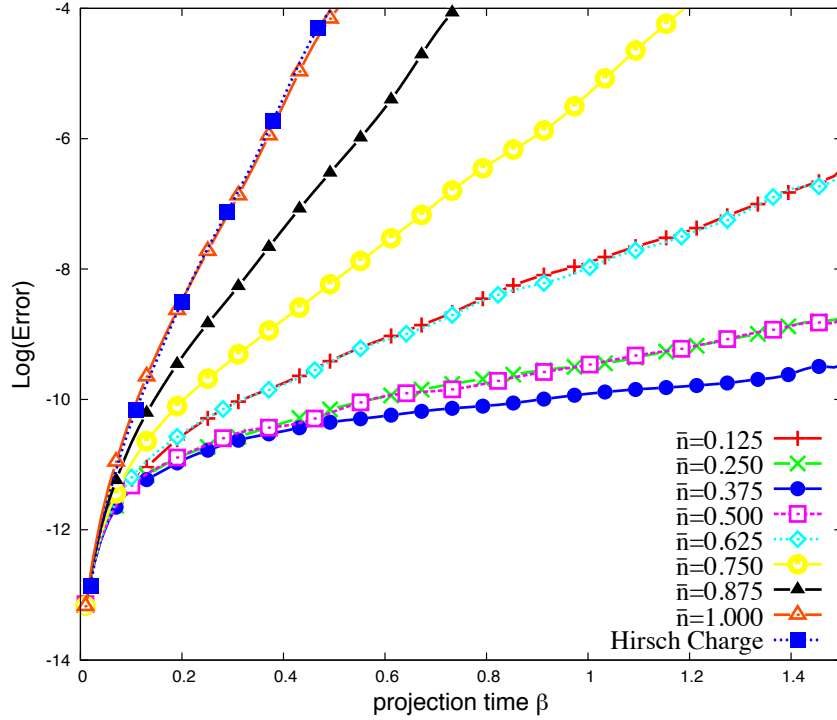


FIG. 3.1: Statistical error bar (log-scale) versus projection time for different HS transformations. FP calculations are shown. The error bars increase exponentially with projection time, but the optimal choice of the background  $\bar{n}$  in Eq. (3.6) greatly reduces the fluctuation and improves efficiency. The system shown is a  $4 \times 4$  lattice with  $N_\uparrow = 3$  and  $N_\downarrow = 3$ , and  $U = 4$ .

### 3.1 Hubbard-Stratonovich Transformation

For each form of the two-body interaction, there are different ways to decompose the propagator, leading to different forms of Eq. (2.4). Decompositions based on Hartree, Fock, and pairing mean-fields are all possible. Even within each mean-field framework, the details can affect the final form of the one-body propagator and the computational efficiency. When a constraint is imposed, the form of the HS transformation chosen can affect the systematic accuracy for a given form of the trial wave function. For the Hubbard interaction, for example, the most commonly used HS transformation involves discrete

auxiliary-fields, due to Hirsch [38]. The spin form of this decomposition is:

$$e^{-\Delta\tau U n_{i\uparrow} n_{i\downarrow}} = e^{-\Delta\tau U (n_{i\uparrow} + n_{i\downarrow})/2} \sum_{x_i=\pm 1} \frac{1}{2} e^{\gamma x_i (n_{i\uparrow} - n_{i\downarrow})}, \quad (3.1)$$

which results in an Ising-like auxiliary-field for each lattice site. The constant  $\gamma$  is determined by

$$\cosh(\gamma) = e^{\Delta\tau U/2}. \quad (3.2)$$

It can also be mapped to a charge density form:

$$e^{-\Delta\tau U n_{i\uparrow} n_{i\downarrow}} = e^{-\Delta\tau U (n_{i\uparrow} + n_{i\downarrow} - 1)/2} \sum_{x_i=\pm 1} \frac{1}{2} e^{\gamma x_i (n_{i\uparrow} + n_{i\downarrow} - 1)}, \quad (3.3)$$

with

$$\cosh(\gamma) = e^{-\Delta\tau U/2}. \quad (3.4)$$

A more general HS transformation [37],

$$e^{\hat{A}^2} = \frac{1}{\sqrt{2\pi}} \int_{-\infty}^{\infty} e^{-x^2/2 + \sqrt{2}x\hat{A}} dx, \quad (3.5)$$

applies to any two-body operators written in the form of a square. To apply this to the Hubbard interaction, we write:

$$n_{i\uparrow} n_{i\downarrow} = \frac{1}{2} [(n_{i\uparrow} + n_{i\downarrow} - \bar{n})^2 - \bar{n}^2 - (1 - 2\bar{n})(n_{i\uparrow} + n_{i\downarrow})], \quad (3.6)$$

where  $\bar{n}$  can take any value (including acquiring a dependence on  $i$ ). We then let  $\hat{A} = \sqrt{-\Delta\tau U/2}(n_{i\uparrow} + n_{i\downarrow} - \bar{n})$  and use Eq. (3.5) to obtain an HS transformation with continuous fields. The constant  $\bar{n}$  can be thought of, physically, as a background term that one subtracts from the one-body operator *prior to* applying the HS transformation. This has been pointed out before for Hubbard interactions [51] and for Coulomb interactions [52, 31]. As discussed below, the optimal choice for  $\bar{n}$  is to remove all background interactions from the mean-field, by minimizing the quadratic first term on the right-hand side in Eq. (3.6). Over typically densities, this choice leads to significant improvement over other choices including the standard Hirsch discrete decomposition [38].

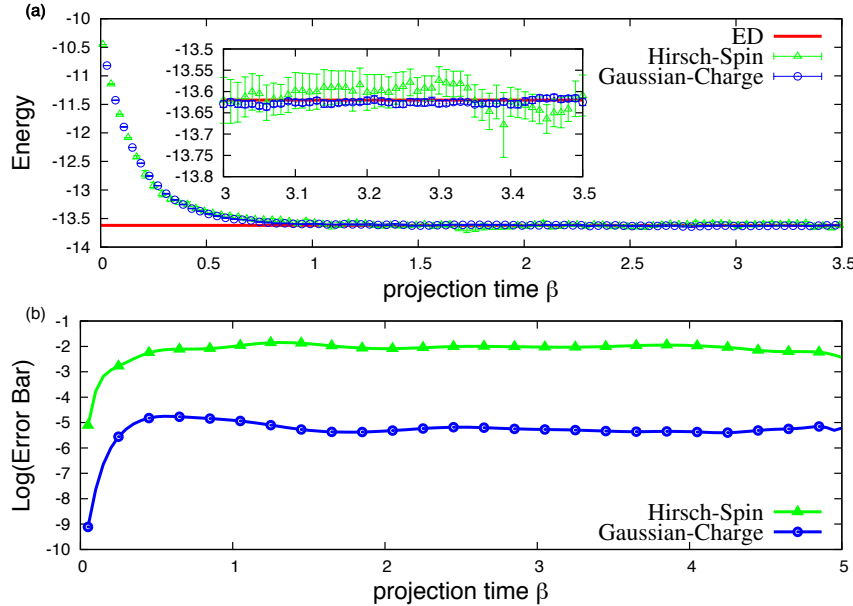


FIG. 3.2: Illustration of the effect of preserving symmetry in the HS transformation: Hirsch spin (Eq. (3.1)) vs. Gaussian charge (Eqs. (3.5) and (3.6)). Panel (a) plots the energy from FP versus projection time, with the inset showing a magnified view of  $\beta \in (3, 3.5)$ . Exact diagonalization (ED) result is shown for comparison. Panel (b) shows the statistical error bar as a function of projection time in a semi-log plot. The system is the  $8 \times 8$  Hubbard model, with  $N_\uparrow = N_\downarrow = 32$  and  $U = 8$ . A Hartree-Fock trial wave function is chosen. The number of walkers was  $10^5$ , with a total 20 separate runs to obtain the final averages and estimate the error bars.

In Fig. 3.1, we illustrate the effect of the background  $\bar{n}$  in the continuous charge decomposition of Eqs. (3.5) and (3.6). The logarithm of the statistical error bar is plotted versus projection time for different values of the background  $\bar{n}$ . The calculations are all FP so the sign problem is present, as indicated by the growing error bars, which are essentially linear in the log-plot with projection time. It is seen that the minimum statistical error is achieved when  $\bar{n} = \langle n_{i\uparrow} + n_{i\downarrow} \rangle_{\text{MF}} = (N_{\uparrow} + N_{\downarrow})/L$ . The efficiency of the HS decomposition decreases as  $\bar{n}$  deviates from the optimal value. It is a symmetric function of the deviation: a background value which is larger or smaller than the optimal value by the same amount gives comparable results. We point out that, although we have illustrated this with the repulsive model, the same applies to the attractive case. For example, in dilute Fermi gas simulations, Eqs. (3.6) with a small  $\bar{n}$  will be much more efficient than Eqs. (3.3) which corresponds to  $\bar{n} = 1$ .

It is often thought that the use of a discrete HS field, compared to continuous fields, leads to significant performance advantages [53]. This is not the case, as shown in Fig. 3.1. The discrete charge decomposition of Eq. (3.3) is shown in the figure. We see that it is almost the same as the continuous decomposition with  $\bar{n} = 1$ . This is because the interaction term in the discrete charge decomposition is mapped to  $(n_{i\uparrow} + n_{i\downarrow} - 1)$ , identical to the continuous transformation when  $\bar{n}$  is set to 1. The discrete decomposition is ideal near half-filling, but will be inefficient in dilute systems, for example, in Fermi gas simulations [54].

Because the decomposition in Eq. (3.5) preserves SU(2) symmetry, it can be more

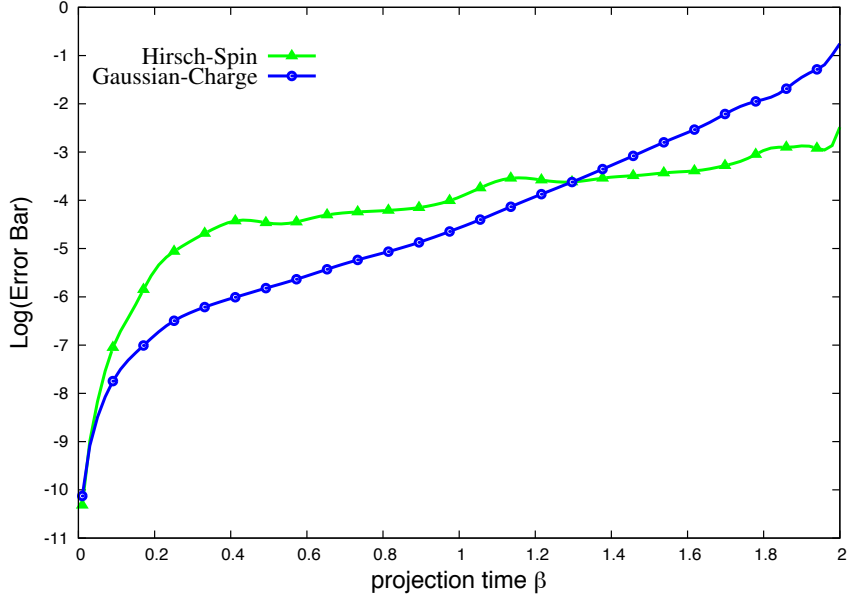


FIG. 3.3: Comparison of discrete spin and Gaussian charge decomposition in the presence of a sign/phase problem. The logarithm of the statistical error bars from FP is plotted vs. projection time for a  $4 \times 4$  lattice with  $N_\uparrow = N_\downarrow = 7$  and  $U = 8$ . A symmetric multi-determinant trial wave function is used. The number of walkers is  $5 \times 10^5$ , with a total of 100 separate runs to estimate the error bars.

efficient than the discrete spin decomposition of Eq. (3.1), which is the most commonly used form in simulations of systems with repulsive interactions. This point is more subtle, however, as it is intertwined with the sign/phase problem. In Fig. 3.2, the two decompositions are compared in a situation free of the sign problem, namely the half-filled repulsive Hubbard model. It can be seen that the Gaussian charge decomposition leads to much smaller statistical fluctuations. This has also been pointed out by Meng *et. al.* [18], using the discrete charge decomposition of Eq. (3.3) at half filling.

In Fig. 3.3 we study the case when a phase problem is present ( $U > 0$ , so  $\hat{A}$  is imaginary):  $4 \times 4$ , with  $N_\uparrow = N_\downarrow = 7$  and  $U = 8$ . This system has a severe sign problem for the discrete spin decomposition. The continuous Gaussian decomposition leads to a

phase problem. The latter decomposition initially has smaller error bars, benefiting from the preservation of symmetry, but after some time, its error bars exceed that of the spin decomposition. So in systems with a sign/phase problem, the efficiency is a balance of two competing aspects. On the one hand, the charge decomposition has an advantage for preserving symmetry. On the other hand, the phase problem tends to result in fast deterioration of the statistical signal and is a disadvantage. Below we discuss how to exploit these characteristics in different calculations.

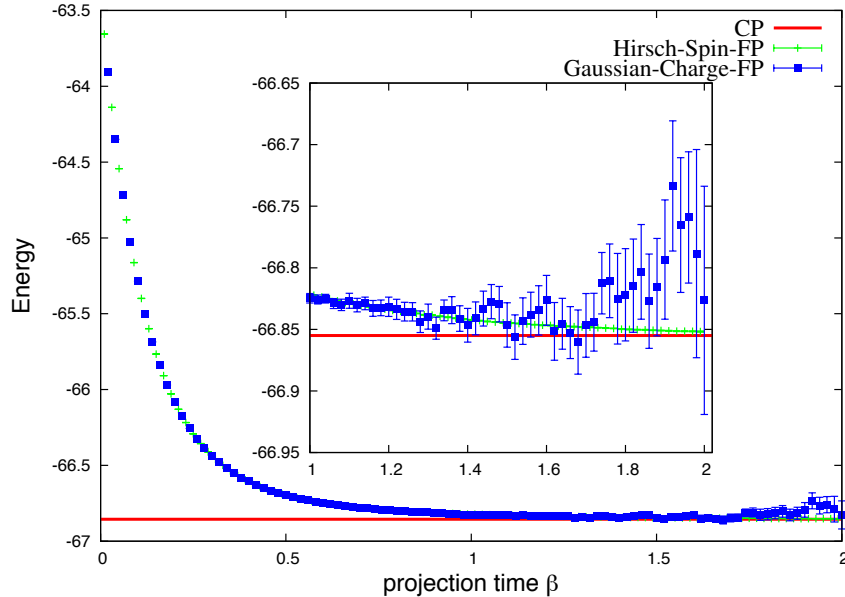


FIG. 3.4: Total energy versus projection time in FP calculations using discrete spin and continuous charge decompositions. The system is a  $8 \times 8$  lattice under periodic boundary conditions, with  $N_\uparrow = N_\downarrow = 13$  and  $U = 4$ . A FE trial wave function is used. The number of walkers is  $5 \times 10^5$ , with total 60 runs to obtain the average and estimate the statistical error bars. The red horizontal line gives the final CPMC result. The inset shows a magnified view of the last part of the projection. The spin decomposition calculation provides a reliable upper bound to the ground-state energy.

We can use the advantage of the spin decomposition in longer time projections, as shown in Fig. 3.4 in a FP calculation of the periodic  $8 \times 8$  supercell with  $N_\uparrow = N_\downarrow = 13$  and

$U = 4$ . The continuous charge decomposition has much larger noise and is not accurate enough. The discrete spin decomposition has rather small fluctuations and provides a useful estimate of an upper bound of the ground-state energy:  $-66.855(2)$ . The run took  $\sim 17$  hours on 100 AMD Opteron 2.4GHz cores. (For comparison, the CP calculation using a free-electron (FE) trial wave function gives  $-66.857(2)$ , as indicated by the line in Fig. 3.4, running for minutes on a single core. )

The charge decomposition can offer a significant advantage in short projection time, however. A main application of this is in RC calculations. Since we start from a population of a converged CP run, the initial state is close to the true ground state. One can expect a short projection in the RC calculation to recover a significant fraction of the correction to CP. In Fig. 3.5, we show an example RC calculation, for the same system as in Fig. 3.3. In this calculation, the CPMC portion always uses the standard spin decomposition, which has a severe sign problem. As can be seen from the inset, the CP energy obtained from the mixed-estimate is not variational [46]. (Typical CP calculations will run to much larger  $\beta$  than shown in the main figure, in order to collect statistics.) In the RC portion, two different calculations are shown, one continuing to use the discrete spin decomposition while the other switching to the symmetry charge-decomposition. It is seen that the latter leads to much smaller statistical fluctuations and allows the RC calculation to reach convergence. The RC with discrete spin decomposition has much larger errors, and also displays a population control bias [15]. (The statistical error and the bias could, of course, be reduced by increasing the population size further.)

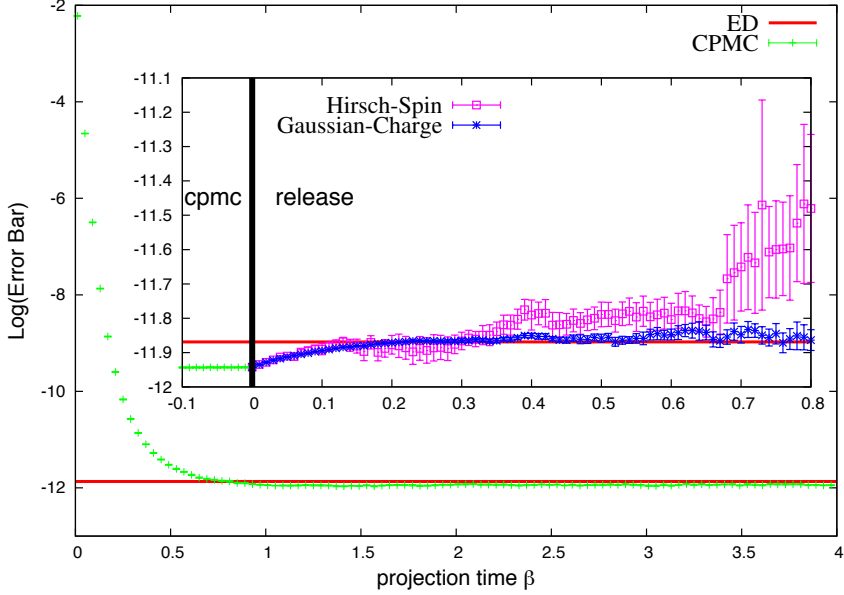


FIG. 3.5: Effect of symmetry decomposition in release constraint calculations. The main figure shows the convergence of CPMC energy with projection time, compared with the exact ground-state energy. The CPMC calculation uses the discrete spin decomposition. The inset shows RC calculations, starting from a converged CP state, using two different forms of the HS decomposition. The system is the same as in Fig. 3.3:  $4 \times 4$ ,  $N_\uparrow = N_\downarrow = 7$  and  $U = 8$ , using a symmetric multi-determinant trial wave function. The number of walkers is  $1 \times 10^5$ , with a total of 100 runs in the RC portion to collect statistics.

## 3.2 Symmetry of the Trial Wave Function

In this section we discuss the other aspect of symmetry in AFQMC calculations, the use of trial wave functions which preserve symmetry. We generate the trial wave function with particular symmetries: total spin  $S^2$ , total momentum  $\vec{K}$ , rotational symmetry in momentum space  $R$ , mirror reflection  $\sigma$  along the line  $K_y = K_x$  in momentum space. When the total momentum  $\vec{K} = 0$ , we use the  $C_{4v}$  point group irreducible representation to label different symmetry state. In the present work, these properties are imposed in the trial wave function by a brute-force approach, making a linear combination of Slater

determinants, which we obtain by diagonalizing in the subspace of the open-shell [in the spirit of a small complete active-space self-consistent field (CASSCF) calculation]. It can also be achieved by projecting symmetry to Hartree-Fock wave functions [55, 56].

### 3.2.1 Trial Wave Function in FP Calculations

Imposing the proper symmetry in the trial wave function can accelerate convergence and reduce the equilibration time in the FP calculations. As mentioned in Sec. 2.3.1, the trial wave function is often also used to generate the initial population in FP. In all the FP calculations in this section, we use the HS transformation given in Eqs. (3.5) and (3.6), using optimal background values from simple mean-field calculations.

We illustrate the effect of the symmetry in the trial wave function in Fig. 3.6. In the top panel, we consider a half-filled system which is thus sign-problem-free. The effects of three trial wave functions are compared: the unrestricted Hartree-Fock (UHF) wave function, a single-determinant trial wave function formed by occupying  $k$ -states, and a multi-determinant trial wave function which preserves additional symmetry. The UHF trial wave function builds in correlation effect via its static anti-ferromagnetic order, and is an excellent starting point, as can be seen from the variational energy values at the beginning of the projection. However, it is contaminated by higher spin eigenstates, and the FP with UHF exhibits a long convergence time, as seen in the inset. (The effect of spin-contamination in AFQMC calculations has been discussed in continuum systems by Purwanto *et. al.* [57].) The single-determinant FE trial wave function has a very high

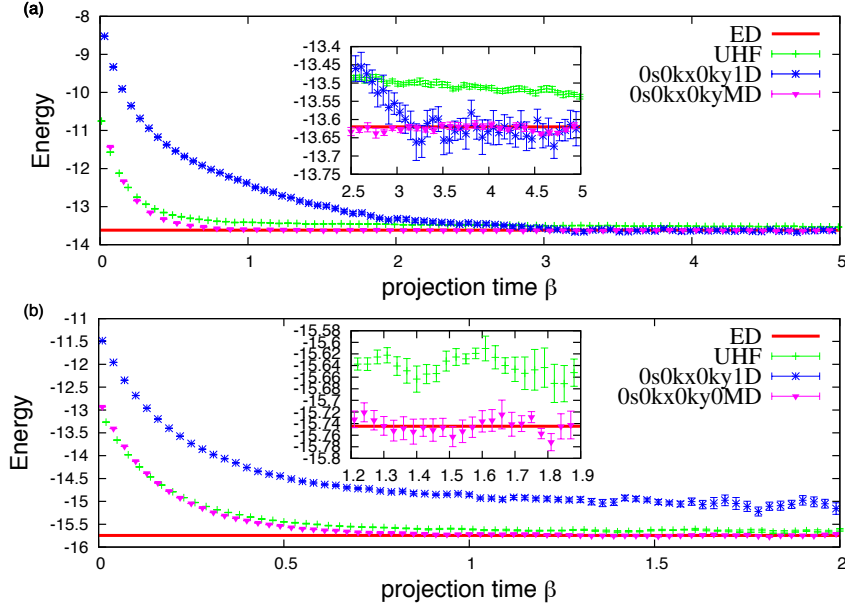


FIG. 3.6: The effect of symmetry trial wave functions in FP calculations, compared to exact results in  $4 \times 4$  lattices with  $U = 4$ : (a)  $N_\uparrow = N_\downarrow = 8$ , no sign problem; (b)  $N_\uparrow = N_\downarrow = 7$ , severe phase problem. The UHF trial wave function is generated by a UHF calculation with  $U = 0.5$ ,  $0s0kx0ky1D$  is a single-determinant non-interacting trial wave function with  $S^2 = 0$  and  $k_x = k_y = 0$ , and  $0s0kx0kyMD$  is a multi-determinant trial wave function which has rotational symmetry in momentum space in (a) and B1 symmetry in (b), in addition to  $S^2 = 0$ ,  $k_x = 0$ ,  $k_y = 0$ .

variational energy. Its statistical error bars are larger since the  $|\psi_T\rangle$  in Eq. (2.10) to evaluate the energy is much poorer, and preserves fewer symmetry properties. However, it eventually leads to a faster convergence than the UHF trial wave function because symmetry has properly removed certain excitations. The multi-determinant trial wave function with symmetry leads to rapid convergence and small statistical errors. In the bottom panel, Fig. 3.6b, we show an example when there is a severe sign/phase problem. The same trends are seen, with the full symmetry trial wave function leading to rapid convergence of the projection.

With the mixed estimate, the symmetry trial wave function on the left will have zero

overlap with any wave function component in a different symmetry space. This allows one to project out explicitly lower energy states of different symmetry, and thus an opportunity to study excited states. This has been used in QMC calculations before. In the AFQMC formalism, the walkers are full Slater determinants, so that the symmetry projection can be done rigorously and explicitly for each walker. We illustrate excited state calculations in Fig. 3.7, where the converged FP results show excellent agreement with results from exact diagonalization (ED).

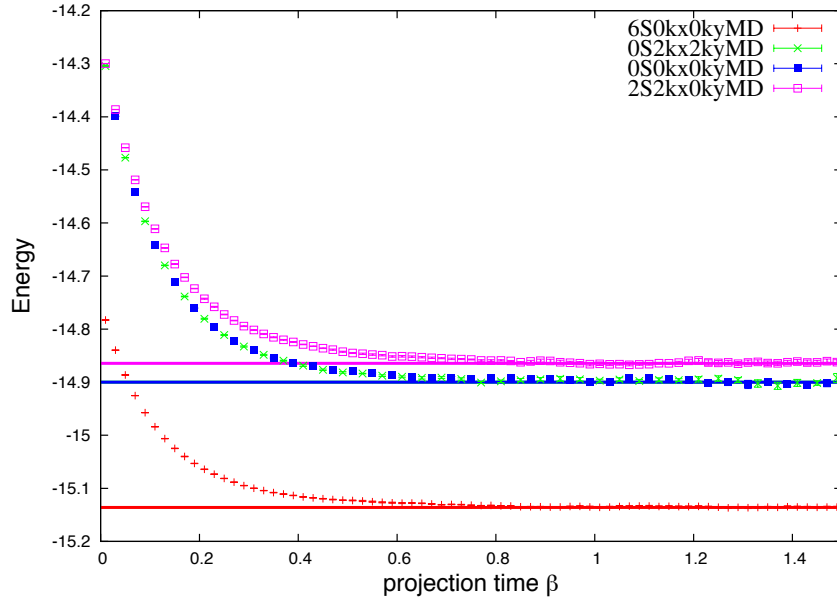


FIG. 3.7: FP calculations for the ground state and three excited states. The energy is plotted versus projection time for a  $4 \times 4$  lattice with  $N_\uparrow = N_\downarrow = 3$  and  $U = 4$ . The exact results for the ground state and the three excited state energies are shown for comparison. The symmetry of each energy level is labeled. The trial wave functions are chosen with the correct symmetry using multi-determinant. The error bars are shown but are smaller than symbol size at most points.

### 3.2.2 Trial Wave Function in CP Calculations

In CPMC, the sign or phase problem is controlled by the sign or gauge condition of the overlap with the trial wave function. The condition is approximate, and the resulting systematic error depends on the trial wave function. Thus the trial wave function has an especially important role in CP calculations. In this section, we study how trial wave functions which preserve symmetries impact the accuracy in CP calculations. As shown in prior studies [15, 47], the systematic error from the constraint is in general small for Hubbard-like systems, even when a FE or UHF trial wave function is used. In closed-shell systems in particular, the error is often negligible, as seen in the example of  $8 \times 8$  system with 26 electrons in Fig. 3.4. The systematic errors tend to be larger for open-shell systems. As we show below, the leading reason for the problem in open-shell systems seems to be symmetry in the trial wave function. The use of trial wave functions with proper symmetry often leads to a dramatic reduction in the CP error.

We use the discrete spin decomposition in Eq. (3.1) in the CP calculations, which causes “only” a sign problem, even when a twist angle is applied in the boundary condition of the supercell [47]. We first focus on small system sizes where exact results are available to make detailed and systematic comparison. Larger systems are treated later, and compared with our best results from RC calculations. In Fig. 3.8, we study the systematic error in the case of  $4 \times 4$  with  $N_\uparrow = N_\downarrow = 7$ , which has the most severe sign problem in systems that can be diagonalized presently. We study the systematic error as  $U$  goes from 0 to 12, spanning weak to moderate to strong interactions. The CP results with an FE trial wave

function is shown. (We use a small twist of opposite sign for  $\uparrow$  and  $\downarrow$  spins to generate the FE trial wave function, which breaks the SU(2) symmetry, but has translational symmetry and  $\vec{K} = 0$ .) The CP systematic error tends to grow with  $U$ , reaching about 2% of the total energy, or about 1% of the correlation energy at  $U = 12$ . As we see, the use of symmetry wave functions (obtained by diagonalizing the open-shell, leading to a total of 10 determinants) makes the CP systematic error very small across the range of  $U$ . Figure 3.5 contains a zoomed-in view, at  $U = 8$ , of the CP/SYM run and the subsequent RC which leads to an exact result. In Table 3.1, we compile the results from a variety of systems where exact diagonalization can be done to provide a quantitative measure. The CP results are compared for FE (or UHF solution obtained from a weak  $U$ ) trial wave functions and symmetry trial wave functions. Significant improvement is seen in open-shell systems, and accurate results are obtained from CP calculations.

In Table 3.1, we have included a set of results for  $4 \times 4$  and  $N_\uparrow = N_\downarrow = 8$ . There is no sign problem at half-filling. As has been discussed before [15, 47], the CP calculations can be easily made exact at half-filling (or for negative  $U$  [54]) by re-defining the importance sampling to have a non-zero minimum. However, if this were ignored and the CP algorithm applied to half-filling literally, an artificial constraint would result because the random walk cannot tunnel from one side of  $\langle \Psi_T | \phi \rangle = 0$  to the other, even though both sides are positive. The calculated energy would then show a bias, which is visible in the results shown in the table. With symmetry trial wave functions, this bias is removed even when running CP unmodified, and the CP results at half-filling are accurate.

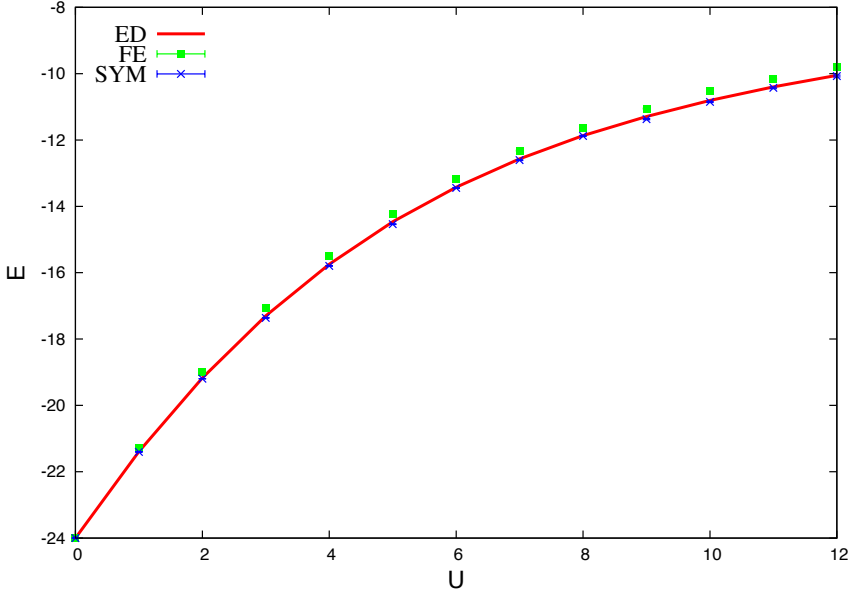


FIG. 3.8: Accuracy of CPMC in the Hubbard model as a function of interaction strength. Results are shown for the  $4 \times 4$  lattice with  $N_\uparrow = N_\downarrow = 7$  as a function of  $U$ , and compared with exact diagonalization. When the trial wave function preserves symmetry, the systematic bias in the calculated energy from the CP approximation is reduced.

The improvement of CP calculations with the symmetry trial wave function is not just to the ground-state energy. The CP bias in the observable is also significantly reduced. An example is shown in Fig. 3.9, in which we calculate the structure factor of the spin-spin correlation function in the ground state:

$$S(K) = 1/N \sum_{ij} S_i^z S_j^z \exp[iK(R_i - R_j)]. \quad (3.7)$$

As mentioned earlier, we use the back-propagation technique [15, 30] to calculate correlation functions. The result is plotted for the same  $4 \times 4$  systems for three different values of  $U$ . The peak at  $(\pi, \pi)$  indicates strong anti-ferromagnetic correlations. We see that the

CP result using UHF trial wave function shows a larger anti-ferromagnetic order, because the UHF state itself over-estimates the order. The symmetry trial wave function removes the bias and leads to results in agreement with exact diagonalization.

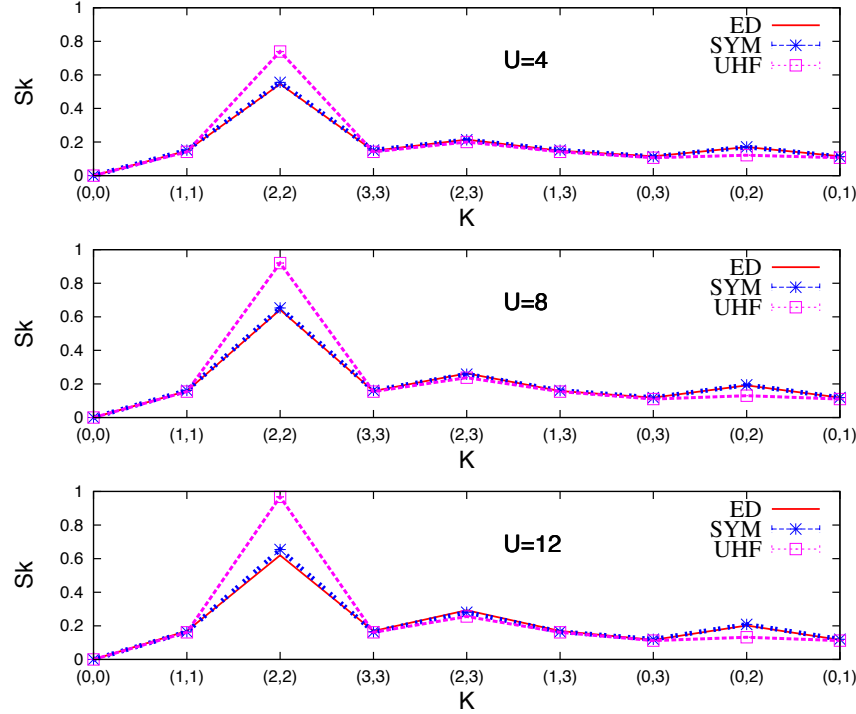


FIG. 3.9: The structure factor  $S(k)$  of the spin-spin correlation function for three interaction strengths. The system is  $4 \times 4$  with  $N_\uparrow = N_\downarrow = 7$ , and the horizontal axis labels of  $K$  are in units of  $\pi/2$ . The symmetry trial wave function has  $S^2 = 0$  and  $K_x = K_y = 0$  and B1 symmetry. CPMC has 10,000 walkers, with back-propagation  $\beta = 1$ .

### 3.2.3 Trial Wave Function in RC Calculations

Formally the role of symmetry in the trial wave function in RC calculations is similar to that in FP. However it is intimately connected to the discussion in the previous section on CP, since the initial state in RC is the converged solution from CP. The symmetry

TABLE 3.1: Computed ground-state energy per site ( $E/L$ ) from CP, with FE or UHF trial wave function (CP/FE) and with multi-determinant symmetry trial wave function (CP/SYM) respectively, compared with release-constraint (RC/SYM) and exact diagonalization results. RC/SYM uses the same symmetry trial wave function as in CP/SYM. The symmetry of the ground state is given in the last column. The statistical error bars in the QMC results are on the last digit and are shown in parentheses.

L	$(N_\uparrow, N_\downarrow, U)$	CP/FE	CP/SYM	RC/SYM	ED	$(S^2, K_x, K_y)$
$2 \times 2$	(2,1,4)	-1.60564(5)	-1.60615(3)	-1.60465(5)	-1.60463	(0.75,0,1)
$2 \times 3$	(2,2,4)	-1.38328(6)	-1.40129(4)	-1.40085(4)	-1.40087	(2,0,0)
$2 \times 3$	(2,2,8)	-1.2239(2)	-1.2463(1)	-1.2443(3)	-1.2442	(2,0,0)
$2 \times 4$	(2,2,4)	-1.36839(2)	-1.37387(2)	-1.37379(3)	-1.37383	(0,0,2)
$2 \times 4$	(3,3,4)	-1.56939(4)	-1.56942(4)	-1.56944(5)	-1.56941	(0,0,0)
$3 \times 3$	(4,4,8)	-0.7783(2)	-0.8127(1)	-0.8091(1)	-0.8094	(0,0,0)
$4 \times 4$	(2,2,4)	-0.72026(5)	-0.72094(1)	-0.72063(1)	-0.72064	(0,0,0)
$4 \times 4$	(2,2,8)	-0.7070(1)	-0.7082(1)	-0.7075(2)	-0.7076	(0,0,0)
$4 \times 4$	(2,2,12)	-0.6997(1)	-0.7010(1)	-0.7002(3)	-0.7003	(0,0,0)
$4 \times 4$	(3,3,4)	-0.93394(2)	-0.94622(1)	-0.94598(1)	-0.94600	(6,0,0)
$4 \times 4$	(3,3,8)	-0.9034(1)	-0.9208(1)	-0.9203(1)	-0.9202	(6,0,0)
$4 \times 4$	(3,3,12)	-0.8867(1)	-0.9067(1)	-0.9062(3)	-0.9061	(6,0,0)
$4 \times 4$	(4,4,4)	-1.09442(2)	-1.09693(2)	-1.09597(6)	-1.09593	(0,0,0)
$4 \times 4$	(4,4,8)	-1.0265(1)	-1.0307(1)	-1.0282(5)	-1.0288	(0,0,0)
$4 \times 4$	(4,4,12)	-0.9914(1)	-0.9962(1)	-0.9940(3)	-0.9941	(0,0,0)
$4 \times 4$	(5,5,4)	-1.22368(2)	-1.22368(2)	-1.22380(4)	-1.22381	(0,0,0)
$4 \times 4$	(5,5,8)	-1.0948(1)	-1.0948(1)	-1.0942(2)	-1.0944	(0,0,0)
$4 \times 4$	(5,5,12)	-1.0292(1)	-1.0292(1)	-1.0278(4)	-1.0284	(0,0,0)
$4 \times 4$	(6,6,4)	-1.1012(1)	-1.1104(1) <sup>1</sup>	-1.1084(2)	-1.1080	(0,0,0)
$4 \times 4$	(6,6,8)	-0.9293(1)	-0.9376(1) <sup>2</sup>	-0.9329(5)	-0.9328	(0,0,0)
$4 \times 4$	(6,6,12)	-0.8439(1)	-0.8557(1) <sup>2</sup>	-0.8507(6)	-0.8512	(0,0,0)
$4 \times 4$	(7,7,2)	-1.19584(2)	-1.19992(1) <sup>3</sup>	-1.19822(2)	-1.19821	(0,2,2)
$4 \times 4$	(7,7,4)	-0.9793(1)	-0.9863(1) <sup>1</sup>	-0.9840(1)	-0.9840	(0,0,0)
$4 \times 4$	(7,7,6)	-0.8334(1)	-0.8428(1) <sup>1</sup>	-0.8386(3)	-0.8388	(0,0,0)
$4 \times 4$	(7,7,8)	-0.7361(1)	-0.7461(1) <sup>1</sup>	-0.7417(8)	-0.7418	(0,0,0)
$4 \times 4$	(7,7,10)	-0.6687(2)	-0.6782(1) <sup>1</sup>	-0.673(2)	-0.6754	(0,0,0)
$4 \times 4$	(7,7,12)	-0.6202(2)	-0.6296(2) <sup>1</sup>	-0.627(4)	-0.6282	(0,0,0)
$4 \times 4$	(8,8,4)	-0.84225(6)	-0.85140(6)	-0.85133(6)	-0.85137	(0,0,0)
$4 \times 4$	(8,8,8)	-0.5164(2)	-0.5293(2)	-0.5291(2)	-0.5293	(0,0,0)
$4 \times 4$	(8,8,12)	-0.364(3)	-0.3741(2)	-0.3739(4)	-0.3745	(0,0,0)

<sup>1</sup>  $B_1$  symmetry is also used in  $|\psi_T\rangle$ .

<sup>2</sup>  $A_1$  symmetry is also used in  $|\psi_T\rangle$ .

<sup>3</sup>  $\hat{R}_{\pi/2}|\psi_T\rangle = \exp(i3\pi/2)|\psi_T\rangle$  symmetry is also used.

trial wave functions improves the CP approximation and the quality of the wave function sampled from CP, as indicated by the improvement in the energy and in the calculated observables. This means symmetry trial wave functions also allow better RC calculations, by providing a better initial state *and* by giving a better trial wave function in the mixed estimate in Eq. (2.17). As discussed in Sec. 3.1, we also impose symmetry with the HS transformation in RC, by switching from the Ising spin form in the CP calculation to the Gaussian form in the RC part. We find that this combination improves the quality of the RC calculations greatly in most cases. An example is shown in Fig. 3.5. Results from RC/SYM calculations are also shown in Table 3.1 for systematic comparisons with CP and with exact diagonalization results.

Figure 3.10 illustrates the behavior of RC calculations using two different trial wave functions, the UHF versus a symmetry trial wave function. A small system size of  $3 \times 3$  with  $2 \uparrow$  and  $2 \downarrow$  electrons is chosen such that the RC calculation can also be carried out explicitly to allow direct comparison. (In the explicit calculation, we propagate the CP population of  $\{|\phi_i^{\text{CP}}\rangle\}$  directly by applying  $e^{-\Delta\tau\hat{H}}$ . The propagation is carried out by expanding each walker in terms of exact eigenstates of  $\hat{H}$ .) We see that CPMC/UHF gives an energy closer to the exact value ( $\sim 0.1\%$  error) compared to CPMC/SYM ( $\sim -0.3\%$  error). The corresponding RC/UHF moves further away from the exact answer and shows no indication of convergence in the imaginary-time span in which RC/SYM is well-converged. The explicit RC calculation, as shown in the inset, reveals a highly non-monotonic behavior. The projection does converge to the correct ground-state energy, but

requiring an imaginary time of  $> 100$ . This would be impossible to reach in a QMC RC calculation because of the sign problem. Thus non-monotonic behaviors could be difficult to detect and would yield misleading results. The improvement with the symmetry trial wave function, which leads to rapid and monotonic convergence, is then especially valuable.

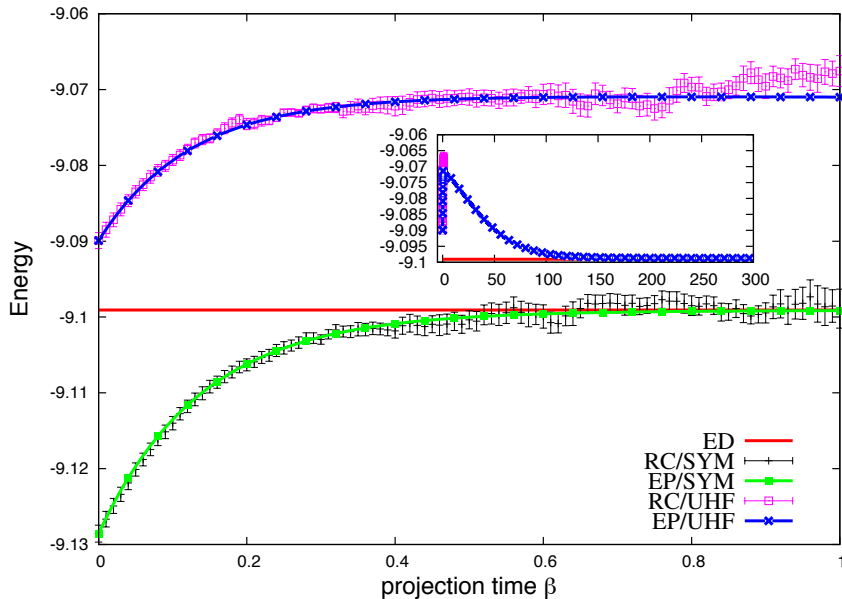


FIG. 3.10: RC calculations with symmetry trial wave functions and without. The system is  $3 \times 3$  with  $N_\uparrow = N_\downarrow = 2$  and  $U = 4$ . The symmetry trial wave function has  $S^2 = 2, K_x = 0, K_y = 0$  while the UHF wave function breaks these symmetries. CP/UHF is very accurate, but RC/UHF has non-monotonic behavior and slow convergence, as shown by the explicit propagation. RC/SYM converges rapidly and monotonically. The explicit propagation (EP) result of RC/UHF is shown to large projection time in the inset.

The use of proper symmetry can allow RC calculations of excited states, similar to the discussion in Fig. 3.7. Since CP allows one to start from an initial population much closer to the exact state, RC can be more accurate. An example is shown in Fig. 3.11, in which the many-body ground state and first excited state energies are calculated as a function of crystal momentum. Both CP and RC are done with the same trial wave function, in which

the correct symmetry is imposed. Consistent with prior experience, CP is very accurate for the ground state, although a systematic error is visible at larger twist angles. The CP result is less accurate for the excited state. With RC, the CP error is removed and the results are seen to be essentially exact.

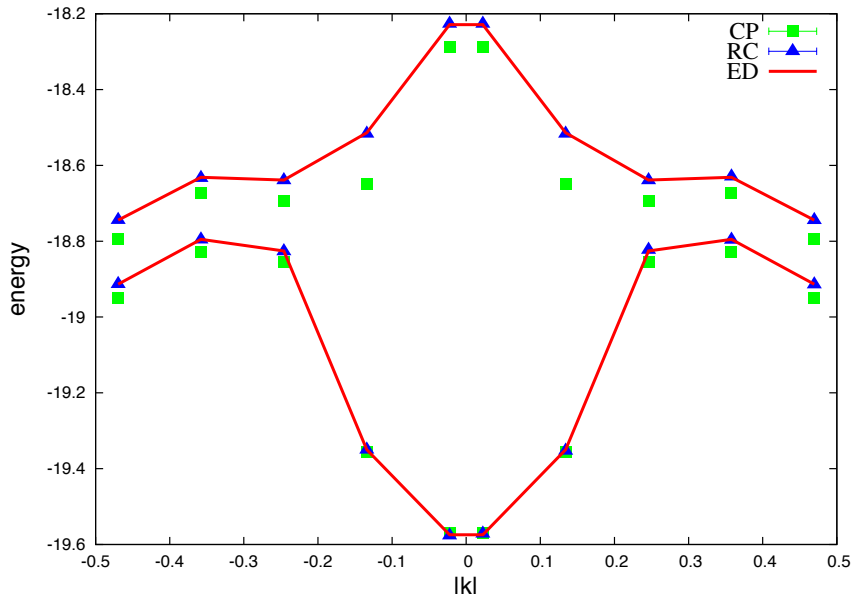


FIG. 3.11: RC and CP results for ground and the first excited state energies versus crystal momentum. RC greatly improves the calculation of excited states and band structures. The system is  $4 \times 4$  with  $N_\uparrow = N_\downarrow = 5$  and  $U = 4$ . QMC statistical error bars are smaller than symbol size. The horizontal axis gives  $|k|$  along a line cut  $k_y = 2k_x$ . Exact diagonalization results are shown for comparison. The line is to aid the eye.

### 3.3 Conclusion

In this chapter, we have studied the role of symmetry in AFQMC calculations, and discussed the imposition of symmetry from two key aspects of an AFQMC calculation, namely the HS transformation and the trial wave function. It is shown that major im-

TABLE 3.2: Energy per site in some open-shell Hubbard square lattices at  $U = 4$ . The symmetry of the ground state,  $S^2 = 0, K_x = K_y = 0$ , is preserved in the trial wave function used in CP/SYM and RC/SYM. The UHF trial wave function is generated with  $U = 0.5$  as has been done before [15].

L	$(N_\uparrow, N_\downarrow)$	CP/UHF	CP/SYM	RC/SYM
$6 \times 6$	(12, 12)	-1.18444(3)	-1.18625(3)	-1.18525(4)
$6 \times 6$	(24, 24)	0.14889(2)	0.14709(3)	0.14809(4)
$8 \times 8$	(14, 14)	-1.07173(1)	-1.07239(1) <sup>1</sup>	-1.07180(2)
$8 \times 8$	(22, 22)	-1.18580(2)	-1.18673(2)	-1.1858(2)
$10 \times 10$	(40, 40)	-1.11378(3)	-1.11468(2)	-1.1135(2)
$12 \times 12$	(58, 58)	-1.10912(3)	-1.11015(3)	-1.1089(2)

<sup>1</sup>  $B_2$  symmetry is also used in  $|\psi_T\rangle$ .

provements in efficiency and accuracy can be achieved. To allow detailed and systematic benchmark and analysis, we have used smaller lattice sizes extensively, where exact results are available. The method applies straightforwardly to larger systems. CP calculations will scale as a low power with system size; FP and RC will of course have a sign/phase problem, albeit at a much reduced level with the proposed symmetry improvements. In Table 3.2, we present CPMC energies in several open-shell systems up to  $12 \times 12$ . (For closed shell systems, the single-determinant FE trial wave function already satisfies the symmetries. They are expected to be very accurate. We have verified this in several cases with RC runs). CP/SYM and the corresponding RC results are shown. The RC results in Table 3.2 are essentially exact ground-state energies. CP/UHF results are also shown, which are comparable and even closer to the exact answer than the CP/SYM using simple symmetry trial wave functions in these systems. (As discussed, the CP/SYM leads to much better convergence in RC calculations.) This confirms the accuracy of CP/UHF as has been previously asserted.

We have discussed the general continuous Gaussian charge decomposition, which preserves spin symmetry. It is shown that the proper choice of the background  $\bar{n}$  can lead to a large reduction of the statistical fluctuations. One advantage of the spin decomposition is that, for repulsive interactions, it results in a sign problem in contrast with a phase problem for the charge decomposition. CP calculations with the spin decomposition tend to perform much better. We have emphasized the idea that the different forms can have advantages in different situations. Generally, the merits of the discrete spin and continuous charge, or indeed other forms of the HS transformation, will depend on the actual problem and physics. However, preserving the right symmetry is highly valuable, as we have demonstrated. Especially worth noting is that the switch to charge-decomposition within a CP calculation of spin-decomposition produces much better RC performance over many parameter ranges.

We have shown the importance of having trial wave functions which preserve symmetry. These trial wave functions accelerate convergence, allow better calculations of excited states, can significantly reduce the CP systematic error, and make possible systematically improvable RC calculations. The approach we have taken to generate trial wave functions that preserve symmetry, the equivalent of a small CASSCF calculation in quantum chemistry, has provided a proof-of-concept. In addition, they have already allowed calculations in significant system sizes for physically important regimes (low doping), as shown in Table 3.2. However, for general open-shell situations, the CASSCF approach does not scale well. The resulting number of Slater determinants in the trial wave function will grow

rapidly with system size. Several alternatives are possible, including projected BCS wave functions [54] and projected Hartree-Fock wave functions [55, 56].

The development presented in this chapter will allow many applications even in its current form. Although we have focused on zero-temperature methods, many of the ideas will also apply to finite-temperature calculations [12, 58]. The formula can be directly mapped from the  $U>0$  case we discussed to  $U<0$  with a particle-hole transformation. Indeed the principle works for any other two-body interactions. The CP/SYM calculations and the RC/SYM from it represent a major step forward, as we can now have internal checks and a systematically improvable computational method capable of reaching two- and three-dimensions and large system sizes.

# CHAPTER 4

## Infinite Variance in QMC

In this chapter, we show that the commonly employed Metropolis forms of the determinantal QMC approach, have MC variances that diverge. Since the MC statistical error is proportional to the variance, the divergence makes it impossible to obtain a correct estimate of the error bar, thereby rendering the MC results unreliable. The results obtained by ignoring the problem can turn out to be reasonable, as we illustrate below. However, the computation cannot internally determine whether this will be the case and, in a strict mathematical sense, the result is not meaningful without controlling the problem. The extent of the problem can differ for different models, observables, and algorithms, but the fundamental problem appears to be generic in standard path-integral determinantal QMC calculations.

We illustrate the infinite variance problem, discuss its origin, and examine ways to detect it. A method is then proposed to solve the problem, which is straightforward to

implement within the standard algorithms. The work here provides a robust approach for all the situations mentioned above where standard determinantal QMC algorithms are applied to sign-problem-free fermion systems. Further, the ideas can be potentially useful in many other MC simulations (wherever the function being sampled might contain zero values).

## 4.1 Symptoms and Origin of the Problem

In this section, we illustrate the infinite variance problem with calculations on the Hubbard model defined in Eq. (2.1). With a repulsive interaction ( $U > 0$ ), there is no sign problem on a bipartite lattice at half-filling. For illustrative purposes, we have selected an arbitrary small system, a  $2 \times 4$  supercell, with  $U/t = 4$ . The characteristics of the results discussed and the underlying issues are general and independent of the details of the system or the calculation. We compute the total ground-state energy of the system in 100 independent calculations. Each calculation carries out, by Metropolis MC sampling of the path-integral form, the imaginary-time projection from an initial wave function taken to be the ground state of the non-interacting system. The total imaginary time of the projection in each calculation is  $\beta = 81$ , with  $\Delta\tau = 0.01$  (in units of  $t$ ). After discarding an initial equilibration phase, we perform 50 sweeps along the path measuring the energy between 0 and  $81t$  with an interval of  $0.9t$  of imaginary time.

From this standard analysis procedure, one obtains the expectation value from the average of the 100 data points. The statistical error bar is given, based on the Central

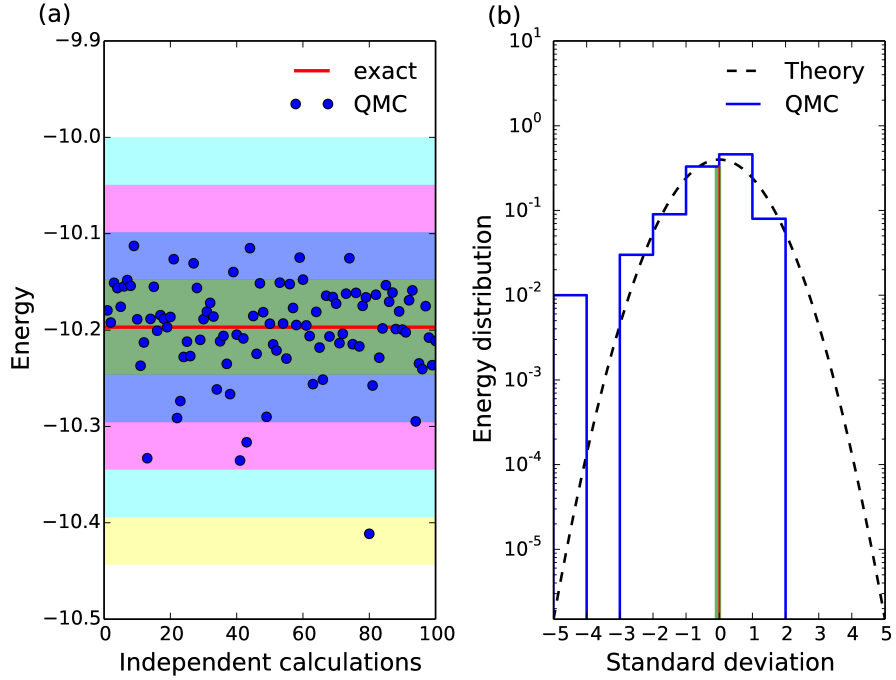


FIG. 4.1: Distribution of the computed ground-state energies from 100 independent determinantal QMC calculations. In the left panel, each shade band indicates one standard deviation, as computed from the 100 data points, which are plotted vs. the (arbitrary) run index. In the right panel, the histogram of the 100 data points are shown with a bin size of the computed standard deviation. For comparison, the theoretical Gaussian distribution from the CLT is also shown. (A shift is applied on the horizontal axis so that the exact result is shown at zero, the vertical red line.) The computed mean from the 100 data is shown by the vertical green line, with its thickness indicating the statistical error bar. Note the logarithmic scale on the vertical axis.

Limit Theorem (CLT), by the standard deviation divided by  $\sqrt{100 - 1}$ . Our final result is  $-10.199 \pm 0.005$ . This implies that, for example, the probability that the exact result is within one MC error bar of the computed expectation is  $\sim 68.27\%$ , the probability that it is outside of two error bars is 4.55%, etc. The exact result is  $-10.197$  (a twist boundary condition, with a small twist angle of  $\Theta = (0.03, 0.02)$ , was applied to the Hamiltonian to break the open-shell degeneracy [47]), and our results look quite reasonable.

However, as seen from Fig. 4.1, the data exhibit several anomalies. The distribution of

the MC data is not symmetric about the expectation value. One data point falls outside four standard deviations from the mean, the probability for which should be less than 0.007%. Overall, the  $\chi^2$  between the two distributions in the right panel of Fig. 4.1, namely the histogram from binned data and the theoretical distribution according to the CLT, is 342.1, which indicates that it is highly unlikely that the two are consistent. The disagreement means that although our final result happens to be consistent with the exact result, the MC estimates of the mean and statistical error bar could have been catastrophically wrong.

We have tested many different system sizes and interaction strengths, several different models, different forms of HS transformations, and measuring observables other than the energy, to confirm the above observations. The behavior appears quite general in standard determinantal QMC calculations.

In the metropolis algorithm discussed in Sec. 2.4, one computes the variance to estimate the statistical error bar:

$$\sigma_{\hat{O}}^2 = \frac{\int \frac{g^2(\mathbf{X})}{f(\mathbf{X})} d\mathbf{X}}{\int f(\mathbf{X}) d\mathbf{X}} - \langle \hat{O} \rangle^2 \doteq \left\langle \left( \frac{g}{f} \right)^2 \right\rangle_f - \left\langle \frac{g}{f} \right\rangle_f^2, \quad (4.1)$$

where on the right we have omitted the variable  $\mathbf{X}$  but the averages have the same meaning as in Eq. (2.24). (In practice the configurations sampled will have auto-correlations, and one will need to re-block the measurements to obtain a reliable estimate, as is commonly done. This is always done in our data analysis in the present work. It does not affect the following discussions.)

The variance in Eq. (4.1), as given by the explicit formula on the left, can diverge if  $g(\mathbf{X})$  remains non-zero when  $f(\mathbf{X})$  approaches zero. More precisely, it diverges if a non-integrable singularity exists in  $g^2/f$  anywhere in the space of the auxiliary-field paths. This can occur because  $f$  is given by the overlap between two single Slater determinant wave functions,  $|\phi^l\rangle$  and  $|\phi^r\rangle$ , which are randomly evolving. The existence of paths with  $f(\mathbf{X}) = 0$  is related to the occurrence of the sign problem in calculations of general fermion problems in this framework. The symmetry which prevents the sign problem from occurring in the sign-problem-free cases eliminates the part of the space where  $f(\mathbf{X}) < 0$ ; however, this symmetry in general does not exclude  $f(\mathbf{X}) = 0$ . In the example in Sec. 4.1, both  $|\phi^l\rangle$  and  $|\phi^r\rangle$  can be written as  $|\phi_\uparrow\rangle \otimes |\phi_\downarrow\rangle$ , where  $|\phi_\downarrow\rangle$  can be made equal (or complex conjugate) to  $|\phi_\uparrow\rangle$  under partial particle-hole transformation [59]. This means that  $f(\mathbf{X})$  can be written in the form of  $|\langle\phi_\downarrow^l|\phi_\downarrow^r\rangle|^2$  for any path  $\mathbf{X}$ , and thus is non-negative. It does not mean, however, that  $f(\mathbf{X})$  cannot be zero, which occurs whenever  $|\phi^l\rangle$  and  $|\phi^r\rangle$  become orthogonal. This is inevitable, since they are two independent single-Slater determinant wave functions controlled by separate stochastic paths  $\mathbf{X}_l$  and  $\mathbf{X}_r$ , respectively.

This divergence is the origin of the symptoms seen in the calculation in Sec. 4.1. It causes the underlying variance of the calculation to diverge. It is important to emphasize that the infinite variance problem is not caused by a path with  $f(\mathbf{X}) = 0$  being encountered in an actual calculation. In the MC calculation points with  $f(\mathbf{X}) = 0$  are, of course, never sampled. The expectation value  $\langle g/f \rangle$  exists, and will converge to the correct answer. The infinite variance problem arises because paths are sampled which come close to  $f(\mathbf{X}) = 0$ .

TABLE 4.1: MC results for the toy problem in Eq. (4.2) at  $\alpha = 0$ . The PDF  $2x$  is sampled on  $(0, 1)$ . The MC statistical error bars (one standard deviation) are estimated from 100 independent runs.

Sample size	Computed value $\langle y(0) \rangle$	Error bar
5000	5.0064	0.0089
20000	4.9939	0.0047
80000	4.9997	0.0026
320000	5.0011	0.0014
1280000	5.0021	0.0009

Although the computed variance, using  $\langle (g/f)^2 \rangle$ , will always have a finite numerical value in each calculation, it will have sporadic large fluctuations. The variance is an intrinsic property of the underlying probability distribution function (PDF) being sampled, so the problem does not depend on which sampling algorithm is used. The more samples generated, the more likely the divergence will manifest itself. Hence the computed error bar, which is obtained by  $\sigma$  divided by the number of effective independent samples, does not provide a reliable estimate of the MC statistical error.

## 4.2 Illustration from a Toy Model

In this section we illustrate several key aspects of the infinite variance problem by studying a toy problem. Let us consider the following expression involving simple one-dimensional integrals,

$$y(\alpha) = \frac{\int_{\alpha}^1 (x+2) dx}{\int_{\alpha}^1 x dx}, \quad (4.2)$$

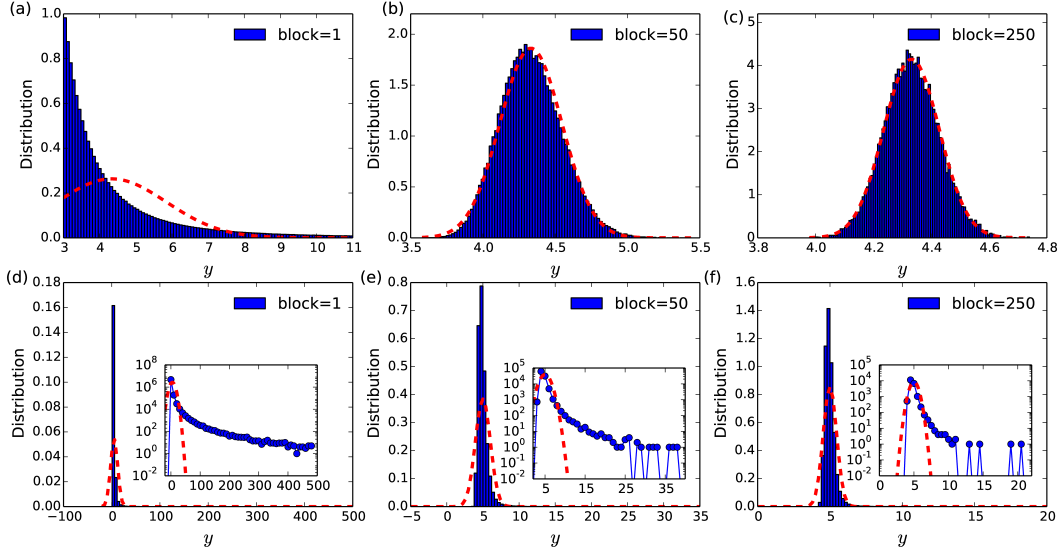


FIG. 4.2: Normalized histograms of MC measurements for  $\alpha = 0.2$  (top row) and  $\alpha = 0.0$  (bottom row). The calculations at each  $\alpha$  are done with  $5 \times 10^6$  MC samples. Each histogram is obtained by grouping a different number ("block") of samples together to make one entry of  $\langle y(\alpha) \rangle$ . In the top row, they converge quickly to Gaussian distributions as "block" is increased, and reach agreement with the red (dashed) curves, which indicate the Gaussian as defined according to the CLT. In the bottom row, in contrast, the histograms do not converge to Gaussians. A persistent discrepancy is seen between the CLT prediction and the data. The insets, which display the unnormalized histogram values (semi-log scale), highlight the long tail on the right.

where  $\alpha \in [0, 1)$  is a parameter which we will vary. Eq. (4.2) can be viewed as a special case of Eq. (2.23), with  $f(x) = x$  and  $g(x) = x + 2$ .

Mimicking the QMC calculations, we will choose to sample the PDF  $x/(\int_{\alpha}^1 x dx)$  and evaluate  $y(\alpha)$  by MC, i.e., the expectation of  $(x + 2)/x$  from the samples. The exact value is  $y(\alpha) = (5 + \alpha)/(1 + \alpha)$ . The variance is

$$\begin{aligned} \sigma_{y(\alpha)}^2 &= \frac{\int_{\alpha}^1 (x + 2)^2/x dx}{\int_{\alpha}^1 x dx} - y^2(\alpha) \\ &= -\frac{8 \ln \alpha}{1 - \alpha^2} - \frac{16}{(1 + \alpha)^2}. \end{aligned} \quad (4.3)$$

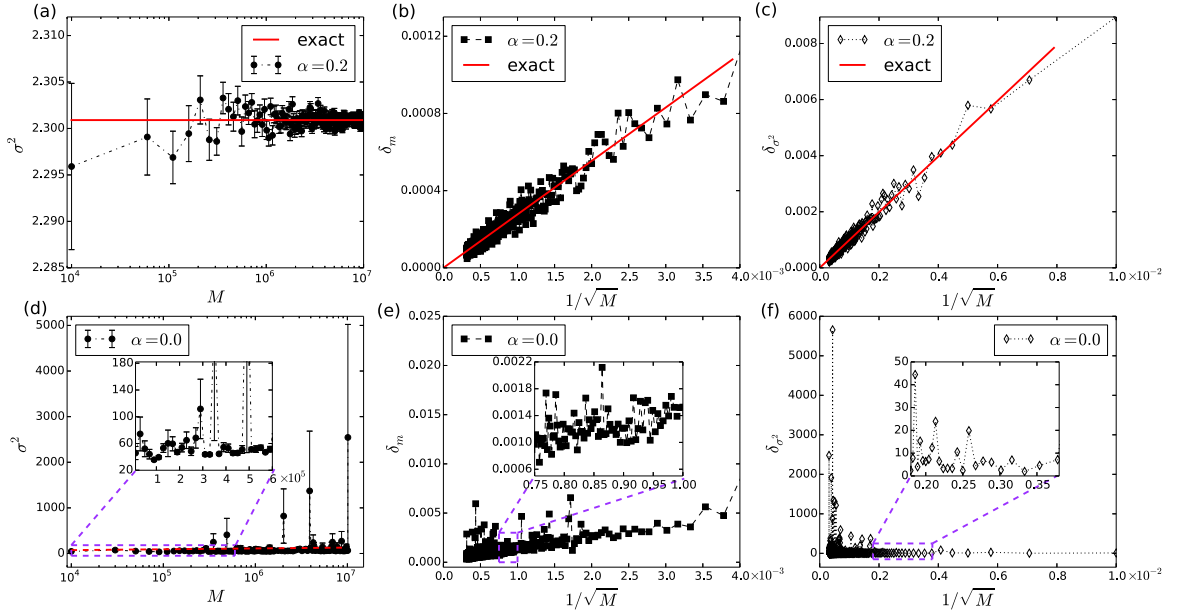


FIG. 4.3: Comparison of finite and infinite variance calculations. The variance, statistical error on the expectation value, and the statistical error on the computed variance are shown for  $\alpha = 0.2$  (top row) and  $\alpha = 0$  (bottom row). The statistical errors are estimated from 30 independent MC runs. For  $\alpha = 0.2$ , the computed variance remains consistent with analytic results as the sample size  $M$  is varied, and the computed statistical errors on the variance and on the expectation values decreases as  $1/\sqrt{M}$ . For  $\alpha = 0$  the MC variance shows increasing fluctuations as  $M$  is increased, and does not converge. (As a guide, the dashed red line plots Eq. (4.3) with  $\alpha$  replaced by  $1/M$ .) The statistical errors do not decrease following  $1/\sqrt{M}$ , as is especially evident in the error on the variance.

As  $\alpha \rightarrow 0$ , the expectation  $y(\alpha) \rightarrow 5$  is well defined, while the variance diverges as

$$\sigma_{y(\alpha)}^2 \rightarrow -8 \ln(\alpha).$$

This divergence is not straightforward to detect in the MC calculation. The logarithmic divergence is a consequence of samples landing close to  $f(x) = 0$  (i.e.,  $x$  being near the origin). Statistically this occurs more as the sample size grows. On the other hand, the standard deviation of the computed expectation value, in the absence of the divergence, will decrease as the square root of the sample size. In the competition between the two trends, the logarithm is slower so the latter dominates. Table 4.1 displays the result ob-

tained from actual MC calculations at  $\alpha = 0$ . The expectation values are obtained from averaging 100 independent runs, each with the specified sample size, and the error bar is estimated by the standard deviation of the 100 results divided by  $/\sqrt{99}$ . Similar to the situation in the Hubbard model in Sec. 4.1, the results look reasonable at first glance. The error bar is seen to decrease as the sample size is increased, roughly as the square root, although the largest calculation gives a result which is away from the correct answer by more than two error bars.

In Fig. 4.2 we examine the behavior of the calculations more closely, and compare it to that of a case with no variance problem ( $\alpha \neq 0$ ). In each calculation a total of  $M$  samples are drawn from the PDF. We group the samples into blocks each with  $M_b$  samples, and compute the MC estimate of  $y(\alpha)$  for each block. These are entries for the histogram with "block" number  $M_b$ . Thus the first histogram in the top row contains  $M$  entries of  $(x + 2)/x$ , each computed at an  $x$  value sampled from the PDF  $f(x) \propto x$ , with  $x \in (\alpha, 1)$ . In the next histogram, each entry is obtained from an average  $\langle (x + 2)/x \rangle$  of  $M_b = 50$  samples, and there are  $M/M_b$  entries. This procedure of re-blocking or re-binning is common in QMC calculations where auto-correlation is present. (If successive MC samples are not correlated, different ways of re-blocking will lead to statistically equal error estimates.) For each re-blocking step, the variance between the block means can be computed numerically, following the right-hand side of Eq. (4.1) (with the block mean values replacing  $g/f$ ) and averaging over all the blocks.

As seen from the top row in Fig. 4.2, for  $\alpha = 0.2$  the behavior is consistent with

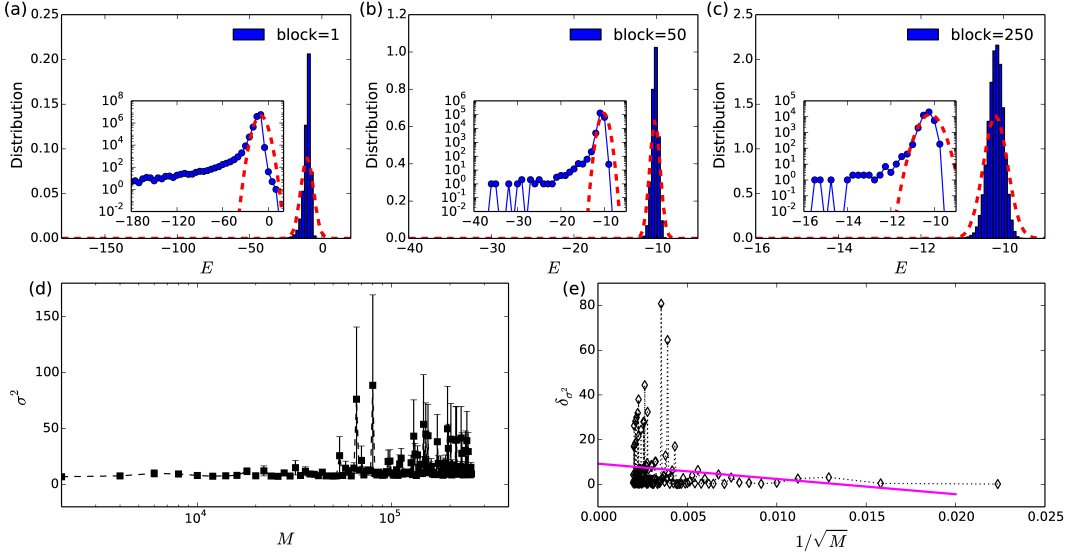


FIG. 4.4: Detection and further analysis of the infinite variance problem in the Hubbard model calculation in Sec. 4.1. The top panel shows a re-blocking analysis similar to that in Fig. 4.2. The histograms of the computed ground-state energy do not converge to Gaussians and do not follow the CLT. In the bottom panel, the computed variance and the statistical error on the variance are shown vs. sample size, similar to Fig. 4.3. The variance does not converge to a finite value. Its error bar grows with sample size in contrast with the expected  $1/\sqrt{M}$  decay. (The magenta line is a linear fit.)

what is expected from the CLT. As  $M_b$  is increased, the histograms converge to Gaussian distributions given by the overall mean and the standard deviations computed from the entries. For  $\alpha = 0$ , however, the behavior is different. The histograms do not converge to Gaussian distributions with re-blocking. A persistent tail is present, and the standard deviations and the MC error estimates obtained according to the CLT do not give a correct description of the actual data.

Figure 4.3 further analyzes the behaviors of the variance. For each  $\alpha$ , we compute the variance and the expectation value systematically for increasing sample sizes. In other words, a sequence of  $\langle y(\alpha) \rangle$  and  $\sigma_{y(\alpha)}^2$  are obtained as we vary the number of samples,  $M$ ,

used in Eqs. (2.24) and (4.1). To estimate the statistical errors on  $\langle y(\alpha) \rangle$  and  $\sigma_{y(\alpha)}^2$  for each choice of  $M$ , we carry out 30 independent MC calculations and compute the corresponding standard deviations. (Note that this applies to any observables in any QMC calculations. An estimate of the error bar can always be obtained by repeating the calculations with different random number seeds a number of times and computing the standard deviation of the corresponding observable from them.) We see from the first panel in the figure that, at  $\alpha = 0.2$ , the computed variance agrees with the exact value of  $\sigma^2 = 2.30087$  from Eq. (4.3), regardless of the sample size. The error bar on the computed variance decreases with sample size. Indeed the error bar is proportional to  $1/\sqrt{M}$  as shown in the last panel in the top row. Similarly, the statistical errors on the computed expectation value agree with  $\sigma/\sqrt{M}$ , as shown in the second panel. For  $\alpha = 0$ , the situation is different. Though a well defined expectation value still exists, the computed variance does not show convergence with increasing sample size. Large fluctuations are seen at large  $M$  on the computed statistical errors of both the expectation value and, especially, the variance. (The calculations were done with a different set of points for each  $M$ .) This is understandable, since larger  $M$  makes it more likely to have samples which land ever closer to the origin.

The toy problem is of course rather artificial. To what extent it captures the characteristics of determinantal QMC is not immediately clear. Because of the non-orthogonal and over-complete nature of  $|\phi^l\rangle$  and  $|\phi^r\rangle$ , less is known about the behavior of  $f(x)$  and how it approaches zero than that of wave functions written in coordinate space (which

tend to vanish linearly at the node) [60]. In Fig. 4.4 a similar analysis is performed on the Hubbard model calculations described in Sec. 4.1. In the top panels histograms of the computed ground-state energy,  $E$ , are shown from re-blocking, again with the inset showing the long tails (which are on the left since the energy is negative here). In the bottom panels, the variance is computed with increasing MC sample size, following a similar procedure to that used in Fig. 4.3. The estimated statistical error on the computed variance shows large fluctuations and does not resemble a  $1/\sqrt{M}$  behavior. As we see there is a striking similarity between the behaviors of the real determinantal QMC calculations and the toy model.

### 4.3 Solution

Conceptually it is straightforward to avoid the infinite variance problem. One should modify the PDF which is sampled by MC so that it is non-zero in the entire configuration space (or at least find one that only leads to an integrable singularity in the estimator). One example would be to shift the PDF, i.e., to sample

$$f'(\mathbf{X}) = \frac{f(\mathbf{X}) + \eta}{\int [f(\mathbf{X}) + \eta] d\mathbf{X}}, \quad (4.4)$$

where  $\eta$  is a small constant. One could also modify  $f$  to set a minimum value such as  $f'(\mathbf{X}) \propto \max\{f(\mathbf{X}), \eta\}$ . Yet another example would be to sample

$$f'(\mathbf{X}) \propto f(\mathbf{X}) + \gamma|g(\mathbf{X})|, \quad (4.5)$$

where  $\gamma$  is a constant which can be tuned to minimize the variance of the desired expectation value or a set of expectation values. One example is the worm algorithm [61], which uses this form as an elegant way to expand the sampled phase space beyond that defined by  $f$ . Under the new PDF  $f'$ , the observable in Eq. (2.23) can be estimated by computing the integrals in the numerator and denominator separately,

$$\langle \hat{O} \rangle = \frac{\langle g(\mathbf{X})/f'(\mathbf{X}) \rangle_{f'}}{\langle f(\mathbf{X})/f'(\mathbf{X}) \rangle_{f'}}, \quad (4.6)$$

where the averages are with respect to samples from the new PDF  $f'(\mathbf{X})$  as indicated. These and related tricks have been used in different contexts [49, 36, 62] where a zero needs to be avoided in the function being sampled.

Any of the choices above would solve the toy problem of Eq. (4.2). In realistic sign-problem-free QMC calculations, however, these approaches in general do not work well. The function  $f(\mathbf{X})$  in these cases tends to span an enormous range. For example, we observe that the unnormalized  $f(\mathbf{X})$  can vary from  $\exp(-50)$  to  $\exp(50)$  during a typical simulation in a lattice of moderate size. The range grows exponentially with system size (physical size or imaginary time/inverse temperature). This makes it difficult to choose a

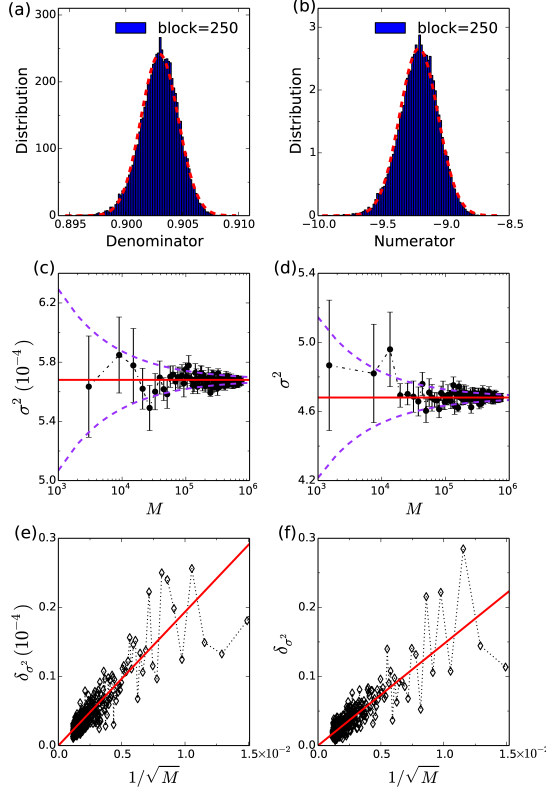


FIG. 4.5: The new method applied to the problem in Fig. 4.4. The top row shows histograms of the expectation values in the (a) denominator and (b) numerator of the new ground-state energy estimator, compared with the CLT analysis. The middle row shows the respective variances, together with the computed error bars on the variances, versus sample size. The purple dashed lines, which plot  $s/\sqrt{M}$ , indicate the expected behavior of the error bars. The bottom panel plots the size of the computed error bars on the variances vs.  $1/\sqrt{M}$ . The red solid lines show a linear fit, whose slopes give the values of  $s$  above, for the denominator and numerator, respectively.

“suitable” value of  $\eta$ , which can depend sensitively on the specific calculation. The choice can be either too small (no effect on reducing the variance) or too large (inefficient sampling in a large part of the configuration space and hence large variance). A reasonable choice for one can become ineffective for a different calculation (different physical system, or even run parameters). In principle the approach in Eq. (4.5) could work better if a suitable  $g(\mathbf{X})$  is found. For example, we tested the case  $\hat{O} = \hat{H}$  in the function in Eq. (2.22).

This was difficult to implement and it slowed down the computation significantly. If one keeps the measurement of  $\hat{H}$  at a fixed location on the path, say, at  $l = L/2$ , one has to re-compute large segments of the path for a two-body expectation for every update, which is done in sweeps across the path. If one allows the position  $l$  to vary, the effective function in the PDF is  $g(\mathbf{X}, l)$ , for which detailed balance is less straightforward to maintain.

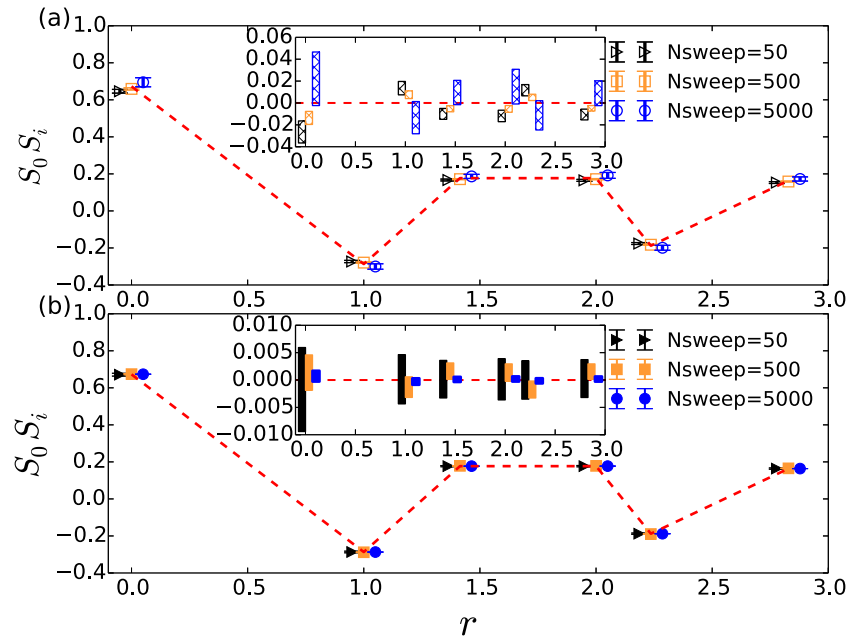


FIG. 4.6: Comparison between the standard (top panel) and new (bottom panel) methods for spin correlations in the  $4 \times 4$  Hubbard model with periodic boundary conditions and  $U = 8t$ . Results from exact diagonalization are shown by the red dashed lines. The insets show the deviations from ED. The three separate QMC results in each set, with increasing sample size, are displayed with small horizontal shifts for clarity. In the new method the statistical error bars decrease as expected, while with the standard algorithm a drastic increase is seen in the largest run. Note that the vertical scale in inset (a) is five times that in inset (b).

Here we propose a simple solution to overcome the infinite variance problem which requires minimal modifications to the standard algorithm. From Eq. (2.21), let us introduce

an intermediate function:

$$F(\mathbf{X}) = P(\mathbf{X}) \langle \phi^l(\mathbf{X}_l) | e^{-\Delta\tau\hat{H}} | \phi^r(\mathbf{X}_r) \rangle. \quad (4.7)$$

We then define a new PDF to be used in the MC:

$$f'(\mathbf{X}; x') \propto P(\mathbf{X}) \langle \phi^l(\mathbf{X}_l) | p(x') \hat{B}(x') | \phi^r(\mathbf{X}_r) \rangle, \quad (4.8)$$

which contains an extra auxiliary-field  $x'$ . The function  $F(\mathbf{X})$  implicitly depends on the location  $l$  where the propagator  $e^{-\Delta\tau\hat{H}}$  is inserted. The new PDF, on the other hand, does not distinguish where  $x'$  is inserted. It is simply the PDF that lives in a larger auxiliary-field space, identical to a path integral with  $(L + 1)$  time slices. Using Eq. (2.4) and Eq. (2.5), we obtain that

$$F(\mathbf{X}) = C \int f'(\mathbf{X}; x') dx', \quad (4.9)$$

where  $C$  is a normalization constant (which will not need to be determined in the calculation).

We can now write the original expectation value in Eq. (2.23) as

$$\langle \hat{O} \rangle = \frac{\iint \frac{g(\mathbf{X})}{F(\mathbf{X})} f'(\mathbf{X}; x') dx' d\mathbf{X}}{\iint \frac{f(\mathbf{X})}{F(\mathbf{X})} f'(\mathbf{X}; x') dx' d\mathbf{X}}. \quad (4.10)$$

The identity is easily verified by performing the integrals over  $x'$ , using Eq. (4.9). This

leads to the MC estimator

$$\langle \hat{O} \rangle = \frac{\langle g(\mathbf{X})/\mathcal{F}(\mathbf{X}) \rangle_{f'}}{\langle f(\mathbf{X})/\mathcal{F}(\mathbf{X}) \rangle_{f'}}, \quad (4.11)$$

where the average is with respect to the PDF  $f'(\mathbf{X}; x')$ , which is sampled in the expanded space of auxiliary-field paths containing an additional time slice. The basic idea of the new algorithm is thus:

1. Set up the calculation with one more time slice than originally needed.
2. Update the entire path of  $(L + 1)$  time slices as usual.
3. Whenever a measurement is made, the time slice where the measurement takes place is the “extra” time slice, which we shall refer to as the “bridge” link. Its auxiliary-field configuration  $x'$  should be ignored, i.e., the corresponding  $B(x')$  should be excluded in forming  $f(\mathbf{X})$ ,  $g(\mathbf{X})$  and  $\mathcal{F}(\mathbf{X})$ .

The “bridge” link is thus dynamic, moving along the path with the update sweeps. This is a crucial difference from the approach of Eq. (4.5). Note that the integrals in Eq. (4.10) are automatically evaluated by MC when we perform the sampling in the expanded space of  $\{\mathbf{X}, x'\}$  and ignore  $x'$  in step (3). Computing  $\mathcal{F}(\mathbf{X})$  in Eq. (4.11) requires the expectation value of  $\exp(-\Delta\tau\hat{H})$ . We do so by expanding it in terms of  $\Delta\tau$ . In most calculations this was done up to second order, which we found to be sufficiently accurate. We discuss this point further in Sec. 4.4.

The purpose of the intermediate function  $\mathcal{F}$  is to remove any singularities in the expectations in Eq. (4.11), without having to introduce a PDF that would decrease sampling

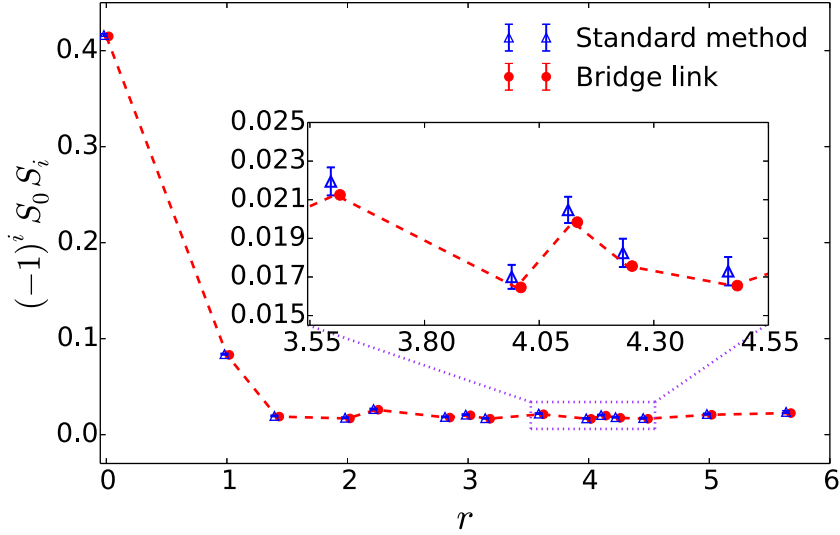


FIG. 4.7: Comparison of the standard and new algorithms: spin correlations (staggered) in a larger lattice. Results from the two sets of calculations are shown side-by-side, with a small horizontal shift for clarity. To aid the eye, those from the new method are connected by a red dashed line. The system is an  $8 \times 8$  Hubbard model with periodic boundary condition and  $U = 0.5t$ . The inset shows a zoom of the segment indicated by the dotted purple rectangular box.

efficiency drastically or increase the complexity of the algorithm substantially. The form of the PDF should scale properly to the thermodynamic limit, and its performance should remain consistent as system size and imaginary time length are varied. These are accomplished with the form in Eq. (4.7), for a broad class of problems. It is easy to see that the function  $F(\mathbf{X})$  removes the zeros present in  $f(\mathbf{X})$ . From Eqs. (4.9) and (4.8),  $F(\mathbf{X})$  is a linear combination (over an infinite/large number of auxiliary-fields  $x'$ ) of terms of the form  $\langle \phi^l(\mathbf{X}_l) | \hat{B}(x') | \phi^r(\mathbf{X}_r) \rangle$ . Each term in the integral/sum is non-negative. If the overlap between  $\langle \phi^l |$  and a single determinant in the sum,  $\hat{B}(x') | \phi^r \rangle$ , is zero for a particular  $x'$ , there will be different random values of  $x'$  which will give non-zero contributions in the sum.

For the energy, the estimator  $g/F$  in the numerator in Eq. (4.11) has the form  $\langle \phi^l | \hat{H} | \phi^r \rangle / \langle \phi^l | e^{-\Delta\tau \hat{H}} | \phi^r \rangle$ . It is easy to see that, to leading order in  $\Delta\tau$ , this is bounded by  $-1/\Delta\tau$  (relative to the mean or trial energy). It is worth emphasizing that the situation here is fundamentally different from that in DMC [63] or in phase-free AFQMC [29] where one could encounter occasional walkers with large local energies. In those cases there is no infinite variance problem, as we further discuss in Sec. 4.4. To control the spurious fluctuations, one may apply a cutoff of  $\mathcal{O}(1/\sqrt{\Delta\tau})$  on the local energies [64, 41] or use an estimate of the integral of the local energy over the time step [64]. The key distinction is that there the problem has a well-defined limit as  $\Delta\tau \rightarrow 0$ , while here any artificial bounds applied on the local energy will give back the infinite variance problem as one attempts to relax or extrapolate the bound to remove the bias it introduces.

In Fig. 4.5 we show results of the new method applied to the example of Fig. 4.4. The histograms are shown for both the numerator and the denominator in Eq. (4.11) for the ground-state energy. For brevity, results are only shown for one re-blocking size. It is seen that both approach perfect Gaussians in agreement with the CLT results. The MC variances and the error bars on the variances are computed for both. The variances converge as we increase the sample size, with the error bars on the variance decreasing as  $1/\sqrt{M}$ . In other words, all the infinite variance symptoms have been removed. The behavior of the calculation is fundamentally different from before, and is consistent with that of a finite, well-defined variance.

We next illustrate the problem and solution in calculations of physical quantities

besides the energy. A direct measure of magnetic order is the spin-spin correlation function

$$\mathbf{S}_0 \cdot \mathbf{S}_i = S_0^z S_i^z + \frac{1}{2}(S_0^+ S_i^- + S_0^- S_i^+), \quad (4.12)$$

with  $S_i^z = (n_{i\uparrow} - n_{i\downarrow})/2$ ,  $S_i^+ = c_{i\uparrow}^\dagger c_{i\downarrow}$ , and  $S_i^- = c_{i\downarrow}^\dagger c_{i\uparrow}$ . The site '0' is an arbitrary reference site and can be averaged over. The site  $i$  is varied through the supercell, with its relative distance to site 0 denoted by  $r$ . Thus far in the HS transformation, we have employed the spin decomposition, which is the more commonly adopted form in the repulsive Hubbard model. Below we will use the charge decomposition instead, which exhibits more severe symptoms of the infinite variance problem, to highlight the different features of the calculations *with* and *without* the bridge link. The two sets of calculations will use otherwise identical settings, to compare the computed spin-spin correlation functions.

In Fig. 4.6 we first show results in a  $4 \times 4$  system, where exact diagonalization can be carried out for comparison. (The QMC calculations used a finite  $\Delta\tau = 0.01$  in units of  $t$ . The resulting Trotter error is negligible on the scale of the main plots. In the insets a shift has been applied to the ED results to account for it.) Within each panel, three QMC calculations are shown, with the number of independent measurements contained in the final result (denoted by the number of sweeps in each measurement block, Nsweep) increasing by a factor of 10 every time. The CLT dictates that the statistical error should decrease by roughly  $1/\sqrt{10}$  between the successive runs. In the standard algorithm (top panel), the computed error bar is seen to decrease first but to rise dramatically in the largest run with Nsweep= 5,000. (Note also the significantly higher than expected number

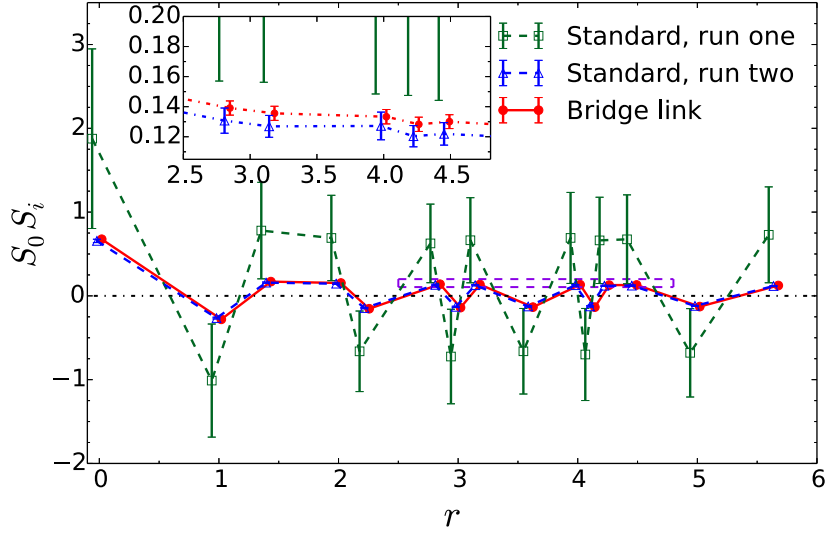


FIG. 4.8: Accurate and reliable predictions of long-range order. The main figure plots spin correlations at  $U = 8t$ , again for an  $8 \times 8$  Hubbard model. The inset is an enlargement of the part indicated by the dashed box. The two runs from the standard algorithm with different random number sequences but otherwise identical parameters show drastically different results. The new algorithm, using the same parameters, provides results with small and reliable error estimates to allow determination of the magnetic correlations.

of data points outside one error bar in the first two runs.) The new method with bridge links eliminates the problem. The computed correlation functions are in agreement with exact results. The error bars decrease with increasing Nsweep as expected. In the run with 5,000 sweeps, the results are about a factor of 30 more accurate than those from the standard algorithm. This would translate into, nominally, a factor of  $\sim 1,000$  savings in computing time. Of course the issue is much more fundamental than a quantitative gain, since the infinite variance means that the results from the standard algorithm cannot be assured of correctness within the context of its quoted error bars.

In Fig. 4.7 we show results for a larger lattice. A smaller value of  $U$  is studied, where the antiferromagnetic order is weaker and higher accuracy is needed to resolve

the order parameter (the magnetization, which can be thought of as the square root of the magnitude of the spin correlation at large distance). Once again, the results from the standard algorithm show large fluctuations. The new approach removes the infinite variance problem, manifested for the chosen size runs as a reduction in statistical error bar by a factor of 8.0. The use of this new method has played an integral part in allowing us to obtain accurate results at half-filling for a variety of quantities, and extrapolate reliably to the thermodynamic limit [32].

In Fig. 4.8 a challenging system with stronger interactions ( $U = 8t$ ) is studied. [The system is a  $8 \times 8$  lattice with a twist boundary condition of  $\Theta = (0, \pi)$ . We used  $\beta = 20$  and  $\Delta\tau = 0.01$ .] Results from the standard algorithm are shown for two runs with different random number seeds, but otherwise identical parameters. Drastic discrepancies are seen between them, with run 1 giving a statistical error estimate which is roughly 50 times that of run 2. This behavior makes it difficult to determine the correlation functions with predictive calculations. The new algorithm eliminates this problem, giving consistent and reliable error estimates. The statistical error is smaller than the smallest from the standard calculation. More importantly, the robust behavior allows the calculation to determine the long-range antiferromagnetic order without ambiguity.

## 4.4 Discussion

The symptoms of the infinite variance problem discussed here tend to be subtle. We have observed that the calculation often give “reasonable” results, i.e., the computed ex-

pectation value is often in agreement with the correct answer within (one or two of) the estimated statistical error bar. Different forms of HS transformations can show different levels of severity, as we further discuss below. Even within the same algorithm, different observables can behave differently. Further, the same observables can exhibit erratic behaviors in larger runs (more samples, smaller time steps, longer imaginary-time lengths) which may have been masked in smaller ones. Perhaps the most common symptoms are occasional “spikes” among the MC measurements of an observable, as illustrated earlier. The behaviors seem consistent with a logarithmic divergence of the variance. If not controlled, the problem is likely to manifest itself more strongly with growing computing power. More importantly, the presence of an infinite variance means that, in a strict mathematical sense, the results of all such simulations are affected. Without detailed analysis or comparisons with properly controlled simulations, one could not detect or predict which results may be biased or incorrect.

Different HS transformations, which result in different forms of  $\hat{B}$  in Eq. (2.5), can lead to different behaviors of the determinantal QMC algorithm. For example, in the half-filled repulsive Hubbard model, both the charge (resulting in  $\hat{B}(x) \propto \exp[i\gamma x(n_{i\uparrow} + n_{i\downarrow})]$  with  $\gamma$  a real constant determined by  $\Delta\tau$  and  $U$ ) and spin (resulting in  $\hat{B}(x) \propto \exp[\gamma x(n_{i\uparrow} - n_{i\downarrow})]$ ) decompositions are free of the sign problem. Both lead to infinite variance problems but the charge decomposition tends to have more severe symptoms. The reason is that it yields an imaginary form in the exponent, which causes the orbitals in the Slater determinants, upon propagation by  $\hat{B}(x)$ , to acquire complex phases. Although the overall integrand

$f(\mathbf{X})$  remains real and non-negative for any path  $\mathbf{X}$ , the random walks of the Slater determinants take place in the complex plane [29, 14], rather than on the real axis as with the spin decomposition. The “two-dimensional” nature of the random walks then causes the density distribution of paths in the vicinity of  $f(\mathbf{X}) = 0$  to tend to a finite value. This is closely related to the general case where there is no symmetry protection and a phase problem arises, for which a projection is necessary [29, 14]. The finite density near  $f(\mathbf{X}) = 0$  exacerbates the divergence in Eq. (4.1) and results in a more severe infinite variance problem.

We comment that the infinite variance problem discussed here is absent in the constrained path Monte Carlo [15] or the phase-free AFQMC [29, 14] methods, which are closely related to determinantal QMC. In the former approaches, an importance sampling transformation is applied which modifies the propagator, and thereby the PDF which is being sampled. This is analogous to how the DMC [65, 63] approach works in fermion or other systems in which the ground state wave function  $\phi(R)$  contains zeros (nodes). After importance sampling, one samples a distribution  $\psi_T(R)\phi(R)$  which vanishes quadratically where the trial wave function  $\psi_T(R) = 0$ . (However some observables other than the energy can still have infinite variance [66, 60].) The distinction between determinantal QMC and constrained path AFQMC is perhaps most easily seen from the discussion and illustration in Fig. 4.1 of Ref. [58]. When there is no sign problem,  $P_l$  is non-negative, i.e., the region below the horizontal line of  $P_l = 0$  is positive mirroring the region above, due to symmetry protection. In determinantal QMC all paths are sampled, while in constrained

path only the paths that stay exclusively above (or below) are sampled. In constrained path AFQMC, the boundary condition and the importance sampling that imposes it cause the sampled PDF to vanish quadratically at  $P_l = 0$ , hence removing the infinite variance. On the other hand, the answer from constrained path can be biased if one uses a constraint which gives the incorrect  $P_l = 0$ . To remove the bias, one needs to modify the importance function so that the value of  $\langle \psi_T | \phi \rangle$  is “lifted” to be above zero, for example by adding a small constant similar to Eq. (4.4). The solution discussed in this chapter, using  $\langle \psi_T | e^{-\Delta\tau\hat{H}} | \phi \rangle$ , provides a better way to do so.

To compute the intermediate function  $F(\mathbf{X})$  in Eq. (4.11), we use the propagator written in the form  $e^{-\Delta\tau\hat{H}} \doteq e^{-\Delta\tau\hat{K}/2}e^{-\Delta\tau\hat{V}}e^{-\Delta\tau\hat{K}/2}$ . The two kinetic energy terms are first applied directly to  $\langle \phi^l |$  and  $| \phi^r \rangle$ , respectively. With the resulting single determinants, the interaction energy term, which is expanded in  $\Delta\tau$  is computed in the usual way using the Green functions. (A second order expansion gives an error commensurate with the Trotter error from the propagator.) For the  $\hat{H}$ 's studied in the present work, the interactions are local and the second-order terms can be computed without significant increase in computational cost. Further improvements would be valuable for cases with long-range interactions. In principle, the  $\Delta\tau$  in the propagator in  $F$  does not have to have the same value as in the Trotter break-up in the rest of the simulation, although a different value would make the “bridge link” static. For example, one could use a smaller value of  $\Delta\tau$  and place multiple “bridge” links at fixed locations along the path where measurements will take place. We have also tested the approach of evaluating the expectation value by

directly applying Eq. (2.5), sampling the auxiliary-fields to evaluate the integral similar to the mixed estimator in constrained path AFQMC. This can be used to complement the power expansion approach when the overlap  $f(\mathbf{X})$  is very small and a higher order expansion is needed.

We have focused on ground-state calculations in our discussions. The ideas apply to finite-temperature determinantal QMC as well. In the standard grand-canonical algorithm [50, 67], the integrand corresponding to  $f(\mathbf{X})$  takes the form  $\det[I + \prod_l B(x_l)]$ , where  $B$  is the matrix form of the one-body propagator  $\hat{B}$ . The structure of the path integrals and how  $f(\mathbf{X})$  varies with imaginary time resemble closely [58] that of the ground-state projection, as we have invoked in the discussion above involving  $P_l$ . When symmetry protection is present,  $f(\mathbf{X})$  becomes non-negative, however  $f(\mathbf{X}) = 0$  is in general not removed, since its removal would require the creation of a *finite* lower bound to  $f(\mathbf{X})$  for any random choice of the path  $\mathbf{X}$  as the path length  $l$  is increased. We have carried out preliminary tests with the finite-temperature grand canonical algorithm [12], and found behaviors of the variance similar to those described in Sec. 4.1. It is of course straightforward to apply the analysis we have discussed to determine the presence of the infinite variance problem in any codes. The simplest way to generalize the new algorithm to finite-temperature grand-canonical determinantal QMC would be to set the temperature and the chemical potential by  $L$  time slices, and treat the bridge link only as a mathematical entity, although it will be worthwhile to study if other choices might be more efficient, especially near a phase transition.

The infinite variance problem is not limited to sign-problem-free calculations. In cases where the sign problem is present, one chooses to sample  $|f(\mathbf{X})|$  and keep track of the sign in evaluating Eq. (2.23), so that the estimator in Eq. (2.24) is replaced by

$$\langle \hat{O} \rangle \doteq \left\langle \frac{g(\mathbf{X})}{f(\mathbf{X})} s(\mathbf{X}) \right\rangle_{|f|} / \langle s(\mathbf{X}) \rangle_{|f|}, \quad (4.13)$$

where  $s(\mathbf{X}) = f(\mathbf{X})/|f(\mathbf{X})|$ . Because  $f(\mathbf{X}) = 0$  is not excluded in the PDF of  $|f|$ , the infinite variance problem will arise. In practice, the problem is entangled with the sign problem, which causes  $\langle s \rangle$  to approach zero — and thus the statistically error to grow — exponentially as  $\beta$  or the system size is increased. As a result, the diverging variance can be obscured by the large noise from the sign problem, especially for larger  $\beta$  and system sizes. However, for a fixed  $\beta$  and chosen system size, the average sign  $\langle s \rangle$  is *finite*. There is a well defined expectation value for the estimator above, and one would expect the MC error bar to converge as  $1/\sqrt{M}$  with sample size. The infinite variance problem causes a breakdown of this, in the same manner as in a sign-problem-free case. One example where this point is relevant is in determinantal QMC as impurity solvers [68], where the finite-size of the cluster and the finite-temperatures help reduce the sign problem.

There are additional areas where the general ideas discussed in this chapter can be useful. For example, in the presence of a sign problem, released node [49] calculations in DMC or released constraint [69, 36] calculations in AFQMC both require removing the zeros from the “natural” importance function ( $|\langle R|\psi_T \rangle|$  or  $|\langle \psi_T|\phi \rangle|$ ). This is related to the issues described here, and the bridge link approach, namely an importance function with

an extra propagator inserted, can be an effective approach to generate the new importance function. Similarly for the finite-temperature counterpart of DMC, the path-integral MC method in real space [70, 61] and the related world-line algorithm in lattice models. More generally, the infinite variance problem can arise whenever the distribution being sampled,  $f$ , contains zeros where the corresponding  $g$  in denominator does not vanish. The analysis of the problem and the solution presented here will find use in such situations which can occur in a variety of MC calculations, both quantum and classical.

## 4.5 Conclusion

Interacting quantum many-body systems form a central theme in many disciplines in physics, chemistry, and materials science. Because of their complexity and the high dimensionality of the Hilbert space involved, Monte Carlo methods are often an indispensable tool in the study of such systems. A Monte Carlo calculation computes an expectation value which inherently contains a statistical uncertainty. Without a reliable estimate of the statistical error, the expectation value would become meaningless. A divergence in the variance of the underlying many-dimensional integrals prevents the computation of a reliable error bar, even in principle. It is therefore vital to detect and then remedy this problem. This is the focal point of the present work.

The determinantal QMC algorithms discussed in this chapter are widely applied in physics. Determinantal QMC calculations are expected and assumed to provide unbiased results in a variety of otherwise intractable interacting fermion systems, which span mul-

tiple sub-disciplines of physics. These results play a crucial role in our understanding of a variety of fundamental models and concepts. Recognizing that such calculations have an infinite variance problem and remedying it thus have wide-ranging impacts. The solution we have proposed removes the infinite variance problem in determinantal QMC, with simple modifications to the standard algorithms. The general ideas put forth are applicable in even broader contexts.

## CHAPTER 5

# AFQMC in Hartree-Fock-Bogoliubov Space

For many-fermion systems with pairing, the Hartree-Fock-Bogoliubov (HFB) approach [71] has been a key theoretical and computational tool. The approach has seen successful applications in the study of ground and certain excited states in nuclear systems, as well as in condensed matter physics and quantum chemistry. The method captures pairing and deformation correlations, and often provides a good symmetry-breaking picture for weakly interacting systems. Symmetry can also be restored by projection [72, 73] on a HFB vacuum, which further improves the quality of the approximation.

For strongly interacting many-body systems, the HFB approach is not as effective, because of its underlying mean-field approximation. There have been attempts to incorporate many-particle effects [74, 75]. However a correlated HFB approach is still lacking

which is size-consistent and scales in low polynomial computational cost with system size.

In this chapter we describe a QMC method [76] for handling many-fermion Hamiltonians without  $U(1)$  symmetry. The method evaluates the path integral in auxiliary-field space to produce a ground-state wave function (or finite-temperature partition function) by sampling HFB states. It is a generalization of the AFQMC method from the space of Slater determinants (Hartree-Fock states) to that of HFB states. Below we formulate the QMC approach in this framework, and then outline all the ingredients for implementing a computational algorithm. We illustrate the method with two examples. The first is a solution of the Kitaev model by imaginary-time projection. This is a non-interacting problem whose ground state is available exactly, and serves as an excellent toy problem for illustrating the key elements of the method. The second example is the attractive Hubbard model. We study the pairing order in this model by applying an explicit pairing field that breaks particle number symmetry.

We can list all the key ingredients needed in the QMC algorithm:

1. The random walker  $|\psi\rangle$ , when propagated by the operator  $\exp(\hat{O})$  in Eq. (2.4), evolves into another state,  $|\psi'\rangle$ , of the same form.
2. The overlap of two “walker” wave functions,  $\langle\psi'|\psi\rangle$ , needs to be calculated (in low polynomial complexity).
3. The Green’s function given by a quadratic operator  $\hat{C}$  needs to be computed,  $\langle\psi'|\hat{C}|\psi\rangle/\langle\psi'|\psi\rangle$ , again with low polynomial complexity. In addition, correlation functions (quartic operators) need to be computed from these (as in Wick’s theorem with Slater determinants).

4. The walker wave function need to be stable (or stabilized) numerically during long imaginary-time propagation.

With these ingredients, force bias can be computed [14, 77] to allow importance sampling to achieve better efficiency. Symmetry properties can be imposed [69, 56, 78]. A constrained-path [79] or phaseless [29] approximation can be introduced to control the sign problem. A full AFQMC-like computation can then be carried out, following either the Metropolis path-integral procedure (including force bias), or with open-ended random walks and a constraint if there is a sign or phase problem.

## 5.1 HFB Basics

Let us first define a set of  $N$  single particle creation operators,  $c^\dagger = \begin{pmatrix} c_1^\dagger & c_2^\dagger & \dots & c_N^\dagger \end{pmatrix}$ , and annihilation operators,  $c = \begin{pmatrix} c_1 & c_2 & \dots & c_N \end{pmatrix}$ , which satisfy fermion commutation relations. Quasi-particle bases  $\beta^\dagger$  and  $\beta$ , with the same form as  $c^\dagger$  and  $c$ , can be set through a unitary Bogoliubov transformation,

$$\begin{pmatrix} \beta^\dagger & \beta \end{pmatrix} = \begin{pmatrix} c^\dagger & c \end{pmatrix} \begin{pmatrix} \mathbb{U} & \mathbb{V}^* \\ \mathbb{V} & \mathbb{U}^* \end{pmatrix}, \quad (5.1)$$

Here  $\mathbb{U}$  and  $\mathbb{V}$  are  $N \times N$  matrices. For example,  $N = 2N_{\text{basis}}$  for spin-1/2 fermions in a basis of size  $N_{\text{basis}}$ .

The vacuum of quasi particles is an HFB wave function. It can be written in the form

of a *product state*, with annihilation operators  $\beta$  applied to the true vacuum,

$$|\psi_p\rangle = \prod_i^N \beta_i |0\rangle, \quad (5.2)$$

where the quasi-particle operator  $\beta_i$  is the  $(N+i)$ -th element of the vector on the left-hand side in Eq. (5.1). In the case of a fully paired state when  $\mathbb{U}$  is invertible, an HFB state can alternatively be expressed in the form of a *Thouless state*:

$$|\psi_t\rangle = \exp\left(\frac{1}{2}c^\dagger \mathbb{Z}(c^\dagger)^T\right) |0\rangle, \quad (5.3)$$

where  $\mathbb{Z} = (\mathbb{V}\mathbb{U}^{-1})^*$ , and the superscript “ $T$ ” indicates “transpose”.

When both exist, the two forms are connected by a simple relation  $|\psi_p\rangle = \text{pf}(\mathbb{U}^\dagger \mathbb{V}^*) |\psi_t\rangle$ , where ‘pf’ denotes Pfaffian (see below). In Sec. 5.2 we discuss the QMC formalisms based on each of these two forms as random walkers.

## 5.2 Method

In this section, we show how the four ingredients for a QMC simulation can be realized with HFB states. We first discuss product states in Sec. 5.2.1, which are formally a more direct generalization of Slater determinants in AFQMC. This is followed in the next section by the details for Thouless states. When  $\mathbb{U}$  is invertible, Thouless states are faster than product states, since they have a smaller matrix size and an automatic stabilization procedure, as illustrated in Sec. 5.2.2. Some mathematical details are left to the Appendix,

in order to not impede the flow of the discussion.

We write, without loss of generality, the one-body operator

$$\hat{O} = \sum_{ij}^N t_{ij} c_i^\dagger c_j + \sum_{i>j}^N \Delta_{ij} c_i c_j + \sum_{i>j}^N \tilde{\Delta}_{ij} c_i^\dagger c_j^\dagger, \quad (5.4)$$

which does not have to be Hermitian as it results after HS transformation of the interacting Hamiltonian, with  $\Delta^T = -\Delta$  and  $\tilde{\Delta}^T = -\tilde{\Delta}$ .

### 5.2.1 Product State

*Overlap:* In a QMC simulation, we need to calculate the overlap of two HFB wave functions. With importance sampling, typically only the ratio of overlaps are needed, for example,  $\langle \psi_T | \exp(\hat{O}) | \psi_p \rangle / \langle \psi_T | \psi_p \rangle$ , where  $|\psi_T\rangle$  is the trial wave function. Onishi's Theorem provides a simple way to calculate

$$\langle \psi_p | \psi'_p \rangle^2 = \det(\mathbb{U}'^\dagger \mathbb{U} + \mathbb{V}'^\dagger \mathbb{V}) \det(\mathbb{V}'^\dagger \mathbb{V}), \quad (5.5)$$

where  $\mathbb{U}$  and  $\mathbb{V}$  are the components of the unitary transformation matrix of  $|\psi_p\rangle$  as defined earlier, and  $\mathbb{U}'$  and  $\mathbb{V}'$  are those for  $|\psi'_p\rangle$ . This formula can be used to evaluate the normalization of a product state, for example. However, Eq. (5.5) neglects the sign in the overlap. The sign/phase of the overlap is important (at least the relative sign/phase in the ratio above) in order to impose the constraint to control the sign or phase problem

[14]. Robledo worked out the following form [80] which regains the sign of the overlap:

$$\langle \psi_p | \psi'_p \rangle = (-1)^{N(N-1)/2} \text{pf} \begin{pmatrix} \mathbb{V}^T \mathbb{U} & \mathbb{V}^T \mathbb{V}'^* \\ -\mathbb{V}'^\dagger \mathbb{V} & \mathbb{U}'^\dagger \mathbb{V}'^* \end{pmatrix}, \quad (5.6)$$

where the Pfaffian can be computed (see, e.g., library by Bertsch [81]). Note that, when  $\mathbb{U} = 0$ , Eq. (5.6) will reduce to the formula of Slater determinants,  $\det(\mathbb{V}'^\dagger \mathbb{V})$ , as expected.

*Green's Function:* Physical properties are measured through Green's functions in AFQMC. Similar generalization can be made from Slater determinants to HFB product states. Let us set  $\mathbb{Q} = (\mathbb{U}'^\dagger \mathbb{U} + \mathbb{V}'^\dagger \mathbb{V})^T$ . The three types of Green's functions are then given by

$$\begin{aligned} \rho_{ij} &= \frac{\langle \psi_p | c_i^\dagger c_j | \psi'_p \rangle}{\langle \psi_p | \psi'_p \rangle} = (\mathbb{V}'^* \mathbb{Q}^{-1} \mathbb{V}^T)_{ji}, \\ \kappa_{ij} &= \frac{\langle \psi_p | c_i c_j | \psi'_p \rangle}{\langle \psi_p | \psi'_p \rangle} = (\mathbb{V}'^* \mathbb{Q}^{-1} \mathbb{U}^T)_{ji}, \\ \bar{\kappa}_{ij} &= \frac{\langle \psi_p | c_i^\dagger c_j^\dagger | \psi'_p \rangle}{\langle \psi_p | \psi'_p \rangle} = -(\mathbb{U}'^* \mathbb{Q}^{-1} \mathbb{V}^T)_{ij}. \end{aligned} \quad (5.7)$$

Note that, when  $\mathbb{U} = \mathbb{U}' = 0$ , the first line reduces to the Slater determinant result, while the last two lines vanish, as expected.

A generalized Wick's theorem [82, 83] holds, which allows expectation values of two-body operators and correlation functions to be calculated. For example,

$$\frac{\langle \psi_p | c_i^\dagger c_j^\dagger c_k c_l | \psi'_p \rangle}{\langle \psi_p | \psi'_p \rangle} = \rho_{il} \rho_{jk} - \rho_{ik} \rho_{jl} + \bar{\kappa}_{ij} \kappa_{kl}. \quad (5.8)$$

*Propagation:* We need to apply the exponential of a general one-body operator  $\hat{O}$  to a product HFB wavefunction. It can be shown (see Appendix A) that  $\exp(\hat{O})$  can be “exchanged” with a quasi-particle operator  $\beta_i$  in the following manner

$$\exp(\hat{O})\beta_i = \beta'_i \exp(\hat{O}), \quad (5.9)$$

i.e., by modifying  $\beta_i$  to a new form  $\beta'_i$  defined with the matrix multiplication

$$\beta' = \begin{pmatrix} c^\dagger & c \end{pmatrix} \exp \begin{pmatrix} t & \tilde{\Delta} \\ \Delta & -t^T \end{pmatrix} \begin{pmatrix} \mathbb{V}^* \\ \mathbb{U}^* \end{pmatrix}. \quad (5.10)$$

Successive applications of the above yields

$$\exp(\hat{O}) \prod_i \beta_i |0\rangle = \prod_i \beta'_i \exp(\hat{O}) |0\rangle. \quad (5.11)$$

As shown in Eq. (A.11) in the Appendix,  $\exp(\hat{O})|0\rangle$  on the right-hand side in Eq. (5.11) can be written as

$$\exp(\hat{O})|0\rangle \propto \exp\left[\frac{1}{2}c^\dagger \mathbb{Z}_0(c^\dagger)^T\right]|0\rangle, \quad (5.12)$$

which gives quasiparticle states that are either paired or empty. So the right-hand side of Eq. (5.11) is the vacuum of the new quasi-particle operator  $\beta'_i$ , which is equivalent to

$\prod_i \beta'_i |0\rangle$  up to a constant factor:

$$\exp(\hat{O}) \prod_i \beta_i |0\rangle = \alpha \prod_i \beta'_i |0\rangle. \quad (5.13)$$

The normalization  $\alpha$  can be determined by

$$\alpha = \frac{\langle \phi | \exp(\hat{O}) \prod_i \beta_i |0\rangle}{\langle \phi | \prod_i \beta'_i |0\rangle}, \quad (5.14)$$

where  $|\phi\rangle$  can be any state. For example, the calculation is straightforward when  $|\phi\rangle$  is chosen to be the true vacuum or an eigenstate of  $\hat{O}$  (see Appendix A for details). Note that  $\alpha$  is always 1 if there is no pairing operator, since  $\exp(\hat{O})|0\rangle = |0\rangle$ . This covers the case of the propagation of Slater determinants in standard AFQMC. It also includes, for example, the situation where a pairing trial wave function is used, but also to a Hamiltonian with no pairing field and a HS transformation that does not involve pairing decompositions. If pairing is between two spin components, we can choose the *vacuum* to be the true vacuum of one spin component, and “fully occupied” for the other spin component, which will reduce  $\alpha$  to 1.

*Stabilization:* A unitary Bogoliubov transformation imposes fermion commutation relations to the quasi-particle operators, which ensures that the product form of the HFB wave function is well-defined. There are two stabilization conditions

$$\mathbb{U}^\dagger \mathbb{U} + \mathbb{V}^\dagger \mathbb{V} = 1 \quad (5.15)$$

and

$$\mathbb{U}^T \mathbb{V} + \mathbb{V}^T \mathbb{U} = 0. \quad (5.16)$$

During the iterative propagation, the transformation matrices  $\mathbb{U}$  and  $\mathbb{V}$  are updated following Eq. (5.10):

$$\begin{pmatrix} \mathbb{V}'^* \\ \mathbb{U}'^* \end{pmatrix} = \exp \begin{pmatrix} t & \tilde{\Delta} \\ \Delta & -t^T \end{pmatrix} \begin{pmatrix} \mathbb{V}^* \\ \mathbb{U}^* \end{pmatrix}. \quad (5.17)$$

It is easy to show that, if  $\hat{O}$  is Hermitian, and  $\mathbb{U}$  and  $\mathbb{V}$  satisfy the second condition above, Eq. (5.16), then the new matrices  $\mathbb{U}'$  and  $\mathbb{V}'$  will follow the same condition. However, these conditions can be violated if  $\hat{O}$  has a general form, or simply because of numerical instabilities caused by finite precision. This can be restored by forcing skew-symmetry to

$$\mathbb{B} \equiv \mathbb{U}'^T \mathbb{V}', \quad (5.18)$$

after which we modify  $\mathbb{U}'^T$  if  $\mathbb{V}'$  is invertible, or vice versa.

The first condition is similar to the situation with Slater determinants in AFQMC. Single particle states created by the quasi-particle operators must remain orthonormal to each other. The propagation can violate this condition and cause numerical instability. This can be stabilized by, for example, the modified Gram-Schmidt (modGS) procedure,

$$\begin{pmatrix} \mathbb{V}'^* \\ \mathbb{U}'^* \end{pmatrix} = \begin{pmatrix} \tilde{\mathbb{V}}'^* \\ \tilde{\mathbb{U}}'^* \end{pmatrix} \mathbb{R}, \quad (5.19)$$

where  $\mathbb{R}$  is an upper triangular matrix, and  $\det(\mathbb{R})$  represents the overall normalization/weight of the HFB wave function which usually needs to be stored. Similar to the modGS stabilization in AFQMC, the off-diagonal part of  $\mathbb{R}$  represents nonorthogonality in the original quasi-particle basis, which does not affect the HFB wave function, and can thus be discarded.

It is worth noting that we should always force skew-symmetry of  $\mathbb{B}$  before applying the modGS process. This is because changes in  $\mathbb{B}$  will affect orthonormality, while the modGS will not change the skew-symmetry of  $\mathbb{B}$ :

$$\tilde{\mathbb{B}} = \tilde{\mathbb{U}}'^T \tilde{\mathbb{V}}' = \mathbb{R}^{\dagger -1} (\mathbb{U}'^T \mathbb{V}') \mathbb{R}^{*-1}, \quad (5.20)$$

i.e.,  $\tilde{\mathbb{B}}$  has the same skew symmetry as  $\mathbb{B}$ .

### 5.2.2 Thouless State

When a fully paired state is involved which allows the use of a Thouless form, similar formulas can be written down.

*Overlap:* The overlap of two Thouless states is [80]

$$\langle \psi_t | \psi'_t \rangle = (-1)^{N(N+1)/2} \text{pf} \begin{pmatrix} \mathbb{Z}' & -1 \\ 1 & -\mathbb{Z}^* \end{pmatrix}. \quad (5.21)$$

*Green's Function:* With the same definition as in Sec. 5.2.1, the Green's functions should be the same in the Thouless form as in product state form. They can be written

more compactly for Thouless states:

$$\begin{pmatrix} \bar{\kappa} & \rho \\ -\rho^T & \kappa \end{pmatrix} = \begin{pmatrix} 0 & 1 \\ -1 & 0 \end{pmatrix} - \begin{pmatrix} \mathbb{Z}' & 1 \\ 1 & -\mathbb{Z}^* \end{pmatrix}^{-1}. \quad (5.22)$$

The above can be shown using coherent states. The ingredients are similar to those used in the evaluation of overlaps in Ref. [80].

*Propagation:* Let us denote the matrix representation of  $\exp(\hat{O})$  by

$$\exp(\mathbb{O}) = \begin{pmatrix} \mathbb{K} & \mathbb{M} \\ \mathbb{L} & \mathbb{N} \end{pmatrix}. \quad (5.23)$$

The application of  $\exp(\hat{O})$  on the Thouless state  $|\psi_t\rangle$  gives

$$\exp(\hat{O})|\psi_t\rangle \propto \exp(\hat{O}')|0\rangle, \quad (5.24)$$

after the one-body operator  $\hat{O}$  is combined with the pairing operator from  $|\psi_t\rangle$  (see Appendix A). The corresponding matrix representation of the new operator  $\hat{O}'$  is given by

$$\exp(\mathbb{O}') = \begin{pmatrix} \mathbb{K} & \mathbb{K}\mathbb{Z} + \mathbb{M} \\ \mathbb{L} & \mathbb{L}\mathbb{Z} + \mathbb{N} \end{pmatrix}. \quad (5.25)$$

Using the expansion in Eq. (A.11), we have

$$\exp(\hat{O}')|0\rangle \propto \exp\left(\frac{1}{2}c^\dagger \mathbb{Z}' c^\dagger\right)|0\rangle, \quad (5.26)$$

with

$$\mathbb{Z}' = (\mathbb{K}\mathbb{Z} + \mathbb{M})(\mathbb{L}\mathbb{Z} + \mathbb{N})^{-1}. \quad (5.27)$$

The new Thouless wave function after propagation is

$$|\psi'_t\rangle \equiv \exp(\hat{O})|\psi_t\rangle = \alpha \exp\left(\frac{1}{2}c^\dagger \mathbb{Z}' c^\dagger\right)|0\rangle. \quad (5.28)$$

The weight/normalization of the new state can be determined by

$$\alpha = \frac{\langle\phi|\exp(\hat{O})|\psi_t\rangle}{\langle\phi|\psi'_t\rangle}, \quad (5.29)$$

where we can choose, for example,  $|\phi\rangle = |0\rangle$ , and use Eq. (A.11) to expand  $\exp(\hat{O})$  before calculating the overlap (see Appendix A).

*Stabilization:* As we stabilize the product state in Eq. (5.19), we have

$$\mathbb{Z} = (\mathbb{V}\mathbb{U}^{-1})^* = (\widetilde{\mathbb{V}}\widetilde{\mathbb{U}}^{-1})^*, \quad (5.30)$$

so that the matrix  $\mathbb{R}$  cancels when the matrix  $\mathbb{Z}$  is formed, and the Thouless state is unchanged. This suggests that Thouless state is more stable during the propagation.

Numerical instability can contaminate the HFB wave function. Skew symmetry of  $\mathbb{Z}$  should be enforced to help maintain stability. When the Thouless state is ill-defined, e.g.  $\det(\mathbb{U}) = 0$ , imposing skew-symmetry will not remove the instability. In such cases, a product state should be used instead.

## 5.3 Illustrative Results

### 5.3.1 Kitaev Model

We first demonstrate the propagation of HFB wave functions using the Kitaev model, which describes a spinless  $p$ -wave superconductor. The Hamiltonian is

$$\hat{H} = -\mu \sum_{i=1}^{L_1} n_i - \sum_{i=1}^{L_1-1} (t c_i^\dagger c_{i+1} + \Delta c_i c_{i+1} + \text{h.c.}), \quad (5.31)$$

where h.c. denotes Hermitian conjugate,  $\mu$  is chemical potential,  $n_i = c_i^\dagger c_i$  is the number operator, and  $L_1$  is the number of sites in the one-dimensional lattice (open boundary condition). This model can be solved exactly, since there is no two-body interaction. The ground-state solution has a Majorana energy mode at the boundary [84].

Solving this model by imaginary-time projection is the same as treating one (mean-field) path in the path integral of a many-body Hamiltonian whose HS transformation leads to a one-body Hamiltonian of the form in Eq. (5.31). It involves all the key elements in generalizing an AFQMC calculation from Slater determinant to HFB states. The only difference with a real QMC calculation is that there is no auxiliary-field to be sampled

(or put another way, each field can take on a fixed value). The result will therefore be deterministic, with no statistical fluctuation. As discussed in Chapter 2,

$$|\psi(\tau)\rangle = \exp(-\tau\hat{H})|\psi_T\rangle \quad (5.32)$$

gives the ground state wave function when  $\tau$  is sufficiently large. The ground state energy can be calculated by the mixed estimator

$$E^M(\tau) = \frac{\langle\psi_T|\hat{H}|\psi(\tau)\rangle}{\langle\psi_T|\psi(\tau)\rangle}, \quad (5.33)$$

which involves calculating Green's functions. It can also be calculated by the so-called growth estimator

$$E^G(\tau) = -\ln\left[\frac{\langle\psi_T|\exp(-\Delta\tau\hat{H})|\psi(\tau)\rangle}{\langle\psi_T|\psi(\tau)\rangle}\right]\Big/\Delta\tau, \quad (5.34)$$

which is usually less costly computationally, since it only involves calculating overlaps. Observables can be computed as full expectation of  $|\psi(\tau)\rangle$

$$\langle\hat{O}\rangle_\tau = \frac{\langle\psi(\tau)|\hat{O}|\psi(\tau)\rangle}{\langle\psi(\tau)|\psi(\tau)\rangle}. \quad (5.35)$$

As shown in Fig. 5.1, the computed energies from product state and Thouless state are numerically equivalent, and both converge to the exact ground-state result at large  $\tau$ . (We use a subscript “ $p$ ” or “ $t$ ” to indicate results from projection of product state or Thouless state, respectively. For example,  $E_p^M(\tau)$  means the mixed estimator by propagating in the

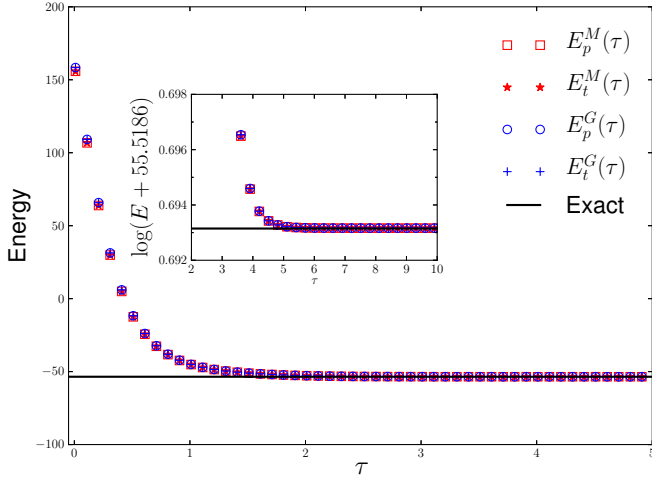


FIG. 5.1: Energy versus imaginary time during projection in the Kitaev model. The lattice size  $L_1$  is 100, and model parameters are  $t = 1.0$ ,  $\Delta = 2.0$ , and  $\mu = -3.2$ . A time step  $\Delta\tau = 0.01$  was used. Results from propagating product states are numerically the same as those from propagating Thouless states. The mixed estimator and the growth estimator are consistent with each other, and converge to the exact answer for sufficiently large  $\tau$ . The inset shows results for  $\tau$  from 2 to 10, with log-scale of the energy.

product state form, while  $E_t^G(\tau)$  means growth estimator by propagating the Thouless state form.) In these tests, we chose a random wave function as the initial and trial wave function  $|\psi_T\rangle$ , which was first set in the product form, and then mapped to the Thouless form. The growth estimator has a small deviation with the mixed estimator at small imaginary times, which results from the Trotter error from the nonzero time step size  $\Delta\tau$ . The deviation vanishes at large  $\tau$  when  $|\psi(\tau)\rangle$  becomes the exact ground state. In Fig. 5.2, we show the computed pairing order at different imaginary times. The initial value at  $\tau = 0.0$  is from the random initial wave function. The result is seen to converge to the exact result at the large  $\tau$  limit.

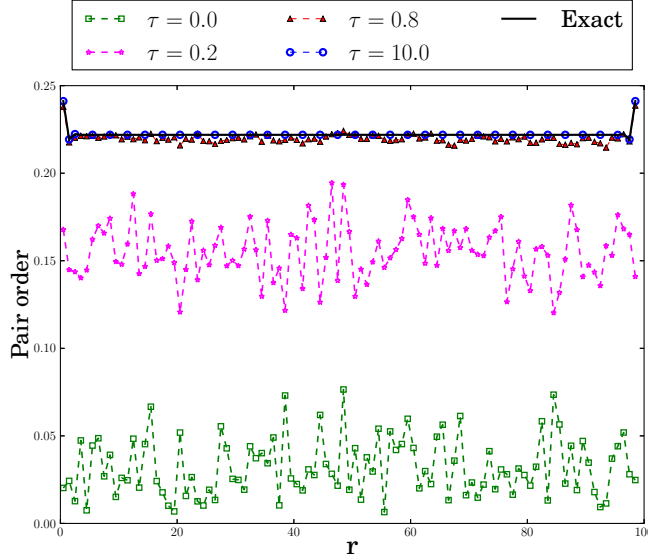


FIG. 5.2: Pairing order  $\langle c_r^\dagger c_{r+1}^\dagger \rangle$  vs. lattice position  $r$  in the Kitaev model computed from  $|\psi(\tau)\rangle$  at different projection-times  $\tau$ , with the same parameters in Fig. 5.1. The order parameter converges to the exact solution at the large imaginary time limit. For clarity, data in the middle of the lattice are shown at every third value of  $r$  for  $\tau = 10$ .

### 5.3.2 Hubbard Model

We next show the propagation of HFB wave functions in an interacting many-fermion system, the two-dimensional Hubbard model. We will consider periodic lattices with  $L_1 \times L_2$  sites in the supercell [i.e.,  $N = 2(L_1 \times L_2)$  in the notation of Eq. (5.4)]. In Eq. (2.1) the sites are labeled by  $i$  and  $j$ , and use chemical potential  $\mu$  to tune number of particles.

In the attractive Hubbard model ( $U < 0$ ),  $s$ -wave electron pairing is present. Our initial state will take a Bardeen-Cooper-Schrieffer (BCS) wave function, which is a special case of the HFB form. This wave function is then propagated in the AFQMC framework [14], and our trial wave function  $|\psi_T\rangle$  is also of the BCS form. In contrast to Slater determinant initial wave functions (such as Hartree-Fock), the number of particles is not

conserved in the BCS wave function. The chemical potential needs to be tuned to reach the targeted number of particles. In Fig. 5.3, we illustrate the convergence of the QMC propagations of the BCS wave function, and how the expectation value of the particle number varies as the chemical potential is varied. (Our calculations are in the  $S_z = 0$  sector, with  $N_\uparrow = N_\downarrow$ .) QMC energies are consistent with exact diagonalization results, as shown in Table 5.1.

The computational cost of the present method scales similarly to Slater determinant random walkers. However, it has a larger prefactor. More specifically, in the current example the computational cost of our method scales as  $N^3$ , while the Slater determinant counterpart scales as  $N^2(N_\uparrow + N_\downarrow)$ . For example,  $N_\uparrow = 2$  in Table 5.1 costs 58 seconds with 48 Xeon E5620 cores. To reach the same accuracy, only 17 seconds is needed for the conventional Slater determinant method.

We also compute the pairing correlation function [77]

$$P_{\text{corr}}(i) = \langle c_{0\uparrow}^\dagger c_{0\downarrow}^\dagger c_{i\downarrow} c_{i\uparrow} \rangle . \quad (5.36)$$

This requires the full estimator which is implemented by back-propagation in the branching random walk approach or by direct measurement at the middle portions of the path in the path integral formula. Here we used the latter [77, 85]. QMC pairing correlation functions are benchmarked against ED results in Fig. 5.4 for different numbers of particles.

The new method affords an advantage in the study of electron pairing correlations, since it allows one to directly treat a Hamiltonian which contains a pairing field. In

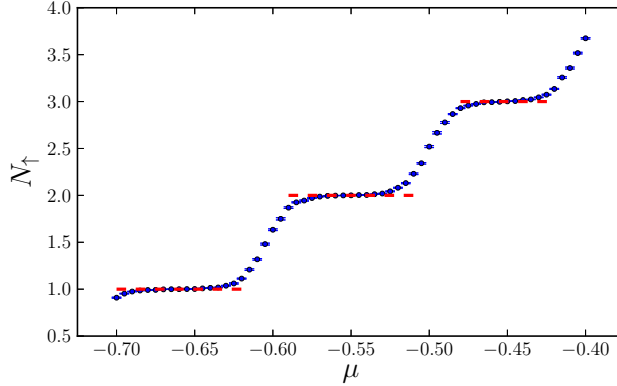


FIG. 5.3: QMC calculations by projecting BCS random walkers. Average particle number (for  $\uparrow$ -electrons) is shown versus chemical potential. The lattice size is  $4 \times 4$ , and model parameters are  $t = 1.0$ ,  $U = -12.0$ . A imaginary-time step of  $\Delta\tau = 0.01$  was chosen, with projection time  $\beta = 64t$ . Our BCS initial wave function has  $\langle N_\uparrow \rangle = 2.0$ . The algorithm converges to different densities as  $\mu$  is varied and gives accurate results. The plateaus indicate integer particle numbers.

standard QMC calculations of the Hubbard model (either attractive as in the present case, or repulsive in which the  $d$ -wave pairing correlation is especially of interest), the Hamiltonian does not break particle number symmetry, which makes it difficult to directly measure a pairing order parameter,  $\langle c_\uparrow^\dagger c_\downarrow^\dagger \rangle$ . Typically one instead measures the pairing correlation function in Eq. (5.36).

TABLE 5.1: Kinetic, interaction, and total energies from QMC and ED. Three QMC calculations from the middle of the plateaus in Fig. 5.3 are shown, with  $\mu = -0.65$ ,  $-0.55$ , and  $-0.45$  respectively, which are compared with ED results for fixed particle numbers. The QMC total energy does not include chemical potential. QMC statistical error bars are on the last digit and shown in parentheses.

$(N_\uparrow, N_\downarrow)$	K		V		E	
	ED	QMC	ED	QMC	ED	QMC
(1, 1)	-2.995	-2.997(3)	-10.42	-10.43(2)	-13.41	-13.42(2)
(2, 2)	-5.318	-5.320(3)	-21.30	-21.33(2)	-26.62	-26.65(2)
(3, 3)	-7.162	-7.167(4)	-32.46	-32.42(3)	-39.62	-39.59(3)

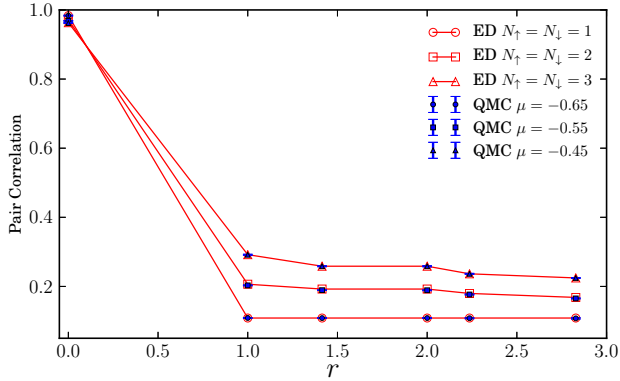


FIG. 5.4: Pairing correlation functions computed from QMC and ED. The chemical potential is tuned in QMC to match particle numbers in the ED calculations. Same run parameters are used as in Fig. 5.3 and Table 5.1. QMC statistical error bars are smaller than symbol size.

If the order parameter is small,  $P_{\text{corr}}(i)$  will be much smaller since it is related to the square of the order parameter at large separation  $i$ . This makes the task of detecting order especially challenging. An alternative way to calculate order parameters is to apply a small pinning field in the Hamiltonian, and detect the order induced by the pinning field [86, 87]. For pairing we could now apply

$$\hat{H}' = \hat{H}_{\text{Hub}} + \sum_i \frac{h_i}{2} (c_{i\uparrow}^\dagger c_{i\downarrow}^\dagger + c_{i\downarrow} c_{i\uparrow}) , \quad (5.37)$$

where the pairing fields  $h_i$  will be non-zero only in a small local region (two neighboring sites in the present case). Using the technique described in this chapter, we can solve the above Hamiltonian for the Hubbard model with a pairing pinning field. Note that, in this special case, the formalism can be reduced to Slater determinants since the pairing field is between spin up and spin down. This was done for up to  $16 \times 16$  lattices to obtain the 1s

pairing order parameter. As illustrated in Fig. 5.3, the use of a pinning field provides a way to measure pairing order with excellent accuracy. (A more detailed study with finite-size scaling will be required to determine the precise value in the thermodynamic limit.)

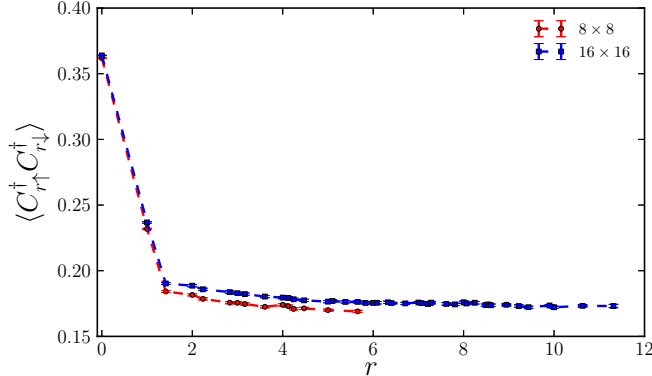


FIG. 5.5: Pairing order versus distance. The lattice sizes are  $8 \times 8$  and  $16 \times 16$ , with total number of particles tuned to 10 and 40, respectively. The model parameters are  $t = 1.0$  and  $U = -8.0$ . We choose a time step  $\Delta\tau = 0.01$ , and projection time  $\beta = 64$ . Pinning field is put on two neighboring sites  $(0,0)$  and  $(1,0)$ , with  $h_i = 1$ .

## 5.4 Discussion and Summary

For clarity, we have separated the two forms of HFB states, the product state and the Thouless state, in the discussion of the technical ingredients. The former is more general, while the latter is restricted to fully paired states but gives more compact representations. Of course they can be mixed and used together as needed, both in theory and in numerical implementation. A limitation is that we have not implemented or discussed the case of unpaired fermions, or when the product in Eq. (5.2) is restricted to a subset of the  $N$  quasi-particle operators. We will leave this to a future study.

In Appendix B, we discuss the special example of propagating singlet-pairing BCS wave functions, and write out explicit formulas for the “mixed” overlap and Green’s functions between a BCS wave function and a Slater determinant. This particular case is useful in the study of Fermi gases, for example, where a charge form of the HS decomposition can be used to decouple the attractive short-range interaction but a BCS trial wave function greatly improves the efficiency [54]. In this form, the energy can be computed straightforwardly with the mixed estimate, but observables require propagating the BCS trial wave function, and keeping it numerically stable.

We have presented the method and formalism in this chapter so that they are invariant to whether the Metropolis or the branching random walk method of sampling is used, or whether a sign problem is present or not. The two examples studied in Sec. 5.3 are sign-problem-free. When there is a sign or phase problem, it is straightforward to apply a constraint to control it approximately. The constraint is imposed in the branching random walk framework of AFQMC, requiring the calculation of the overlap with  $|\psi_T\rangle$ , and the force bias which is given by the mixed Green’s functions. Both of these ingredients have been discussed and can be applied straightforwardly.

In summary, we have presented the computational ingredients to carry out many-body calculations in interacting fermion systems in the presence of pairing fields. All aspects required to set up a full QMC calculations in such systems are described. Components of the formalism presented may also be useful in other theoretical and computational contexts and can be adopted. We illustrated the method in two situations where propagating a

BCS or HFB wave function becomes advantageous or even necessary, namely in model Hamiltonians without  $U(1)$  symmetry, or with standard electronic Hamiltonians when a pairing field term is added to induce superconducting correlations. Related situations include the study of Majorana fermions, or in embedding calculations of standard electronic systems where an impurity is coupled to a bath described by a mean-field solution that may have electron pairing present.

# CHAPTER 6

## Strongly Interacting Fermi Gases in Two Dimensions

### 6.1 Introduction

Exact results on fundamental models are uncommon, especially for strongly interacting fermion systems. In the rare cases where they exist (for example in one-dimensional models by Bethe ansatz or density matrix renormalization group [9, 10]), they have invariably played an integral role in bringing about physical insights, advancing our understanding, and serving as benchmarks for the development of new theoretical and computational approaches.

The Fermi gas with a zero-range attractive interactions is a model for strongly interacting fermions which has generated a great deal of research activities [88, 89]. The model

is of interest in both condensed matter and nuclear physics. As a model it is rather unique in that, thanks to advances in experimental techniques using ultracold atoms, it can be realized in a laboratory with great precision and control [89, 90].

In three-dimensions (3D) the interplay between experiment, theory and computation has lead to rapid advances [91, 92, 54, 93]. An example is seen in the evolution [94] of the determination of the so-called Bertsch parameter at unitarity. Quantitative comparisons have allowed validation of our understanding and provided an impetus for developments of both experimental and theoretical techniques. The remarkable level of agreement achieved recently between calculation [54] and experiment [92] demonstrates the tremendous progress towards precise understanding and control of strongly correlated quantum matter.

The two-dimensional (2D) Fermi gas has attracted considerable recent interest [95, 96, 97, 98, 99, 100, 101, 102, 103], especially with its experimental realization using highly anisotropic trapping potentials [104]. In 2D a bound state always exists, and the BCS-BEC cross-over offers rich possibilities between the interplay of inter-particle spacing (density) and interaction strength, where effects beyond the mean-field description will be more pronounced than in 3D. Interest in this model is further enhanced by the 2D nature of many of the most interesting and complex materials, including high- $T_c$  cuprate superconductors and topological superconductors.

In this chapter, we obtain *exact* numerical results on the ground state of the strongly interacting 2D spin-balanced uniform Fermi gas. Before, the most accurate numerical

results on the 2D system have mainly come from DMC simulations [102]. These calculations, however, involve the fixed-node approximation [105, 65] and lead to systematic errors which are difficult to estimate; furthermore, some of the correlation functions that are central to the physics of these systems are not readily available from DMC. Here, we employ two AFQMC approaches: one based on the branching random walk method used in the 3D study in Ref. [54], and the other a novel approach in the Metropolis path-integral framework which dramatically improves efficiency. Their combination allows us to calculate the thermodynamics and pairing properties exactly in the entire range of interaction strengths.

## 6.2 Model and Method

Our calculations are performed on periodic lattices. We use supercells of up to 3,000 sites, containing about 120 particles, with projection length in imaginary time of  $\beta > 50$  (in units of  $1/E_F$ ). For each lattice and Hamiltonian parameters, the calculation is numerically exact, with only statistical uncertainties which are fully controlled. Systematic extrapolations are then carried out to reach the thermodynamic limit (TL).

As the interaction in cold atoms is short-ranged compared to the inter-particle spacing, the uniform 2D Fermi gas can be modeled by a lattice Hamiltonian

$$\hat{H} = t \sum_{\mathbf{k},\sigma} \varepsilon_{\mathbf{k}} c_{\mathbf{k}\sigma}^\dagger c_{\mathbf{k}\sigma} + U \sum_i n_{i\uparrow} n_{i\downarrow} \quad (6.1)$$

with  $\mathcal{N}_s = L^2$  sites and  $t = \hbar^2/(2m\Delta^2)$ , where  $\Delta$  is the lattice parameter. Only the low energy behavior of  $\varepsilon_{\mathbf{k}}$  will be relevant, and we have used both the Hubbard dispersion  $\varepsilon_{\mathbf{k}}^H = 4 - 2(\cos k_x + \cos k_y)$  and the quadratic dispersion  $\varepsilon_{\mathbf{k}}^q = k_x^2 + k_y^2$ . In this form, the momentum  $k_x$  (or  $k_y$ ) is defined on the lattice, with units  $2\pi/L$ , and  $k_x \in [-\pi, \pi]$ . The on-site interaction is attractive and is given by [106]

$$\frac{U}{t} = -\frac{4\pi}{\ln(k_F a) - \ln(\mathcal{C}\sqrt{n})}, \quad (6.2)$$

which is tuned, for each lattice density  $n \equiv N/\mathcal{N}_s$  and Fermi momentum  $k_F = \sqrt{2\pi n}/\Delta$ , to produce the desired 2D scattering length  $a$ , defined as the position of the node of the zero-energy  $s$ -wave solution of the two-body problem. The constant  $\mathcal{C}$  in Eq. (6.2) depends on the dispersion relation:  $\mathcal{C}^H = 0.49758$  and  $\mathcal{C}^q = 0.80261$ .

We employ two AFQMC methods to study this model: the branching random walk approach, and an accelerated Metropolis approach with a force bias. In the first [54], we project the ground-state wave function by importance-sampled random walks in Slater determinant space [79, 29]. A BCS wave function, taken from the solution of the gap equation for the same discretized Hamiltonian, is chosen as the trial wave function, and the mixed estimator [54, 14] is used to calculate the ground-state energy. The BCS trial wave function shortens the convergence time in the imaginary-time projection, and greatly reduces the Monte Carlo statistical fluctuations, as illustrated in the 3D case [54].

Our second approach is based on the ground-state path integral form of AFQMC, but introduces several advances, including accelerated sampling (described in more detail

in Appendix C) by a dynamic force bias [14], which enables global moves of fields on a time slice with acceptance ratio of over 90%, and control of the Monte Carlo variance [85]. Its main advantage over the the open-ended branching random walk approach is the ease with which any observables can be computed, and we use it to compute the momentum distribution and correlation functions. (Since there is no sign problem here, no constraint is needed, which is the primary motivation for using the open-ended branching random walk form.) With this approach, our calculations typically have  $\beta \sim 320$  or larger (in units of  $t^{-1}$ ), discretized with over 12,800 time-slices.

These technical advances result in orders of magnitude improvement in sampling efficiency, which makes it possible to achieve the high numerical accuracy presented in this work. In both approaches, the computational cost scales as  $\sim \mathcal{N}_s N^2 \beta$ . The linear scaling with  $\mathcal{N}_s$  is important, as it enables calculations on large lattice sizes. To approach the TL, we first extrapolate calculations to the continuum limit by taking  $\mathcal{N}_s \rightarrow \infty$  while holding  $N$  fixed. The number of particles,  $N$ , is then increased until convergence is reached within our statistical accuracy, as illustrated next.

## 6.3 Results

### 6.3.1 Equation of State

Figure 6.1 displays the calculated equation of state (EOS), in units of the Fermi gas energy  $E_{\text{FG}} = \pi n t$ , as a function of the interacting strength,  $x \equiv \ln(k_F a)$ . The top panel

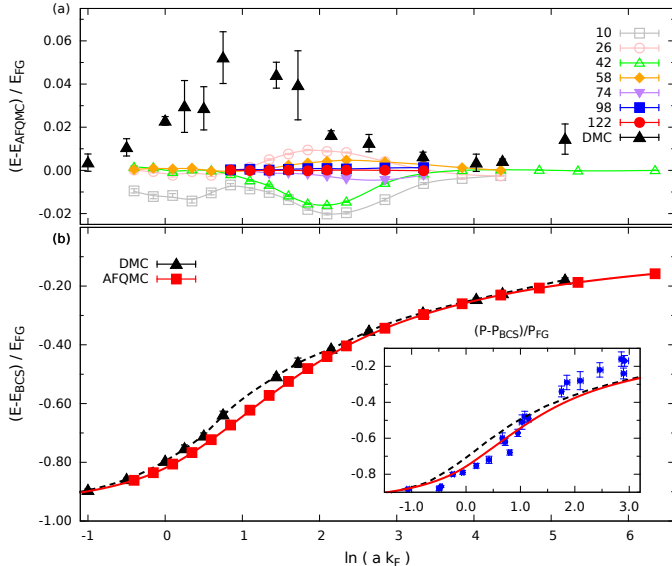


FIG. 6.1: Calculated equation of state. The top panel shows the energy, relative to the final AFQMC results, for finite number of particles,  $N$ . Also shown are the DMC results of Ref. [102], which are variational. Note the small scale of the vertical axis. The bottom panel shows the AFQMC (and DMC) results at the TL, relative to the BCS result. A fit has been performed on the AFQMC results for the EOS. The result is given in Eqs. (6.4-6.5) and shown as the solid line. The inset in panel (b) compares the calculated pressure from AFQMC (solid line) and DMC (dashed, taken from Ref. [102]) with experiment [107] (points) in the crossover region.

illustrates the convergence to the TL, where AFQMC energies are shown for fixed  $N$ . At each  $x$ , the energy has been extrapolated to the continuum limit, using a 4th-order polynomial in  $1/L$ . In the more strongly interacting cases, we take advantage of the fact that  $\varepsilon_{\mathbf{k}}^q$  and  $\varepsilon_{\mathbf{k}}^H$  produce energies which converge to a common limit from opposite directions and perform both sets of calculations to reduce the uncertainty in the extrapolation. In the opposite regime, energies from the quadratic dispersion shows less dependence on  $L$  and they are used alone. We illustrate the extrapolation procedure in Appendix D. The error bar of each symbol, barely noticeable in the graph, combines the QMC statistical error (negligible) at each  $L$  and a conservative estimate of the uncertainty from the extrapolation,

which typically involves half a dozen or more data points from each dispersion relation, with  $L$  ranging from  $\sim 15$  to  $45$  (and larger if necessary).

The results for different values of  $N$  show that convergence is reached to within our statistical accuracy by  $N \sim 100$ . We have applied finite-size corrections to our QMC results using the difference between the BCS energy for the same  $N$  and at the TL. The correction is in general small (largest at large  $x$ ) and vanishes with increasing  $N$ . This is consistent with DMC results [102] which observed no significant change between  $N$  of 26 and 98. The DMC results provide the current best estimate of the EOS and are included in Fig. 1. We see that the error from the fixed-node approximation is largest in the crossover region, at intermediate values of  $x$ . The maximum error is about 10% of the “correlation energy”, the difference between the BCS and exact energies.

In addition to serving as a benchmark for theory, the new EOS can provide validation for experiments. Experiments are fast developing; in 3D remarkable precision [92] was reached in the measurement of the Bertsch parameter (with uncertainties only slightly larger than our symbol size in the top panel of Fig. 6.1). In the inset in the bottom panel, we show a comparison of the calculated pressure with the latest experiment in 2D [107]. In the crossover regime, better agreement with experiment is seen with the new result than with DMC. There may be other factors contributing to the discrepancy between experiment and theory [108, 109]. We leave more detailed comparisons of our results and experiment to a future publication.

We parametrize the computed EOS by  $E_c \equiv E_{\text{QMC}} - E_{\text{BCS}}$  [note that  $E_{\text{BCS}}/E_{\text{FG}}$  is

TABLE 6.1: Final parameter values in the parametrization [Eqs. (6.3-6.5)] of the exact EOS from QMC.

$i$	0	1	2	3	4	5	6	7
$a_i^l$	-11.8041	14.6755	-4.85508					
$a_i$	-0.81984	0.12733	0.06851	-0.01451	-0.00919	0.00419	-0.00064	$3.4312 \times 10^{-5}$
$a_i^r$			-0.06085	0.36401	-0.61531			

related to the two-body binding energy by  $1 - \epsilon_B/(2E_{\text{FG}})$ , and is given by  $1 - 8e^{-2(\gamma+x)}$  where  $\gamma = 0.57721$  is Euler's constant]:

$$\frac{E_c}{E_{\text{FG}}} = \begin{cases} f^l(x), & x \leq 0.2664; \\ f(x), & 0.2664 < x < 4.3058; \\ f^r(x), & x \geq 4.3058. \end{cases}$$

The intermediate region is fitted with a 7th-order polynomial

$$f(x) = \sum_{i=0}^7 a_i x^i. \quad (6.3)$$

In the BCS region, the form is based on perturbative results [110, 111]

$$f^r(x) = -\frac{1}{x} + \sum_{i=2}^4 \frac{a_i^r}{x^i}, \quad (6.4)$$

while in the BEC regime a dimer form is used

$$f^l(x) = -1 + \frac{0.5}{X} \left[ 1 - \frac{\ln(X)}{X} + \frac{c_1}{X} + \frac{\sum_{i=0}^2 a_i^l (\ln X)^i}{X^2} \right], \quad (6.5)$$

where  $X \equiv c_0 - 2x$  with  $c_0 = 3.703$  from the dimer scattering length  $\sim 0.557a$  given

by few-body calculations [95], and  $c_1 = \ln(\pi) + 2\gamma + 0.5$ . The parameters in Eqs. (6.4) and (6.5) are determined by continuity conditions (value and first two derivatives) from Eq. (6.3). The parameters and the locations of the transition between different regions are then varied in a small range to further minimize the variance of the overall fit with the QMC data. The final parameters are listed in Table 6.1. Note that our  $a_2^r$  has different sign from the DMC result [102], but is consistent with analytic results of  $-0.05908$  [110, 111].

### 6.3.2 Contact

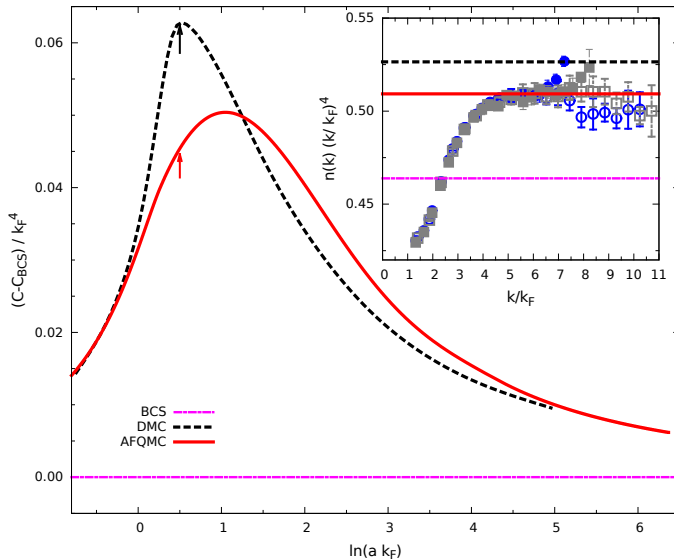


FIG. 6.2: The contact parameter  $C$ . The main figure shows the result of  $C$  (relative to the BCS result) obtained from Eq. (6.6). The statistical uncertainty is smaller than the line thickness. DMC [102] and BCS results are also shown for comparison. The inset shows  $n(\mathbf{k})k^4$  vs  $k \equiv |\mathbf{k}|$  at  $x = 0.5$ . The horizontal lines give the  $C$  values from DMC, AFQMC and BCS (top to bottom), indicated by the arrows in the main figure. The  $n(\mathbf{k})$  data are from two systems, with  $L = 45$  (circles) and  $51$  (squares), respectively, and  $N = 58$ . Results are plotted for  $\mathbf{k}$  along both the horizontal (solid symbols) and diagonal (open) directions.

The contact [112, 113] is important to the physics of dilute gases, and can poten-

tially be measured experimentally [114, 115]. With the functional form of the EOS, it is straightforward to determine the contact:

$$\frac{C}{k_F^4} = \frac{1}{4} \frac{d(E/E_{FG})}{dx}. \quad (6.6)$$

The result is shown in Fig. 6.2. An alternative approach to obtain the contact parameter is from the tail of the momentum distribution [113, 116]:  $n(\mathbf{k})k^4 \rightarrow C$  at large  $k$ . This provides an internal check on the consistency and accuracy of the calculation. As illustrated in the inset, a clear plateau is present before edge effects start to manifest as  $k$  approaches the cut-off value, giving a  $C$  value in excellent agreement with that from the EOS. (The full momentum distribution  $n(\mathbf{k})$  is shown in Fig. 6.3 for three representative interaction strengths.) The pressure and the chemical potential can be obtained from simple combinations of the energy and contact:  $P/P_{FG} = 2C/k_F^4 + E/E_{FG}$ , which was applied in the inset in Fig. 6.1, and  $\mu/\mu_{FG} = C/k_F^4 + E/E_{FG}$ .

### 6.3.3 Pair Wave Function

We next quantify how the pairing properties evolve as a function of interaction strength. The zero-momentum pairing matrix (of dimension  $\mathcal{N}_s \times \mathcal{N}_s$ ),

$$M_{\mathbf{kk}'} = \langle \Delta_{\mathbf{k}}^\dagger \Delta_{\mathbf{k}'} \rangle - \delta_{\mathbf{kk}'} \langle c_{\mathbf{k}\uparrow}^\dagger c_{\mathbf{k}\uparrow} \rangle \langle c_{-\mathbf{k}\downarrow}^\dagger c_{-\mathbf{k}\downarrow} \rangle, \quad (6.7)$$

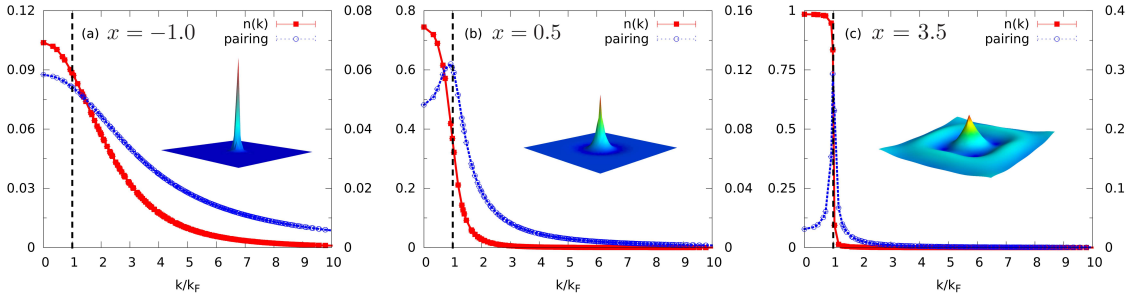


FIG. 6.3: Momentum distribution and pair wave functions in three regimes of interaction strengths,  $x \equiv \ln(ak_F)$ . In each panel, the vertical tick labels on the left are for  $n(\mathbf{k})$  and those on the right are for  $\phi_{\uparrow\downarrow}(\mathbf{k})$ , both plotted vs.  $k$  (in units of  $k_F$ ). Note the different scales between the three panels. The inset shows the real-space wave function  $\psi_{\uparrow\downarrow}(\mathbf{r})$  vs.  $\mathbf{r}$  in a 3D plot. The lattice has  $\mathcal{N}_s = 2025$  sites, with density  $n = 0.0286$ .

is computed in the many-body ground state, where the pair creation operator  $\Delta_{\mathbf{k}}^\dagger \equiv c_{\mathbf{k}\uparrow}^\dagger c_{-\mathbf{k}\downarrow}^\dagger$ . We associate [117] the leading eigenstate with the pair wave function in  $\mathbf{k}$ -space,  $\phi_{\uparrow\downarrow}(\mathbf{k})$ . This is shown in Fig. 6.3 for three characteristic interaction strengths. The inset shows the corresponding real-space structures,  $\psi_{\uparrow\downarrow}(\mathbf{r})$ , obtained from the Fourier transform of  $\phi_{\uparrow\downarrow}(\mathbf{k})$ . In the BEC regime, the momentum distribution is very broad, the pair wave function involves many  $\mathbf{k}$ -values, and the pairs are tightly bound like a molecule, as seen in (a). In the BCS regime in (c), on the other hand, modifications to the non-interacting  $n(\mathbf{k})$  are limited to near the Fermi surface, with a small number of  $\mathbf{k}$ -vectors in its vicinity participating in pairing. The pair wave function is sharply peaked near the Fermi surface, and becomes very extended in real space. (Residual finite-size effect can be seen in this case in the second ring of  $\psi_{\uparrow\downarrow}(\mathbf{r})$  which is affected by the shape of the supercell.) As  $k_F a$  is increased, the systems crosses over from (a) to (c) via the strongly interacting regime represented in (b). Beyond the central peak, the wave function  $\psi_{\uparrow\downarrow}(\mathbf{r})$  in (b) contains significant radial oscillations, with multiple circular nodes.

### 6.3.4 Condensate Fraction

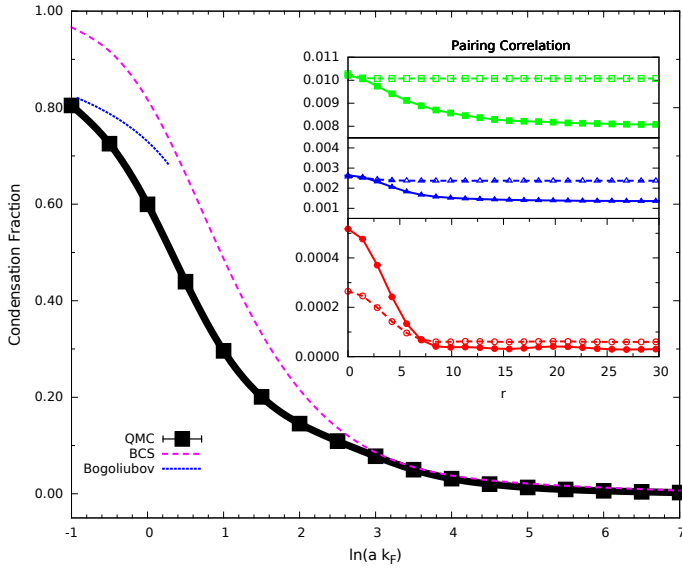


FIG. 6.4: Condensate fraction and pairing correlation functions. In the main graph, the uncertainty in the QMC data (from extrapolation to the TL) is estimated by multiple runs with different sizes and is indicated by the thickness of the line. Also shown are BCS results and, in the BEC limit, Bogoliubov results for Bose gas for reference. In the inset, the pairing correlation function  $C(\mathbf{r})$  is plotted vs.  $r$  for three interaction strengths (from top to bottom, the same parameters as in (a), (b), and (c) of Fig. 6.3). The dashed lines are from BCS and solid lines are QMC results (error bars smaller than symbol size).

The condensate fraction is given by the largest eigenvalue of  $M_{\mathbf{k}\mathbf{k}'}$  divided by  $N/2$ .

The results are shown in Fig. 6.4 as a function of interaction. At the mean-field BCS level  $M_{\mathbf{k}\mathbf{k}'} = \langle \Delta_{\mathbf{k}}^\dagger \rangle \langle \Delta_{\mathbf{k}'} \rangle$ , and there is only one non-zero eigenvalue (equal to  $\sum_{\mathbf{k}} |\langle \Delta_{\mathbf{k}'} \rangle|^2$ ). In the many-body ground state, additional depletion of the condensate is present from scattering into zero-momentum pairs distinct from  $\phi_{\uparrow\downarrow}(\mathbf{k})$ . The BCS condensate fraction and pair wave functions are in reasonable agreement with exact results down to  $\ln(ak_F) \sim -3$ . For stronger interactions, the BCS condensate fraction grows significantly faster. At  $\ln(k_F a) \sim -1$ , it predicts an essentially 100% condensate as opposed to only 80% from

the exact result. In this regime, Bogoliubov theory of a Bose gas [118] with the dimer scattering length above gives results consistent with the QMC data. The largest deviation between BCS and exact results occurs in the crossover region, near  $\ln(ak_F) \sim 0.5$ , where the momentum distributions and pair wave functions also exhibit the largest differences.

We also calculate the real-space on-site pairing correlation function:

$$C(\mathbf{r}) = \langle c_{\mathbf{0}\uparrow}^\dagger c_{\mathbf{0}\downarrow}^\dagger c_{\mathbf{r}\downarrow} c_{\mathbf{r}\uparrow} \rangle, \quad (6.8)$$

where the reference point  $\mathbf{0}$  and all  $\mathbf{r}$  values related by translational symmetry can be averaged over. The results are shown as a function of  $r \equiv |\mathbf{r}|$  in the inset in Fig. 6.4, for three representative values of interaction strength. Long-range order can be seen in all three regimes, with  $C(\mathbf{r})$  approaching a finite constant at large  $r$ .

## 6.4 Summary

In summary, we have calculated *exact* properties of the strongly interacting 2D Fermi gas at zero temperature, by a combination of two AFQMC methods. The equation of state, contact parameter, condensation fraction and pair wave functions are obtained. Improved agreement is seen with the pressure recently measured in quasi-2D experiment compared to best current (approximate) theoretical results. Our results will provide valuable benchmarks for future studies and allow precise comparisons with experiments as the latter rapidly develop in 2D. The analytic forms parametrized from the accurate numeri-

cal results will also facilitate future local-density type of calculations [119] in a variety of systems relevant to experiment, including thermodynamics and out of equilibrium properties in the presence of a trap. The technical advances in computational techniques, which allowed efficient sampling of larger lattices with long imaginary-times and much smaller Monte Carlo variance than previously possible, can be expected to have many applications in cold atom systems and elsewhere.

# CHAPTER 7

## Two-Dimensional Fermi Gas with Rashba Spin-orbit Coupling

### 7.1 Introduction

Spin-orbit coupling (SOC) plays a fundamental role in a number of physical contexts spanning nuclear, atomic, and condensed matter physics. SOC in two-dimensional (2D) systems is particularly relevant to condensed matter physics, because of connections to the quantum Hall effect, and topological insulators and superconductors, among others. While it can be difficult to isolate and study the effects of SOC in typical condensed matter settings, the advent of synthetic gauge fields in ultracold atomic gases [120, 121, 122, 123] provides unprecedented access to clean, tunable systems in which it is possible to precisely investigate the interplay between interaction and SOC. Current experimental efforts have

primarily achieved a combination of Rashba and Dresselhaus SOC. Recently, pure Rashba SOC was realized using a three laser Raman scheme [124], and a number of proposals exist for dark-state, generalized Raman, and magnetic schemes [125, 126, 127, 128, 129, 130, 131, 132].

These recent experimental advances have thus prompted intense theoretical efforts to study SOC in the 2D Fermi gas, many of which focus on the connection between SOC and the BCS-BEC crossover [133, 134, 135, 136, 137, 138]. However, as is commonly the case in the study of strongly interacting systems, mean-field theory is often the only available tool. To date almost all the theoretical and computational work on the Fermi gas has been done at the mean-field level. It is therefore crucial to understand and quantify the corrections from particle correlations, in order to validate the predictions from mean-field calculations. Establishing precise benchmark results is also of fundamental value in guiding and calibrating experiments and assessing new theoretical and computational methods as they are developed for treating SOC in the presence of strong interactions.

In this work we present the first exact results on the ground state of the 2D Fermi gas with strong attractive interactions and Rashba SOC. We show how SOC effects in many-fermion systems can be treated by AFQMC, formulated as random walks of general Slater determinants consisting of spin-orbitals. The method can be generalized to carry out *ab initio* calculations in real materials which will be important in the investigation of novel phases of matter under the interplay of topological physics and strong electron correlations.

For the unpolarized 2D Fermi gas with SOC, this method allows numerically exact calculations free of the sign problem. Combining it with Monte Carlo algorithmic advances, we are able to simulate large lattice sizes to reach the ground state and the continuum limit, and sufficiently large number of particles to reach the thermodynamic limit. Our results present a precision benchmark for an exotic quantum system which, on the verge of experimental realization, combines topological effects and superconductivity.

## 7.2 Model

The Hamiltonian for the 2D Fermi gas with attractive zero-range interactions and Rashba SOC can be written as a sum of three pieces,

$$\hat{H} = \hat{H}_0 + \hat{H}_{\text{SOC}} + \hat{H}_{\text{int}}, \quad (7.1)$$

which correspond to the kinetic, SOC, and interaction energy. We consider  $N$  particles in a periodic box, represented on a lattice of dimension  $L \times L$ , so that

$$\begin{aligned} \hat{H}_0 &= \sum_{\mathbf{k},\sigma} \varepsilon_{\mathbf{k}} c_{\mathbf{k}\sigma}^\dagger c_{\mathbf{k}\sigma}, \\ \hat{H}_{\text{SOC}} &= \sum_{\mathbf{k}} \lambda (k_y - ik_x) c_{\mathbf{k}\downarrow}^\dagger c_{\mathbf{k}\uparrow} + h.c., \\ \hat{H}_{\text{int}} &= U \sum_{\mathbf{i}} n_{\mathbf{i}\uparrow} n_{\mathbf{i}\downarrow}, \end{aligned} \quad (7.2)$$

where  $c_{\mathbf{k}\sigma}^\dagger$  is the creation operator for a fermion with spin  $\sigma$  and momentum  $\mathbf{k}$ . The number operators on lattice site  $\mathbf{i}$  are  $n_{\mathbf{i}\sigma} = c_{\mathbf{i}\sigma}^\dagger c_{\mathbf{i}\sigma}$ , and the dispersion relation is  $\varepsilon_{\mathbf{k}} = |\mathbf{k}|^2 = (k_x^2 + k_y^2)$ . The Hamiltonian in Eq. (7.1) can be directly mapped to the continuum form (e.g., as in experiments) by an overall energy scale defined by the ground-state energy per particle of the corresponding non-interacting Fermi gas,  $E_{FG}$  (which in the present form is  $\pi n$ , with  $n = N/L^2$  the number density). The interaction strength  $U$  is uniquely defined [106] by  $\log(k_F a)$  where the Fermi wave-vector  $k_F$  measures the inverse of the average inter-particle spacing while  $a$  is the scattering length. It is convenient to introduce two dimensionless parameters:

$$\alpha = \frac{\lambda^2}{E_{FG}}; \quad \beta = \frac{\varepsilon_B}{E_{FG}}, \quad (7.3)$$

to specify the strengths of the SOC and interaction, respectively, where  $\varepsilon_B$  is the two-body binding energy at  $\lambda = 0$  and is directly related to  $k_F a$  [77].

Our calculations treat periodic lattices of over 1200 sites, typically with over 70 fermions. For each set of parameters, the many-body ground state is computed using the AFQMC framework [14, 50, 13], generalized to treat SOC. In AFQMC, one projects out the ground state of  $\hat{H}$  from an initial state  $|\phi^{(0)}\rangle$  by repeated applications of the imaginary-time propagator  $e^{-\tau\hat{H}}$ , which is decoupled into path integrals over independent-particle propagators defined by auxiliary-fields. The path integrals can be evaluated by Monte Carlo, which can be realized as random walks in the space of Slater determinants, starting from  $|\phi^{(0)}\rangle$ . Without SOC, each Slater determinant takes the form of a Hartree-

Fock solution,  $|\phi\rangle = |\phi_\uparrow\rangle \otimes |\phi_\downarrow\rangle$ , where the  $\uparrow$ - and  $\downarrow$ -spin components are  $N_s \times N_\uparrow$  and  $N_s \times N_\downarrow$  matrices, respectively, with  $N_s$  being the basis size ( $= L^2$  here) and  $N_\sigma$  being the number of  $\sigma$ -spin fermions ( $= N/2$  here). With SOC, this must be replaced with the generalized Hartree-Fock form, of a  $2N_s \times N$  matrix. The matrix elements evolve stochastically, being propagated by one-body propagators which sample auxiliary-fields and each of which can be thought of as a  $2N_s \times 2N_s$  matrix.

The Fermi gas Hamiltonian, with  $\lambda = 0$ , is free of the sign problem, because  $|\phi_\uparrow\rangle$  can be made identical to  $|\phi_\downarrow\rangle$  for every random walker, so that the trace or ground-state overlap over each path has the form of the square of a determinant and is thus non-negative. With SOC, it is straightforward to show that time-reversal symmetry is preserved,  $\hat{T}\hat{H}_{\text{SOC}}\hat{T}^{-1} = \hat{H}_{\text{SOC}}$ , as is already the case with  $\hat{H}_0$  and  $\hat{H}_{\text{int}}$ . Thus there is no sign problem [26, 139], with the eigenvalues of the overlap matrix being complex-conjugate pairs and thereby the determinant being non-negative. Our calculations are performed on systems with a closed-shell and lattices with odd  $L$  to preserve k-point symmetry. (Of course the  $\lambda = 0$  Hamiltonian can be viewed as a special case, by thinking of  $|\phi_\uparrow\rangle$  and  $|\phi_\downarrow\rangle$  as two diagonal blocks of the  $2N_s \times N$  supermatrix.) We apply dynamic force biases [77] in sampling the AF paths to achieve high efficiency, and remove the infinite variance problem [85]. All numerical biases or systematic errors in the calculations have been controlled so that they are smaller than our statistical uncertainty. The high-precision results obtained are therefore fully *ab initio* and are exact for each parameter set.

## 7.3 Results

### 7.3.1 Equation of State

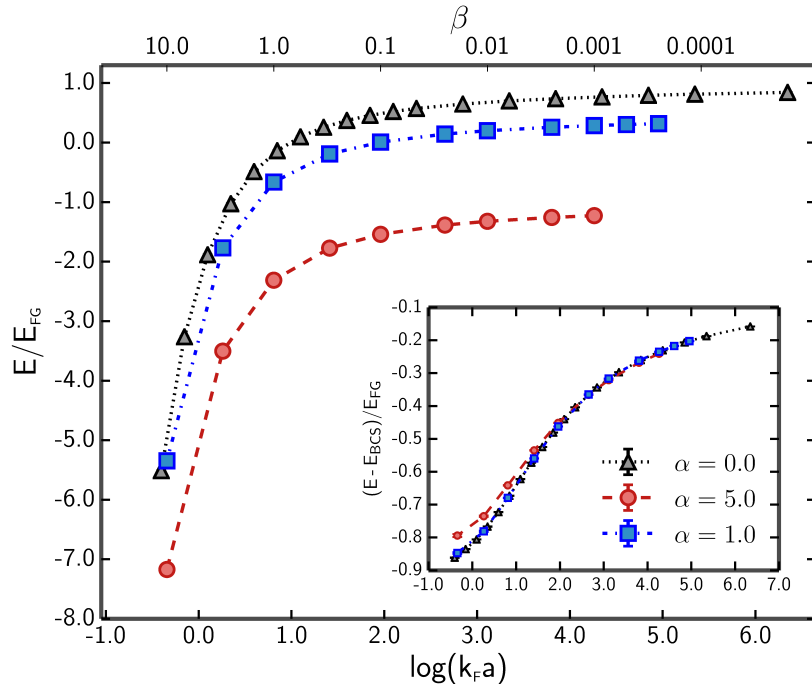


FIG. 7.1: Equation of state for three SOC strengths,  $\alpha = 0.0$  (triangle), 1.0 (square), and 5.0 (circle). Results have been extrapolated to the continuum and thermodynamic limit. The inset plots the results relative to those from BCS, revealing that the correlation energy is quite insensitive to SOC strength.

In Figure 7.1 we present the computed equation of state as a function of interaction strength,  $\log(k_F a)$ , for several values of SOC strength. The results are first extrapolated to the continuum limit with calculations on a sequence of  $L$  values with  $N$  fixed, and then larger  $N$  systems are computed until convergence is obtained [77]. Results for the 2D FG without SOC [77] are also shown as a reference. The most dramatic effect of SOC is a decrease of the total energy, which plateaus at large  $\log(k_F a)$ . The shift to the energy,

which is related to the occupancy of the  $\varepsilon_{\mathbf{k}}^-$  helicity band, becomes more pronounced at larger values of SOC strength. The inset of Fig. 7.1 displays the difference between the QMC energy and the energy predicted by BCS theory. This difference provides a measure of the correlation energy. The similarity in the behavior of the curves suggests that the correlation energy is relatively insensitive to SOC, with a small effect becoming noticeable for systems with strong SOC, in the crossover or BEC regime.

### 7.3.2 Momentum Distributions and Helicity Bands

The non-interacting part of the Hamiltonian can be expressed in diagonal form in the helicity basis with the corresponding dispersion relations,  $\varepsilon_{\mathbf{k}}^{\pm} = \mathbf{k}^2 \pm \lambda|\mathbf{k}|$ . We examine the properties of the many-body ground state in this representation by working in natural orbital space. We diagonalize the one-body density matrix,

$$\begin{pmatrix} \langle n_{\mathbf{k}\uparrow} \rangle & \langle S_{\mathbf{k}}^+ \rangle \\ \langle S_{\mathbf{k}}^- \rangle & \langle n_{\mathbf{k}\downarrow} \rangle \end{pmatrix} = \begin{pmatrix} \langle c_{\mathbf{k}\uparrow}^\dagger c_{\mathbf{k}\uparrow} \rangle & \langle c_{\mathbf{k}\uparrow}^\dagger c_{\mathbf{k}\downarrow} \rangle \\ \langle c_{\mathbf{k}\downarrow}^\dagger c_{\mathbf{k}\uparrow} \rangle & \langle c_{\mathbf{k}\downarrow}^\dagger c_{\mathbf{k}\downarrow} \rangle \end{pmatrix}, \quad (7.4)$$

where the expectation values are taken with respect to the many-body ground state. The eigenvalues yield the momentum distribution in the helicity bands,  $n_{\mathbf{k}}^{\pm}$ . The spin orientation is specified by  $(S^x, S^y)$ , which are computed from  $\langle S_{\mathbf{k}}^{\pm} \rangle$  directly.

Plotted in Fig. 7.2 are the momentum distributions for each helicity band at several values of interaction strength. The insets show the pseudo-spin orientation and magnitude. The helicity bands and the non-interacting Fermi surfaces are indicated for reference.

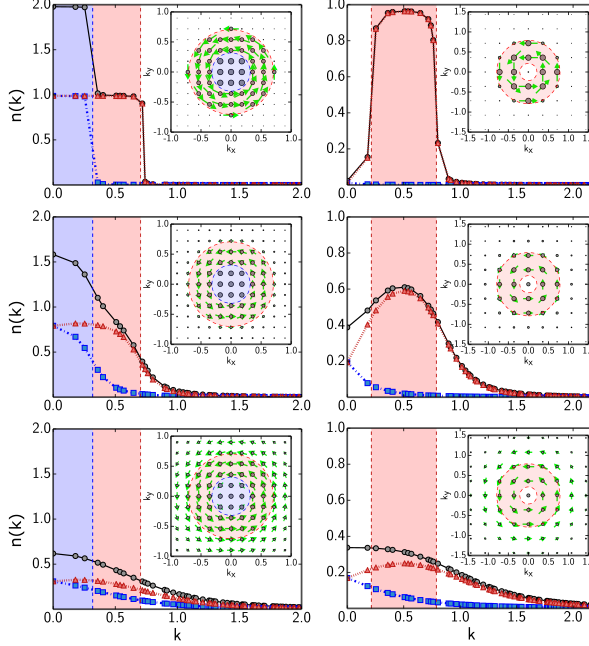


FIG. 7.2: Momentum distributions,  $n_{\mathbf{k}}^+$  (squares),  $n_{\mathbf{k}}^-$  (triangles),  $n_{\mathbf{k}}^{\text{total}}$  (circles) for modest ( $\alpha = 1.0$ , left column) and strong ( $\alpha = 7.0$ , right column) SOC. From top to bottom, the rows correspond to weak ( $\beta = 0.001$ ), intermediate ( $\beta = 1.0$ ), and strong ( $\beta = 10.0$ ) interaction strength. The non-interacting Fermi surfaces are indicated by the vertical dashed lines, and the occupation for each band is indicated by the corresponding shaded regions (in both the main plot and the inset). In the insets, the arrows point to the direction of  $\langle \mathbf{S}_{\mathbf{k}} \rangle$ , and their size indicate its magnitude. The size of the dots represents the magnitude of  $n_{\mathbf{k}}^{\text{total}}$ . These calculations use  $L = 35$  and  $N = 58$  (left column) and  $N = 56$  (right column). (Note that different scales are used between the two columns, and between the last row and the other two to improve clarity.)

(They are also illustrated in more detail in the insets in Fig. 7.3.) In the weak SOC regime, both helicity bands are occupied, while for strong SOC only the  $\varepsilon_{\mathbf{k}}^-$  band is occupied. The transition between the two is at  $\alpha = 4.0$  for  $\beta = 0$ . Our calculations indicate a smooth transition in the presence of interaction.

At small interaction strengths the momentum distributions deviate very little from the non-interacting case, as expected. As  $\beta$  increases, the sharper features of the momentum distributions smoothen and the distributions broaden, indicating that higher momentum

states have become occupied. At intermediate and large interaction strengths the discrepancy from the non-interacting case becomes quite apparent, as interaction dramatically alters the structure defined by the shaded regions. For large SOC, for instance, both bands become occupied and lower  $\mathbf{k}$  states, which are empty in the non-interacting case, are heavily populated.

### 7.3.3 Pair Wave Function

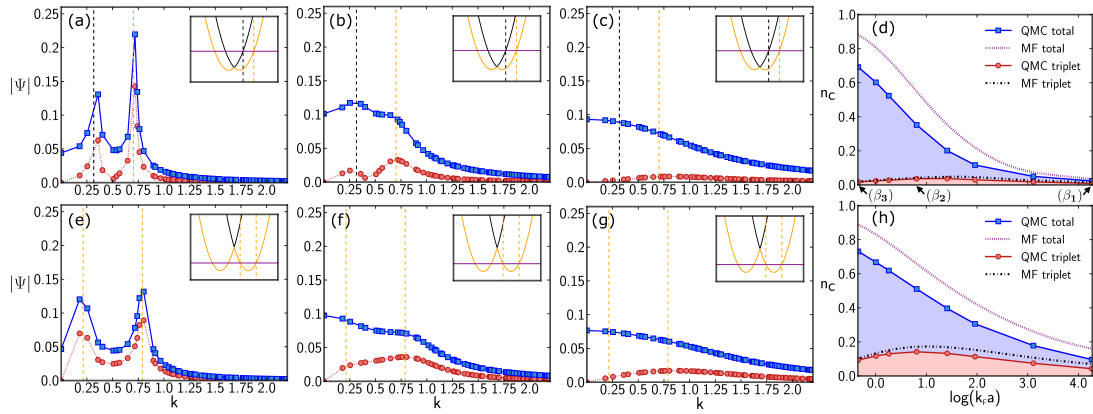


FIG. 7.3: Singlet (square) and triplet (circle) components of the pair wave function, and the condensate fraction. (a)-(d) are for  $\alpha = 1.0$  and (e)-(h) are for  $\alpha = 7.0$ . The first three panels in each row show the wave functions at increasing interaction strength ( $\beta_1 = 0.001$ ,  $\beta_2 = 1.0$ , and  $\beta_3 = 10.0$ , values indicated by arrows in panel (d)). The insets show the helicity bands,  $\varepsilon_{\mathbf{k}}^{\pm}$ , and the non-interacting Fermi surfaces, indicated by the vertical dashed lines. The systems are the same as in Fig. 7.2.

We next examine the pairing properties of the system as a function of SOC and interaction strength. We focus on the interplay of singlet and triplet pairing, and connect the pairing structure to the pair wave function and condensate fraction. With the pairing

operators

$$\begin{aligned}\Delta_{\uparrow}^{\dagger}(\mathbf{k}) &= c_{\mathbf{k}\uparrow}^{\dagger}c_{-\mathbf{k}\uparrow}^{\dagger}; \quad \Delta_{\downarrow}^{\dagger}(\mathbf{k}) = c_{\mathbf{k}\downarrow}^{\dagger}c_{-\mathbf{k}\downarrow}^{\dagger}; \\ \Delta_s^{\dagger}(\mathbf{k}) &= \frac{1}{\sqrt{2}} \left( c_{\mathbf{k}\uparrow}^{\dagger}c_{-\mathbf{k}\downarrow}^{\dagger} - c_{\mathbf{k}\downarrow}^{\dagger}c_{-\mathbf{k}\uparrow}^{\dagger} \right),\end{aligned}\quad (7.5)$$

we construct the following  $3N_s \times 3N_s$  zero-momentum pairing matrix

$$M_{\sigma\sigma'}(\mathbf{k}, \mathbf{k}') = \langle \Delta_{\sigma}^{\dagger}(\mathbf{k}) \Delta_{\sigma'}(\mathbf{k}') \rangle, \quad (7.6)$$

with  $\sigma, \sigma' = \uparrow, \downarrow$ , or  $s$ . The leading eigenvalue,  $N_c$ , of the pairing matrix yields the condensate fraction,  $n_c \equiv N_c/N$ . The corresponding eigenstate gives the pair wave function in  $\mathbf{k}$ -space [117]. The pair wave function is composed of singlet and triplet components,  $|\Psi_c\rangle = |\Psi_{c,s}\rangle + |\Psi_{c,t}\rangle$ . With  $|\Psi_c\rangle$  normalized, we define the singlet and triplet contributions to the condensate fraction by  $n_{c,s}/n_c = \langle \Psi_{c,s} | \Psi_{c,s} \rangle$  and  $n_{c,t}/n_c = \langle \Psi_{c,t} | \Psi_{c,t} \rangle$  respectively.

The singlet and triplet components of the pair wave function, and the condensate fraction, are plotted for several representative values of SOC and interaction strength in Fig. 7.3. The anti-symmetry of the triplet wave function is reflected by the presence of a node at  $\mathbf{k} = 0$ , while the symmetric singlet component has no node.

As SOC strength increases, the amplitude of the triplet component of the wave function becomes closer to that of the singlet, and the triplet portion of the condensate fraction grows relative to the singlet component. The total condensate fraction grows with SOC strength, primarily as a consequence of the increase in triplet pairing, which is induced by

SOC and vanishes as  $\alpha \rightarrow 0$ . BCS theory tends to over-estimate both components but is seen to especially over-estimate the singlet component.

As interaction strength increases the sharp peaks of the wave function, which occur in the vicinity of the Fermi surface, broaden and become smooth. While pairing is confined to the Fermi surface at weak interactions, it occurs over a wide range of momenta at strong interactions, consistent with the modification to the momentum distribution. A peak emerges in the singlet component at low  $|\mathbf{k}|$ , centered around states which are unoccupied in the independent-particle picture. The pairing wave functions in (a) exhibit larger peaks on the right (at larger  $|\mathbf{k}|$ ), in contrast with two relatively even peaks in (e). This is a consequence of the very different properties of the momentum distribution. For  $\alpha = 7.0$ , many unoccupied momentum states are available in the vicinity of the Fermi surface at lower  $|\mathbf{k}|$  to facilitate pairing, which is not the case for  $\alpha = 1.0$ .

The shape and amplitude of the singlet and triplet components of the pair wave function are most similar at small interaction strength, and the contributions to the condensate from singlet and triplet pairs are of roughly equal magnitude. For large interaction strength, the amplitude of the triplet wave function is significantly reduced and the condensate fraction is primarily composed of singlet pairs. The triplet component of the condensate fraction has a peak around  $\log(k_F a) = 1.0$  suggesting that triplet pairing is maximized in the crossover regime, where the strength of the interaction is large enough to induce robust pairing, but not so large as to discourage triplet pair formation.

### 7.3.4 Spin Nematic Order

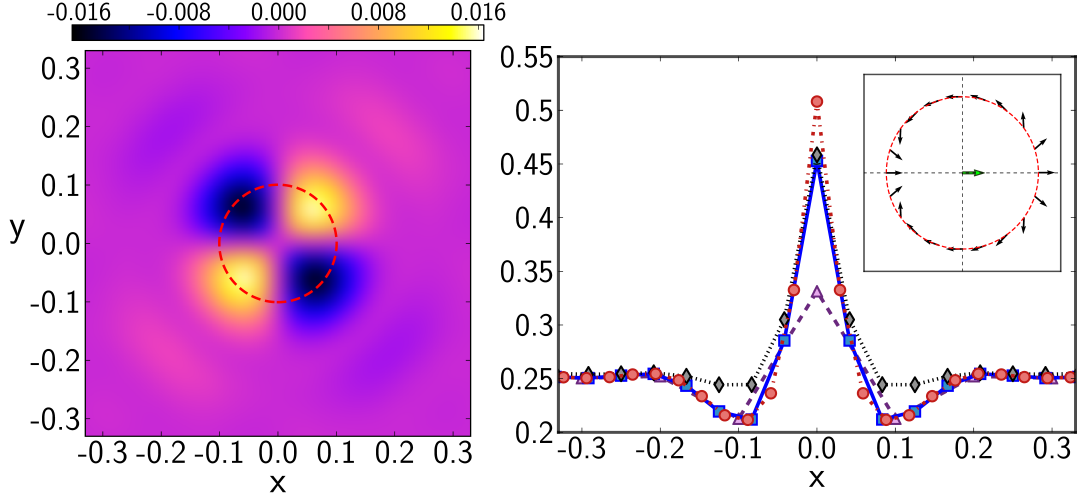


FIG. 7.4: Real-space pairing structure, nematic order, and spin chirality index. Plotted on the left is  $\langle Q^{xy}(0, r) \rangle$  for  $\alpha = 1.0$ ,  $\beta = 0.001$ , with average inter-particle spacing  $1/k_F = 0.0524$ . The right panel shows the (isotropic) spin correlation  $\langle n_{0\uparrow}n_{r\downarrow} \rangle$  for  $L = 11$  (purple triangle),  $25$  (blue square), and  $35$  (red circle). The black diamonds plot a reference curve without SOC for  $L = 25$ . The inset illustrates the chirality of the pair along the dashed red circle shown in the plot of  $Q^{xy}$ .

To probe the real-space structure of pairs and examine possible spin nematic order in the presence of Rashba SOC, we compute the spin correlator defined as [140],

$$\hat{Q}^{ij}(\mathbf{r}_1, \mathbf{r}_2) = \frac{1}{2} \left( \hat{S}_1^i \hat{S}_2^j + \hat{S}_1^j \hat{S}_2^i \right) - \frac{\delta^{ij}}{3} \hat{\mathbf{S}}_1 \cdot \hat{\mathbf{S}}_2, \quad (7.7)$$

where the subscript refers to  $\mathbf{r}_1$  or  $\mathbf{r}_2$  and  $i$  and  $j$  denote  $x$ ,  $y$ , and  $z$ . As depicted in Fig. 7.4,  $\langle Q^{xy} \rangle$  (and similarly,  $\langle Q^{xx} \rangle$ ) yields a flower-shaped pattern, a  $4\pi$  rotation of the second spin in the pair, relative to the first spin, along a circular path around the origin. This spin rotation is illustrated in the upper right panel of Fig. 7.4, which gives the direction of the spin along the dashed red circle in the plot of  $\langle Q^{xy} \rangle$ . Similar chirality/winding behaviors

have been observed in pseudo-spins in layered materials [141, 142, 143, 144]. SOC causes a dramatic difference in the spin correlation as shown in the right panel. With SOC turned on, a significant decrease in  $\langle n_{0\uparrow}n_{r\downarrow} \rangle$  is seen immediately beyond the central peak. However the total density-density correlation (not shown) is essentially unchanged. This signals a decrease in singlet pairing which is compensated for by an increase in triplet pairing.

## 7.4 Summary

In summary, we have developed an approach for exact numerical computations of the ground state of the strongly interacting Fermi gas under SOC, and have provided the first systematic results beyond mean-field theory. A detailed equation of state is obtained. The correlation energy is seen to be nearly independent of SOC strength. Dramatic deviations are seen from the non-interacting picture in the momentum distribution. The condensate fraction is computed. Triplet pairing appears under SOC, and the interplay between interaction and SOC causes triplet pairing to be maximized in the crossover region. Nematic correlation develops but no long-range order is seen. A spin chirality of  $4\pi$  is seen in the pair state. These *ab initio* precision many-body results provide benchmark for theory and can serve as a calibration for experiments.

# CHAPTER 8

## Ground State Properties of the Two-dimensional Hubbard Model

### 8.1 Introduction

The two-dimensional (2D) Hubbard model [33] is one of the simplest models relevant to many correlated electron phenomena, including interaction-driven metal-insulator transitions [145], spin and charge density waves [146], magnetism [59] and high temperature superconductivity[147]. The ability to predict the properties of the 2D Hubbard model is crucial to our understanding of the related exotic quantum states and the transition between them. Though the one dimensional Hubbard model is exactly solvable [148], no exact solution for the Hubbard model exists in two or higher dimensions except for a few special parameter values.

The ground state property of the 2D Hubbard model has been investigated by a variety of methods which have both strengths and weaknesses in different regions of the parameter space. Recently [32, 149], the 2D Hubbard model was studied by state-of-the-art numerical methods [150, 151, 152, 153, 9, 154, 155, 156, 157] including our AFQMC method. In the collaboration, we provide benchmarks for other numerical methods at half-filling, and highly accurate results alway from half-filling. Combined with other methods, we conclude the order in the underdoped region of the two-dimensional Hubbard model.

In this chapter, we present results [158, 48, 149] of the two-dimensional Hubbard model studied by AFQMC method. At half-filling in the repulsive Hubbard model, the result from AFQMC is numerically exact, and the method is computationally very efficient. Away from half-filling, AFQMC methods suffer from the minus sign problem associated with Fermi statistics which leads to exponentially growing statistical errors with system size and inverse temperature. We employ the constrained path formalism under AFQMC, to control the sign problem by introducing a trial wave-function to guide the walk in the Slater determinant space. This restores the algebraic computational scaling as in the half-filled case, but introduces a possible systematic error. We have also used the self-consistent algorithm [48] to minimize this error, and our results are robust as compared with other numerical methods.

## 8.2 Results at Half Filling

In this section, we present results at half-filling. As mentioned, the AFQMC results are numerically exact, as the sign problem is absent because of the particle-hole symmetry. We use a combination of the path-integral approach [77] and the random walk approach [14]. With the former, an infinite variance problem exists which make the Monte Carlo error bars unreliable and thus could render results from standard AFQMC calculations incorrect [85]. The infinite variance problem was removed [85] in our calculations, to obtain reliable results and error estimates on the observables. Results are presented for the ground state energy, double occupancy, effective hopping, and staggered magnetization for  $U = 2, 4, 6$ , and  $8$ . Detailed finite-size data are given, up to  $16 \times 16$ , to provide benchmarks for future theoretical and computational studies. Careful extrapolation and analysis are then performed to obtain results at the thermodynamic limit from the finite-size data.

### 8.2.1 Energy, Double Occupancy, and Effective Hopping

We consider three types of boundary conditions here, i.e. PBC, PBC-APBC, and TABC. Here PBC means periodic along  $x$  and  $y$  direction, PBC-APBC means periodic along the  $x$  direction and anti-periodic along the  $y$  direction, and TABC means twisted average boundary conditions. In Fig. 8.1, we plot the ground state energies versus supercell size for all three boundary conditions. As seen in the table there, our PBC and PBC-APBC data typically range from  $4 \times 4$  to  $16 \times 16$ . Our TABC data contain about 200 twists for the smaller supercells to about 6 twists for  $20 \times 20$ . The statistical error bars contain joint

QMC and twist uncertainties. The fits to reach the TL are also shown in Fig. 8.1, with the insets displaying the asymptotic regime with the TABC, from which the TL values are obtained.

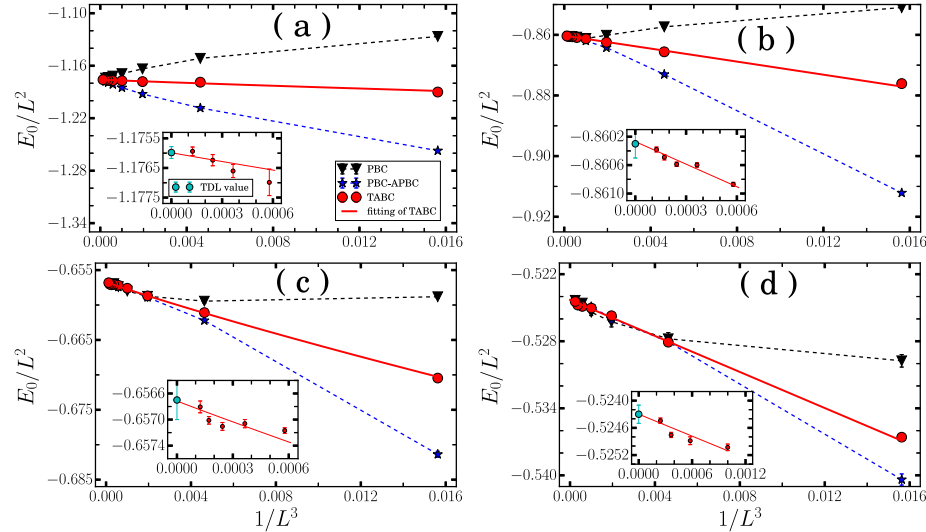


FIG. 8.1: Ground state energy at half-filling calculated using different boundary conditions. PBC, PBC-APBC and TABC data are represented by black triangular, blue star and red dot, respectively. A fit of the TABC data is also shown, with solid red line. Panels (a), (b), (c), (d) correspond to results for  $U = 2, 4, 6, 8$ . In the insets of each panel, a zoom of the TABC results and the fit are shown for large supercell sizes. The cyan dot in each inset represents the TL value and combined statistical and twist error bars and the uncertainty from the fit.

Our fit for the ground-state energy has the following form:

$$E_0/L^2 = e_0 + a/L^3 + b/L^4 \quad (8.1)$$

where  $e_0$  is the energy per site at the TL. In the large  $U$  limit at half-filling, the Hubbard model reduces to the spin-1/2 Heisenberg model with coupling constant  $J = 4t^2/U$  [159]. From spin density wave theory, the leading order of finite size correction to the ground

state energy per site for the latter is  $1/L^3$  on a square lattice [160, 161]. This scaling relationship was also confirmed by quantum Monte Carlo calculations [162]. Our scaling choice in Eq. (8.1), based on these considerations, is seen to fit the data in the Hubbard model with excellent accuracy.

From Fig. 8.1 we see that the TABC energies tend to lie between the PBC and PBC-APBC results. With PBC and PBC-APBC, the curves are less smooth. In fact the PBC energies are non-monotonic for  $U = 4$  and  $U = 6$ . To enter the scaling region of Eq. (8.1), large system size is needed, which makes extrapolation to the TL challenging. The finite size effect is reduced with TABC, as expected from our discussion in the previous section. Even at small system sizes, the scaling relationship in Eq. (8.1) holds well, making the fit more robust compared to that using PBC and PBC-APBC data. With a least squares fit of the TABC data, a reliable estimate of the ground state energy in TL is obtained. For  $U = 2, 4, 6$ , and  $8$ , the final ground state energies per site are  $-1.1760(2)$ ,  $-0.8603(2)$ ,  $-0.6567(3)$ , and  $-0.5243(2)$ , respectively. (The ground state energy for  $U = 4$  is consistent with a previous QMC result  $-0.85996(5)$  obtained with a 45 degree tilted supercell [36])

The magnitude of the finite size effect is seen to decrease with  $U$ . (Note the vertical scales are different in the different panels.) This is the result of a balance of one-body and two-body finite-size effects. The one-body effects are especially pronounced at low  $U$  because of shell effects. The two-body finite-size effects are weakened in the Hubbard model because of the very short-range nature of the interaction. That the TABC results fit the ansatz in Eq. (8.1) so well across the entire range of lattice sizes for all interactions

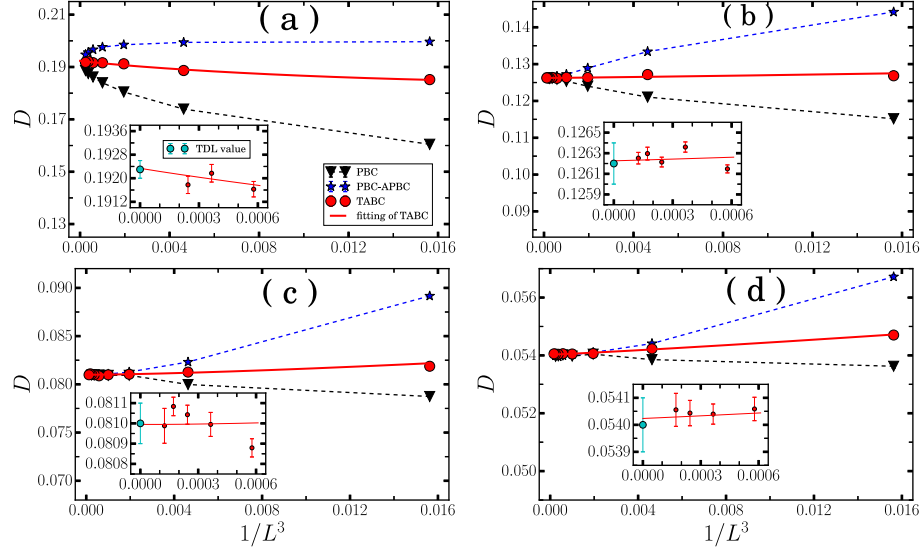


FIG. 8.2: Double occupancy at half-filling calculated using different boundary conditions. Symbols and setup are similar to Fig. 8.1.

is an indication of the separation (or additive nature) of the one- and two-body finite-size effects. The relative improvement of TABC over other boundary conditions is the largest at low  $U$ . At large  $U$ , the effect of the boundary condition is suppressed, and the finite-size effect is dominated by the interaction and the antiferromagnetic correlation. All three boundary conditions give results that fall on the same finite-size curve of Eq. (8.1) for lattice sizes beyond  $L \sim 8$

In Fig. 8.2, we plot the double occupancy,  $D = \langle \sum_i n_{i\uparrow}n_{i\downarrow} \rangle / N$ . Similar to the situation with the ground state energy, the data with TABC lie between the PBC and PBC-APBC data and the finite size effect is reduced by using TABC. We carry out a least squares fit of the TABC data using the scaling relationship given in Eq. (8.1), although the variation with  $L$  is not large compared to the statistical error bars, and the extrapolation is insensitive

to the precise form used here. The TL value obtained by the fits are 0.1923(3), 0.1262(2), 0.0810(1), and 0.0540(1) for  $U = 2, 4, 6$ , and 8, respectively. The double occupancy decreases rapidly with  $U$  as expected.

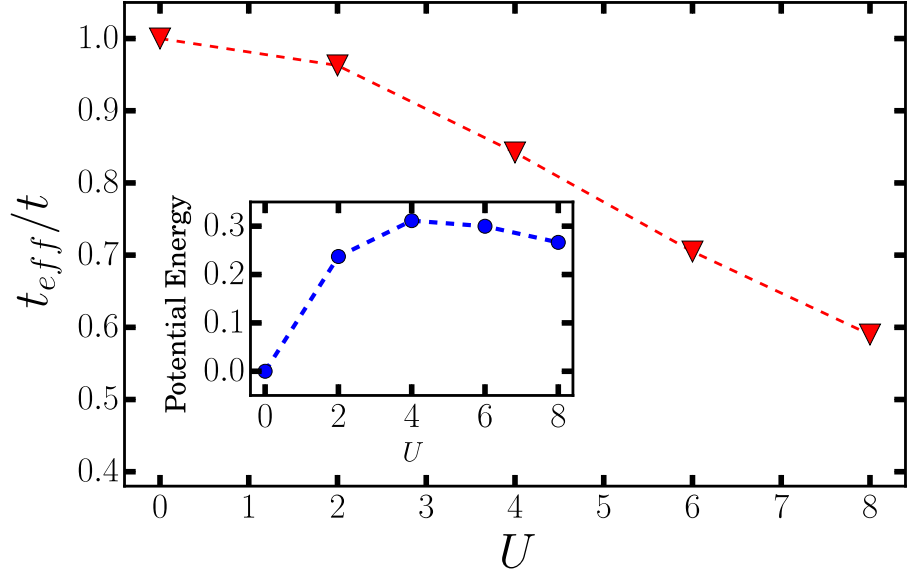


FIG. 8.3: The dependence of the effective hopping,  $t_{\text{eff}}/t$ , on the interaction strength  $U$  at half-filling. The inset shows the corresponding potential energy in units of the non-interacting kinetic energy.

To help quantify the effect of  $U$  on the bandwidth, we calculate the effective hopping  $t_{\text{eff}}/t$  [44], defined as the ratio of kinetic energy in the presence of  $U$  to its non-interacting ( $U = 0$ ) value,

$$\frac{t_{\text{eff}}}{t} = \frac{\langle K \rangle_U}{\langle K \rangle_{U=0}} \quad (8.2)$$

The kinetic energy can be obtained straightforwardly by subtracting the potential energy, given by  $U$  times the double occupancy discussed above, from the total energy. The

effective hopping at the TL is shown in Fig. 8.3 as a function of interaction. The decrease of effective hopping with the increase of  $U$  is consistent with the increasing of locality, as the system develops stronger antiferromagnetic order, which we characterize next.

### 8.2.2 Spin Correlations and Magnetization

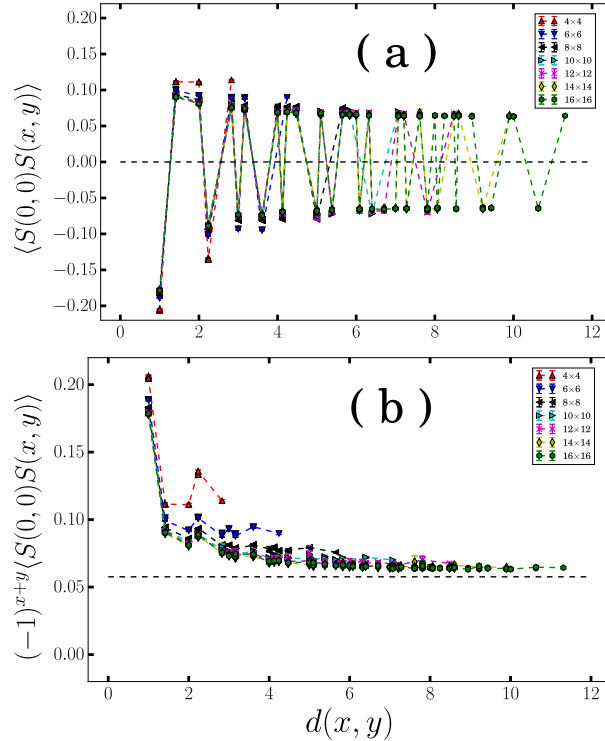


FIG. 8.4: Spin correlation function in the ground state at half filling. System sizes ranging from  $4 \times 4$  to  $16 \times 16$  are shown, under PBC, with  $U = 4$ . The horizontal axis is the relative distance,  $\sqrt{x^2 + y^2}$ . The top panel shows the spin correlation function, while the bottom panel shows the staggered correlation. The dashed horizontal line in (b) shows the final TL value obtained from the fit.

To quantify the magnetic properties in the ground state, we compute the spin correlation function,

$$C(x, y) = \langle \psi_0 | \mathbf{S}(0, 0) \cdot \mathbf{S}(x, y) | \psi_0 \rangle. \quad (8.3)$$

$\mathbf{S}(x, y)$  is the spin operator at site  $i$  with coordinate  $(x, y)$ , which is given by

$$\mathbf{S}(x, y) = \frac{1}{2} \sum_{ss'} c_{is}^\dagger \vec{\sigma} c_{is'}, \quad (8.4)$$

where  $\vec{\sigma}$  denotes the Pauli matrices. In our calculation, translational symmetry is preserved statistically, so the reference point  $(0, 0)$  can be averaged over the whole lattice to reduce the statistical error. In Fig. 8.4, we plot the ground-state spin correlation function for system sizes ranging from  $4 \times 4$  to  $16 \times 16$  under PBC for  $U = 4$ . Long-range order is clearly seen. However, the strength of the correlation decreases substantially from its short-distance values and also as system size is increased, saturating to the asymptotic value very slowly with distance and with system size.

We also compute the staggered magnetization. Two definitions are usually used in the literature [162]. One uses the spin-spin correlation function at the greatest distance which, for a square lattice, is  $M_1^2 = C(L/2, L/2)$ . The other relies on the spin structure factor,

$$M_2^2 = S(\pi, \pi) = \frac{1}{N} \sum_{i=1}^N (-1)^{x_i+y_i} C(x_i, y_i). \quad (8.5)$$

Both definitions have significant finite-size effects, as can be deduced from the results in Fig. 8.4. We use a modified definition [163]

$$M(d)^2 = \frac{1}{N-n} \sum_{x_i^2+y_i^2>d^2}^N (-1)^{x_i+y_i} C(x_i, y_i), \quad (8.6)$$

where  $n$  is the number of sites that fall within a sphere (circle) of radius  $d$  centered at the

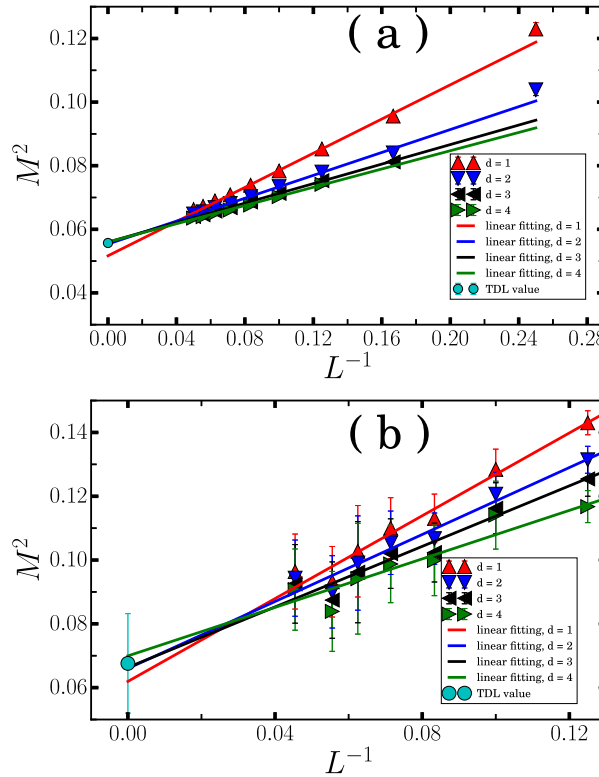


FIG. 8.5: Magnetization computed with TABC at half-filling for (a)  $U = 4$  and (b)  $U = 8$ . For each choice of  $d$ , the result of a fit using the form in Eq. (8.7) is also plotted. The cyan dot represents the final TL value and the estimated error bar.

reference point. All three definitions of the magnetization will converge to the same TL value as  $L \rightarrow \infty$ . However, Eq. (8.6) gives a compromise which removes the large local effects near the reference point while averaging over multiple distances of the long-range correlation to reduce fluctuations.

The computed magnetizations are plotted in Fig. 8.5 for  $U = 4$  and 8. In each case, we show results for a sequence of choices for  $d$ . We fit the computed magnetization as a

function of supercell size, for each choice of  $d$ , with the following scaling form

$$M^2 = M_0^2 + \frac{a}{L} + O\left(\frac{1}{L^2}\right), \quad (8.7)$$

where  $M_0$  is the staggered magnetization at the TL. Similar to scaling forms used above, the form in Eq. (8.7) is motivated by spin-wave theory [164]. The evolution of the fitting with  $d$  is illustrated in the figure. The TL results of magnetizations are 0.094(4), 0.236(1), 0.280(5), and 0.26(3) for  $U = 2, 4, 6$ , and 8, respectively. Our results are consistent with those from a recent finite-temperature determinantal QMC calculation [163]. Note that an upper bound for the magnetization is given by the value of 0.3070(3), from the spin-1/2 Heisenberg model on a square lattice [162]). Our results are consistent with the scenario that the long-range antiferromagnetic(AFM) order persists to small  $U$  values, with no Mott transition at finite  $U$  in the two-dimensional Hubbard model at half-filling.

### 8.3 Results Away from Half-filling

We next study the ground state when the system is doped. The constrained-path approximation is applied to control the sign problem, as mentioned. Previous studies have shown that the systematic error from the constraint in the CPMC calculation is small in the Hubbard model [47]. We carried out additional benchmarks to further quantify the systematic errors [32]. At low and intermediate densities, the CP errors are small, using free electron trial wave functions (TWFs). At higher densities where magnetic correlation

is enhanced, the generalized Hartree-Fock (GHF) trial wave function improves the CP result and brings them to a level roughly comparable to that at intermediate densities. We also use the self-consistent algorithm [48] to minimize this error.

All results reported in this chapter have so far used single-determinant TWFs. Recent progress has resulted in further improvement in the accuracy of CPMC, by use of symmetry properties [69, 56], by constraint release [69]. We have used multideterminant trial wave functions and constraint release to verify the accuracy in a few systems of larger  $L$ . The results are consistent with the benchmark discussed above.

### 8.3.1 Low to Medium Density

In this section, we present numerical results for densities of  $n = 0.3, 0.5, 0.6$ , and  $0.75$  in the TL. We first illustrate the finite-size effects and the extrapolation to the TL with  $n = 0.5$ , which can be precisely realized for any even  $L$ . In Fig. 8.6 (a) and (c), we plot the ground-state energy for  $U = 4$  and  $U = 8$ , using TABC. The corresponding double occupancy is presented in Fig. 8.6 (b) and (d). We have also relaxed the targeted statistical accuracy somewhat compared to half-filling, because of CP systematic errors. Given this and given the large system sizes we compute, the residual finite-size effects are modest. For example, the results from  $16 \times 16$  lattices with TABC are indistinguishable from the extrapolated TL value within statistical errors. Both quantities are seen to continue to fit well the general form in Eq. (8.1), being linear in  $1/L^3$  for large  $L$ . With double occupancy, the TABC reduces the finite-size effects substantially. The residual two-body finite-size

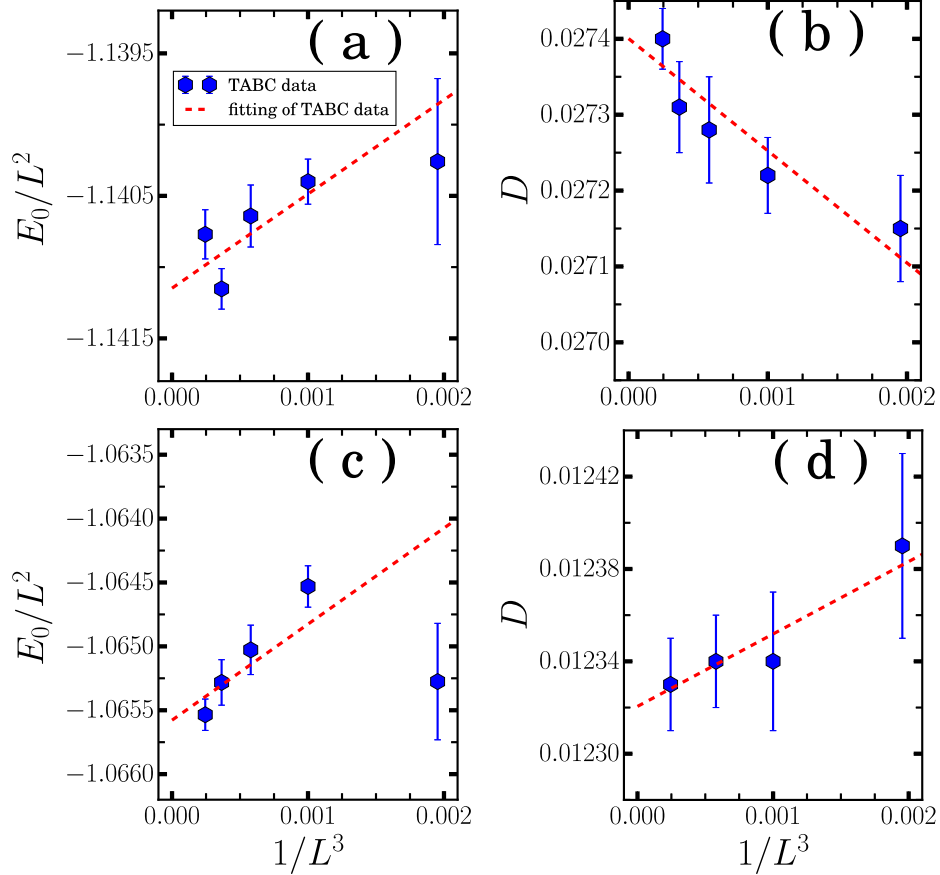


FIG. 8.6: Ground-state energy and double occupancy vs. supercell size at  $n = 0.5$  for  $U = 4$  and  $U = 8$ . TABC is used. Panels (a) and (b) correspond to  $U = 4$ . Panels (c) and (d) correspond to  $U = 8$ . The solid lines are from a fit using  $E_0/L^2(D) \sim e_0(D_0) + a/L^3$ .

effects are seen to have opposite slopes for  $U = 4$  and  $U = 8$ . Similar behavior is seen in the results at half-filling presented in Fig. 8.2.

Similar calculations and analysis were carried out for the other densities. For  $n = 0.3$  and 0.6, integer fillings are not possible in certain finite systems. In these cases, we interpolate from the results for the nearest two integer fillings. A prior study [47] had computed the equation of state for  $U = 4$ . Our results in this density range are consistent with theirs. In Table 8.1 we list the ground-state energies, double occupancies, and kinetic

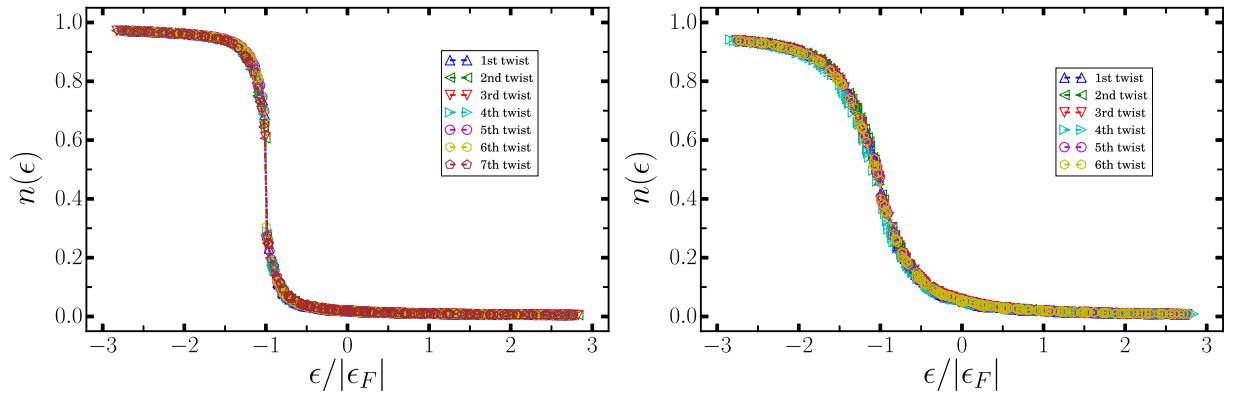


FIG. 8.7: Momentum distribution at  $n = 0.5$  for (a)  $U = 4$  and (b)  $U = 8$ . The horizontal axis is the non-interacting energy for the given momentum normalized by the non-interacting Fermi energy of the corresponding twist.

TABLE 8.1: Ground state energy and kinetic energy per site, and double occupancy for low to intermediate densities at  $U = 4$  and  $U = 8$ .

	$n$	0.3	0.5	0.6	0.75
	$e_0$	-0.8793(2)	-1.141(2)	-1.1845(5)	-1.1491(2)
$U = 4$	$D$	0.00932(1)	0.02740(4)	0.0404(1)	0.06606(6)
	$k$	-0.9166(2)	-1.251(2)	-1.3461(6)	-1.4133(3)
	$e_0$	-0.8534(1)	-1.066(2)	-1.0729(1)	-0.9666(4)
$U = 8$	$D$	0.00442(1)	0.01232(2)	0.01776(3)	0.02847(4)
	$k$	-0.8888(1)	-1.165(2)	-1.2150(3)	-1.1944(5)

energies for all densities studied in this regime for both  $U = 4$  and  $U = 8$ .

We also computed the momentum distribution at  $n = 0.5$  which is shown in Fig. 8.7.

For each  $U$  we plot the results for several twist angles. The  $x$  axis is the non-interacting energy for the given momentum normalized by the non-interacting Fermi energy of the corresponding twist. For  $U = 4$ , we find an obvious discontinuity, which is a indicator of the Fermi liquid behavior in this system and agrees with an early QMC calculation[165].

For  $U = 8$ , there is no obvious jump.

### 8.3.2 $n = 0.875$

The nature of the ground state at  $n = 0.875$  has many competing tendencies, including spin density wave, charge density wave, and possibly superconducting order [166]. In a previous study [167], a spin density wave (SDW) ground state with wavelength  $\lambda = 16$  ( $2/h$ ) was found at  $n = 0.875$  and  $U = 4$ . The computed energies with supercells which are commensurate with the SDW wavelength are seen to be slightly lower than those which are not. Our self-consistent technique [48] gave results consistent with this. As shown in Fig. 8.8, The converged spin and charge density after self-consistent procedure are shown in the upper panel. In the lower panel of Fig. 8.8, the spin density in even and odd rows are plotted to further show the wave-structure.

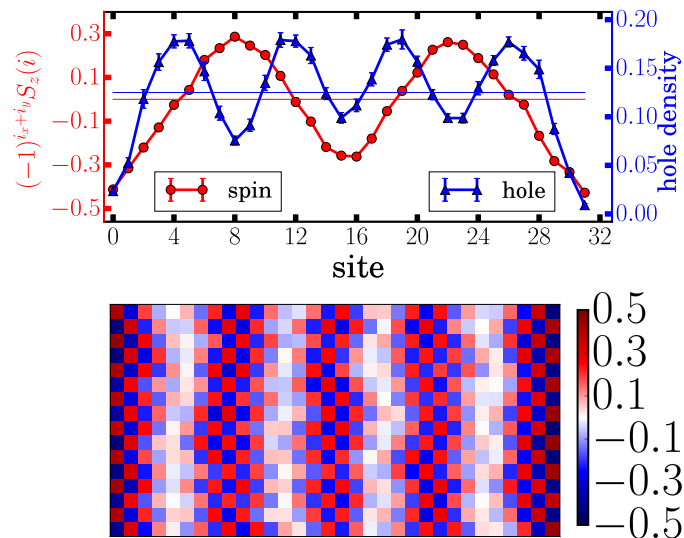


FIG. 8.8: Converged CPMC results after self-consistent procedure. The system has size  $16 \times 32$ ,  $U = 8t$ ,  $h = 1/8$  doping. Opposite pinning fields are applied at the two edges along  $L_y$ . In the upper panel, the staggered spin (hole) densities are plotted in red (blue) color. The red and blue horizontal line represents the zero value for spin and the average hole density, i.e.,  $1/8$  respectively. In the lower pane, the spin density for even and odd rows are plotted.

To accommodate the SDW structure, we studied a range of systems with sizes with length 16, 32, 48, and 64, and width, 4, 6, and 8. To remove the finite-size effects in the computed ground-state energy for the state with wavelength 8, we extrapolated the energies for these systems. In Fig. 8.9 it is seen that the energies are indistinguishable for width, 6 and 8 which means the energy has converged to the targeted statistical accuracy with width 6. We also confirmed the width convergence with length 32 systems. The energies are  $-0.7691(2)$ ,  $-0.7688(2)$ ,  $-0.7691(2)$ , and  $-0.7694(3)$  for width 6, 8, 10, and 12 systems respectively.

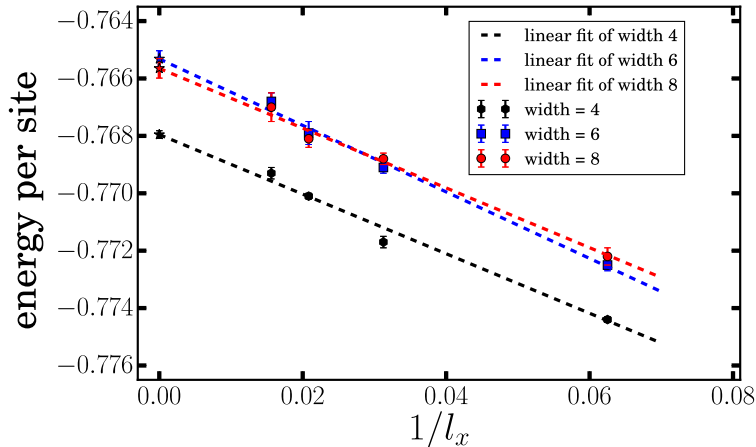


FIG. 8.9: Energies for wavelength 8 state of various lengths and widths for  $U = 8$ . antiferromagnetic pinning fields are applied. Linear fits of  $1/l_x$  are shown. The infinite length values and error bars from extrapolation are marked as stars in the plot.

## 8.4 Conclusion

The Hubbard model is one of the most fundamental models in many-body physics. It is often used as a test ground as new approaches are developed in the quest to reliably treat interacting fermion systems or correlated materials. In this work we have presented

detailed benchmark results for the ground state of the two-dimensional Hubbard model. The total energy, double occupancy, effective hopping, spin correlation function, and magnetization are computed with the AFQMC method.

At half-filling, the results are numerically exact. By a finite size scaling of the TABC data, the most accurate values to date of these quantities are obtained. We also provide the finite size data for system sizes ranging from  $4 \times 4$  to  $16 \times 16$  so as to facilitate benchmark of future analytical and computational studies.

Away from half-filling, we employ the CPMC method, which removes the sign problem and allows us to systematically reach large system size in the same manner as at half-filling. Prior results and a new set of benchmark calculations here show that the systematic error from the constraint is small. Results are presented from low to intermediate densities for  $U/t = 4$  and  $8$ . We also study the case of  $n = 0.875$  with a new self-consistent method and establish that the ground state is a spin density wave.

# CHAPTER 9

## Conclusion and Outlook

We have presented a variety of methodological and algorithmic advances within the AFQMC framework for strongly-correlated many-electron systems. We have shown symmetry properties can be used to greatly increase the accuracy and efficiency in AFQMC calculations, the most commonly employed QMC algorithms in sign problem-free regimes have an infinite variance problem, and an AFQMC method based on path-integrals in the space of Hartree-Fock-Bogoliubov wave functions. These developments represent major steps forward in computational treatment of many-fermion systems. They allow an accurate and size scalable method for fermion systems with strong interactions.

We have shown that symmetry can be rigorously preserved in the AFQMC framework despite the stochastic nature of the calculations. With the Hubbard model as an example, we studied symmetry preservation in two aspects of ground-state AFQMC calculations, the Hubbard-Stratonovich transformation and the form of the trial wave function. It was

shown that significant improvement over state-of-the-art calculations can be achieved. In calculations with constraints, the use of symmetry can reduce the systematic error from the constraint. It also allows more stable release-constraint calculations, leading to essentially exact results in many cases. Thus, the development will allow many applications for fermion systems.

We have shown that the most commonly employed determinantal QMC algorithms have an infinite variance problem. A diverging variance causes the estimated Monte Carlo statistical error bar to be incorrect, which can render the results of the calculation unreliable or meaningless. We discussed how to identify the infinite variance problem. An approach was then proposed to solve the problem. The solution does not require major modifications to standard algorithms, adding a bridge link to the imaginary-time path-integral. The general idea is applicable to a variety of situations where the infinite variance problem may be present. Illustrative results were presented for the ground state of the Hubbard model at half-filling.

We described the computational ingredients for an approach to treat interacting fermion systems in the presence of pairing fields, based on path-integrals in the space of HFB wave functions. The path-integrals can be evaluated by Monte Carlo, via random walks of HFB wave functions whose orbitals evolve stochastically. The approach combines the advantage of HFB theory in paired fermion systems and many-body QMC techniques. The properties of HFB states, written in the form of either product states or Thouless states, were discussed. The states preserve forms when propagated by generalized one-

body operators. They can be stabilized for numerical iteration. Overlaps and one-body Greens functions between two such states can be computed. The method was illustrated with an exact numerical projection in the Kitaev model, and in the Hubbard model with attractive interaction under an external pairing field.

We used our developments to study the two-dimensional strongly interacting, unpolarized, uniform Fermi gas with a zero-range attractive interaction. Two auxiliary-field approaches were employed which accelerate the sampling of imaginary-time paths using BCS trial wave functions and a force bias technique. Their combination enables calculations on large enough lattices to reliably compute ground-state properties in the thermodynamic limit. A new equation of state was obtained, with a parametrization provided, which can serve as a benchmark and allow accurate comparisons with experiments. The pressure, contact parameter, and condensate fraction are determined systematically vs.  $k_F a$ . The momentum distribution, pairing correlation, and the structure of the pair wave function were computed. Our results will provide valuable benchmarks for future studies and allow precise comparisons with experiments as the latter rapidly develop in 2D

We have presented precision ab initio numerical results on the two-dimensional, unpolarized, uniform Fermi gas with attractive interactions and Rashba SOC. Using auxiliary-field quantum Monte Carlo and incorporating recent algorithmic advances, we carried out exact calculations on sufficiently large system sizes to provide accurate results systematically as a function of experimental parameters. We obtained the equation of state, the momentum distributions, the pseudo-spin correlations and the pairing wave functions. Our

results help illuminate the rich pairing structure induced by SOC, and provide benchmarks for theory and guidance to future experimental efforts.

We also studied ground state properties of the Hubbard model on a two-dimensional square lattice. Accurate results for energy, double occupancy, effective hopping, magnetization, and momentum distribution are calculated for interaction strengths of  $U/t$  from 2 to 8. At half-filling, the results are numerically exact and served as a benchmark in the Simons collaboration benchmark project on the Hubbard model. Away from half-filling, the constrained path Monte Carlo method is employed to control the sign problem, and results are obtained with several advances in the computational algorithm. We have provided a definitive resolution of the order in the underdoped ground state and find a stripe order in the underdoped regime.

In the future, we plan to apply the AFQMC method to study high temperature superconductivity, which is one of the major outstanding challenges of theoretical condensed matter physics, for which there is no definitive numerical simulation currently. Based on the experience in the one-band Hubbard model and current study of the three-band Hubbard model, we hope to understand the mechanism for superconductivity induced by electron-electron interaction.

Since most experiments measure spectral functions, and most numerical methods measure static correlation functions, this creates a gap between numerical simulations and experimental measurements. In order to close this gap, we need to measure the dynamic correlation function, which can be used to extract spectral functions. We will do more

research to calculate dynamic correlated function in our AFQMC method [168], in order to extract excited state properties. With these developments, we hope to compare QMC simulations with photoemission spectroscopy results directly.

## APPENDIX A

### HFB Additional Notations and Formulas

We first define a matrix representation which will be used throughout the text. Consider a general bilinear operator,

$$\hat{O} = \sum_{ij}^N t_{ij} c_i^\dagger c_j + \sum_{i>j}^N \Delta_{ij} c_i c_j + \sum_{i>j}^N \tilde{\Delta}_{ij} c_i^\dagger c_j^\dagger + \eta, \quad (\text{A.1})$$

where  $t$ ,  $\Delta$ , and  $\tilde{\Delta}$  are corresponding  $N \times N$  matrices, and  $\eta$  is a constant. Note that  $\hat{O}$  can be non-Hermitian. The matrix representation of  $\exp(\hat{O})$  is

$$\exp(\mathbb{O}) = \exp \begin{pmatrix} t & \tilde{\Delta} \\ \Delta & -t^T \end{pmatrix}, \quad (\text{A.2})$$

which does not depend on  $\eta$ , and we denote its explicit form as

$$\exp(\mathbb{O}) = \begin{pmatrix} \mathbb{K} & \mathbb{M} \\ \mathbb{K} & \mathbb{N} \end{pmatrix}. \quad (\text{A.3})$$

**Linear Transformation of Quas-particle Operators.** An arbitrary quas-particle operator  $\gamma$  has the form

$$\gamma = \begin{pmatrix} c^\dagger & c \end{pmatrix} \begin{pmatrix} v \\ u \end{pmatrix}, \quad (\text{A.4})$$

with  $v = \begin{pmatrix} v_1 & v_2 & \dots & v_N \end{pmatrix}^T$  and  $u = \begin{pmatrix} u_1 & u_2 & \dots & u_N \end{pmatrix}^T$ . It can be proven that

$$\exp(\hat{O})\gamma \exp(-\hat{O}) = \gamma', \quad (\text{A.5})$$

where  $\gamma'$  is built from  $v'$  and  $u'$  with

$$\begin{pmatrix} v' \\ u' \end{pmatrix} = \exp(\mathbb{O}) \begin{pmatrix} v \\ u \end{pmatrix}. \quad (\text{A.6})$$

To prove the above, we use the expansion

$$\exp(\hat{O})\gamma \exp(-\hat{O}) = \gamma + [\hat{O}, \gamma] + \frac{1}{2!}[\hat{O}, [\hat{O}, \gamma]] + \dots \quad (\text{A.7})$$

With commutation relations  $[\hat{O}, c_j^\dagger] = (c^\dagger t)_j + (c\Delta)_j$  and  $[\hat{O}, c_j] = (c^\dagger \tilde{\Delta})_j + (c(-t^T))_j$ , we obtain

$$[\hat{O}, \gamma] = \begin{pmatrix} c^\dagger & c \end{pmatrix} \begin{pmatrix} t & \tilde{\Delta} \\ \Delta & -t^T \end{pmatrix} \begin{pmatrix} v \\ u \end{pmatrix}, \quad (\text{A.8})$$

and

$$[\hat{O}, [\hat{O}, \gamma]] = \begin{pmatrix} c^\dagger & c \end{pmatrix} \begin{pmatrix} t & \tilde{\Delta} \\ \Delta & -t^T \end{pmatrix}^2 \begin{pmatrix} v \\ u \end{pmatrix}. \quad (\text{A.9})$$

The right hand side of Eq. (A.7) thus gives

$$\gamma' = \begin{pmatrix} c^\dagger & c \end{pmatrix} \exp \begin{pmatrix} t & \tilde{\Delta} \\ \Delta & -t^T \end{pmatrix} \begin{pmatrix} v \\ u \end{pmatrix}. \quad (\text{A.10})$$

**Expansion of Exponential Operators.** Following Hara and Iwasaki [169], we can expand  $\exp(\hat{O})$  to three one-body operators,

$$\exp(\hat{O}) = \exp\left(\frac{1}{2}c^\dagger \mathbb{Z} c^{\dagger T}\right) \exp(c^\dagger \mathbb{X} c^T) \exp\left(\frac{1}{2}c \mathbb{Y} c^T\right) \times \langle 0 | \exp(\hat{O}) | 0 \rangle. \quad (\text{A.11})$$

With the help of matrix representation in Eq. (A.3), we have

$$\mathbb{Z} = \mathbb{M} \mathbb{N}^{-1}, \mathbb{X} = \ln(\mathbb{K}), \mathbb{Y} = \mathbb{N}^{-1} \mathbb{L}. \quad (\text{A.12})$$

We can also prove

$$\langle 0 | \exp(\hat{O}) | 0 \rangle = \sqrt{\det(\mathbb{N})} \exp\left[\frac{1}{2} \text{Tr}(t) + \eta\right]. \quad (\text{A.13})$$

**Compression of Exponential Operators.** When we have an operator created by multiplying exponentials of one-body operators

$$\hat{O}_3 = \log[\exp(\hat{O}_1) \exp(\hat{O}_2)], \quad (\text{A.14})$$

$\hat{O}_3$  is still a general one-body operator according to Baker-Campbell-Hausdorff formula.

Its matrix representation is

$$\exp(\mathbb{O}_3) = \exp(\mathbb{O}_1) \exp(\mathbb{O}_2), \quad (\text{A.15})$$

which can be proven by linear transformation relation in Eq. (A.5),

$$\begin{aligned} \gamma'' &= \exp(\hat{O}_3)\gamma \exp(-\hat{O}_3) \\ &= \exp(\hat{O}_1)[\exp(\hat{O}_2)\gamma \exp(-\hat{O}_2)] \exp(-\hat{O}_1), \end{aligned} \quad (\text{A.16})$$

where  $\gamma''$  is built from  $v'', u''$  by

$$\begin{aligned} \begin{pmatrix} v'' \\ u'' \end{pmatrix} &= \exp(\mathbb{O}_1) \exp(\mathbb{O}_2) \begin{pmatrix} v \\ u \end{pmatrix} \\ &= \exp(\mathbb{O}_3) \begin{pmatrix} v \\ u \end{pmatrix}. \end{aligned} \quad (\text{A.17})$$

The matrix relations above define everything up to a proportionality constant. The constant prefactor can be determined from

$$\langle 0 | \exp(\hat{O}_3) | 0 \rangle = \langle 0 | \exp(\hat{O}_1) \exp(\hat{O}_2) | 0 \rangle. \quad (\text{A.18})$$

The right-hand side can be calculated by expanding  $\exp(\hat{O}_1)$  and  $\exp(\hat{O}_2)$  as in Eq. (A.11), which leads to overlap of two Thouless state wave functions.

**Phase of the HFB State After Propagation.** The phase factor of the product state after propagation is determined by Eq. (5.14). If we have  $|\phi\rangle$ , the eigenstate of  $\hat{O}$ :

$$\hat{O}|\phi\rangle = \bar{O}|\phi\rangle, \quad (\text{A.19})$$

it is easy to calculate  $\alpha$ ,

$$\alpha = \exp(\bar{O}) \frac{\langle \phi | \prod_i \beta_i | 0 \rangle}{\langle \phi | \prod_i \beta'_i | 0 \rangle}, \quad (\text{A.20})$$

which only involves two overlaps of HFB wave functions. Alternatively, if we choose  $|\phi\rangle$  to be the true vacuum, we can apply Eq. (A.11) to expand  $\exp(\hat{O})$ :

$$\alpha = \langle 0 | \exp(\hat{O}) | 0 \rangle \frac{\langle 0 | \exp(\frac{1}{2}c\mathbb{Y}c^T) \prod_i \beta_i | 0 \rangle}{\langle 0 | \prod_i \beta'_i | 0 \rangle}. \quad (\text{A.21})$$

Exchanging the exponential operator to the right, we obtain

$$\exp(\frac{1}{2}c\mathbb{Y}c^T) \prod_i \beta_i | 0 \rangle = \prod_i \beta''_i \exp(\frac{1}{2}c\mathbb{Y}c^T) | 0 \rangle \quad (\text{A.22})$$

$$= \prod_i \beta''_i | 0 \rangle, \quad (\text{A.23})$$

so that  $\alpha$  can be determined by the overlaps between the true vacuum and HFB states,

$$\alpha = \langle 0 | \exp(\hat{O}) | 0 \rangle \frac{\langle 0 | \prod_i \beta''_i | 0 \rangle}{\langle 0 | \prod_i \beta'_i | 0 \rangle}. \quad (\text{A.24})$$

The phase in Thouless state is determined by Eq. (5.29). When  $|\phi\rangle$  is chosen to be the true vacuum, we can expand  $\exp(\hat{O})$  as in Eq. (A.7),

$$\alpha = \langle 0 | \exp(\hat{O}) | 0 \rangle \langle 0 | \exp(\frac{1}{2}c\mathbb{Y}c^T) | \psi_t \rangle, \quad (\text{A.25})$$

which is given by the overlap of two Thouless state wave functions.

## APPENDIX B

# The Special Case of an HFB Wave Function and a Slater Determinant

A special case of our discussions is an HFB wave function with a Slater determinant (SD). Here the HFB wave function is

$$|\psi\rangle = \exp\left(\frac{1}{2}c^\dagger Z(c^\dagger)^T\right)|0\rangle, \quad (\text{B.1})$$

and the SD wave function is

$$|\phi\rangle = \prod_i^M \phi_i^\dagger |0\rangle, \quad (\text{B.2})$$

with  $\phi_i^\dagger = c^\dagger \phi_i$ , and  $M$  being the number of fermions.

The overlap between the HFB and SD wave functions is determined by

$$\langle\psi|\phi\rangle = \text{pf}(\phi^T Z^* \phi). \quad (\text{B.3})$$

Setting  $Q = \phi^T \mathbb{Z}^\dagger \phi$ , we have the Green's functions,

$$\begin{aligned}\rho_{ij} &= \frac{\langle \psi | c_i^\dagger c_j | \phi \rangle}{\langle \psi | \phi \rangle} = (\mathbb{Z}^\dagger \phi Q^{-1} \phi^T)_{ji}, \\ \kappa_{ij} &= \frac{\langle \psi | c_i c_j | \phi \rangle}{\langle \psi | \phi \rangle} = (-\phi Q^{-1} \phi^T)_{ij}, \\ \bar{\kappa}_{ij} &= \frac{\langle \psi | c_i^\dagger c_j^\dagger | \phi \rangle}{\langle \psi | \phi \rangle} = (-\mathbb{Z}^\dagger + \mathbb{Z}^\dagger \phi Q^{-1} \phi^T \mathbb{Z}^\dagger)_{ij}.\end{aligned}\quad (\text{B.4})$$

**Projected HFB wave function.** In situations where it is desirable to preserve  $U(1)$  symmetry projected HFB (PHFB) wave function becomes useful. For a fixed number of particles  $M$ , the PHFB wave function is

$$|\psi_{\text{PHFB}}\rangle = \frac{1}{2^{M/2}(M/2)!} (c^\dagger Z c^\dagger)^{M/2} |0\rangle. \quad (\text{B.5})$$

The overlap between a PHFB and an SD is the same as Eq. (B.3) and the Green's functions are the same as Eq. (B.4).

The propagator for PHFB should not break  $U(1)$  symmetry. Let us set  $\Delta$  and  $\tilde{\Delta}$  to zero in Eq. (A.1). The new PHFB wave function after propagation is

$$|\psi'_{\text{PHFB}}\rangle = \exp(\hat{O}) |\psi_{\text{PHFB}}\rangle, \quad (\text{B.6})$$

and  $Z'$  in  $|\psi'_{\text{PHFB}}\rangle$  is

$$Z' = \exp(t) Z \exp(t^T). \quad (\text{B.7})$$

**Spin-1/2 model with singlet pairing.** Let us consider spin-1/2 fermions in a basis of

size  $N_{\text{basis}}$ . If pairing is only between opposite spins,  $\mathbb{Z}$  is specialized to

$$\mathbb{Z} = \begin{pmatrix} 0 & \mathbb{Z}_0 \\ -\mathbb{Z}_0^T & 0 \end{pmatrix}, \quad (\text{B.8})$$

where  $\mathbb{Z}_0$  is an  $N_{\text{basis}} \times N_{\text{basis}}$  matrix. If  $SU(2)$  symmetry is present,  $\mathbb{Z}_0$  is Hermitian. The SD wave function is in block diagonal form

$$\phi = \begin{pmatrix} \phi_\uparrow & 0 \\ 0 & \phi_\downarrow \end{pmatrix}, \quad (\text{B.9})$$

where  $\phi_\uparrow$  and  $\phi_\downarrow$  are  $N_{\text{basis}} \times M/2$  matrices.

The overlap between the HFB and SD is reduced to a determinant

$$\langle \psi | \phi \rangle = (-1)^{M/2(M/2-1)/2} \det(\phi_\downarrow^T \mathbb{Z}_0^\dagger \phi_\uparrow), \quad (\text{B.10})$$

which can be calculated efficiently. Note that we can ignore the overall sign here if the number of particles is fixed in the calculation. If we set  $Q_0 = \phi_\downarrow^T \mathbb{Z}_0^\dagger \phi_\uparrow$ , the nonzero Green's functions are

$$\begin{aligned} \frac{\langle \psi | c_{i\uparrow}^\dagger c_{j\uparrow} | \phi \rangle}{\langle \psi | \phi \rangle} &= (\mathbb{Z}_0^* \phi_\downarrow (Q_0^T)^{-1} \phi_\uparrow^T)_{ij}, \\ \frac{\langle \psi | c_{i\downarrow}^\dagger c_{j\downarrow} | \phi \rangle}{\langle \psi | \phi \rangle} &= (\mathbb{Z}_0^\dagger \phi_\uparrow Q_0^{-1} \phi_\downarrow^T)_{ij}, \\ \frac{\langle \psi | c_{i\uparrow} c_{j\downarrow} | \phi \rangle}{\langle \psi | \phi \rangle} &= (-\phi_\uparrow Q_0^{-1} \phi_\downarrow^T)_{ij}, \\ \frac{\langle \psi | c_{i\uparrow}^\dagger c_{j\downarrow}^\dagger | \phi \rangle}{\langle \psi | \phi \rangle} &= (\mathbb{Z}_0^* - \mathbb{Z}_0^* \phi_\downarrow (Q_0^T)^{-1} \phi_\uparrow^T \mathbb{Z}_0^*)_{ij}. \end{aligned} \quad (\text{B.11})$$

The corresponding projected HFB wave function is similar to Eq. (B.5),

$$|\psi_{\text{PHFB}}\rangle = \frac{1}{(M/2)!} (c_\uparrow^\dagger Z_0 c_\downarrow^\dagger)^{M/2} |0\rangle, \quad (\text{B.12})$$

where  $c_\uparrow^\dagger$  and  $c_\downarrow^\dagger$  are the same as  $c^\dagger$  except for the spin index. The general operator in Eq. (A.1) has the form

$$t = \begin{pmatrix} t_\uparrow & 0 \\ 0 & t_\downarrow \end{pmatrix}, \quad (\text{B.13})$$

with  $\Delta$  and  $\tilde{\Delta}$  equal to zero again. After propagation, the new  $Z'_0$  is given by

$$Z'_0 = \exp(t_\uparrow) Z_0 \exp(t_\downarrow^T). \quad (\text{B.14})$$

For a system with  $SU(2)$  symmetry, we have  $t_\uparrow = t_\downarrow^*$  and  $Z_0 = U_0 D_0 U_0^\dagger$ , where  $U_0$  is a unitary matrix and  $D_0$  is a diagonal matrix. The propagation is

$$Z'_0 = (\exp(t_\uparrow) U_0) D_0 (\exp(t_\uparrow) U_0)^\dagger, \quad (\text{B.15})$$

and  $Z'_0$  will remain Hermitian. The propagation can be thought of as  $U'_0 = \exp(t_\uparrow) U_0$ , which is similar to propagating an SD wave function. Note that maintaining numerical stability in the propagation will likely require additional investigation in these situations.

## APPENDIX C

# Generalized Metropolis with Force Bias

In this appendix, we describe our second approach using the generalized Metropolis procedure to accelerate the sampling of paths in auxiliary field (AF) space. We introduce a dynamic force bias, analogous to what is employed in the branching random walk methods in constrained path or phase-free AFQMC [14], in proposing the updates of the field values, which improves the acceptance ratio and hence the MC efficiency.

To facilitate the description of the sampling algorithm we first give a brief sketch of the standard path-integral AFQMC approach, on which more detailed descriptions can be found in, for example, Refs. [50] and [14]. Ground state AFQMC measures the static properties by

$$\langle \hat{O} \rangle = \frac{\langle \psi_T | \exp(-\beta \hat{H}/2) \hat{O} \exp(-\beta \hat{H}/2) | \psi_T \rangle}{\langle \psi_T | \exp(-\beta \hat{H}) | \psi_T \rangle}, \quad (\text{C.1})$$

where the Hamiltonian  $\hat{H} \equiv \hat{K} + \hat{V}$  is given by Eq. (6.1). We apply the usual Trotter-Suzuki breakup

$$e^{-\Delta\tau\hat{H}} \simeq e^{-\Delta\tau\hat{K}/2} e^{-\Delta\tau\hat{V}} e^{-\Delta\tau\hat{K}/2} \quad (\text{C.2})$$

and the HS decomposition [38]

$$\begin{aligned} e^{\Delta\tau U n_{i\uparrow} n_{i\downarrow}} &= \frac{1}{2} \sum_{x_i=\pm 1} e^{(\gamma x_i - \Delta\tau U/2)(n_{i\uparrow} + n_{i\downarrow} - 1)} \\ &\equiv \frac{1}{2} \sum_{x_i=\pm 1} \hat{b}_i(x_i), \end{aligned} \quad (\text{C.3})$$

with  $\cosh(\gamma) = \exp(-\Delta\tau U/2)$ , arriving at the form

$$e^{-\Delta\tau \hat{H}} = \int d\mathbf{x} p(\mathbf{x}) \hat{B}(\mathbf{x}), \quad (\text{C.4})$$

where  $\mathbf{x} = \{x_1, x_2, \dots, x_{N_s}\}$ . The probability density function  $p(\mathbf{x})$  is uniform for the  $2^{N_s}$  AF configurations under the choice of HS in Eq. (C.3), and the one-body propagator is  $\hat{B}(\mathbf{x}) = e^{-\Delta\tau \hat{K}/2} \prod_i \hat{b}_i(x_i) e^{-\Delta\tau \hat{K}/2}$ .

The expression in Eq. (C.1) is then re-written as a path integral of  $M \equiv \beta/\Delta\tau$  time slices. Let us consider the  $l$ -th time slice, and introduce the notation

$$\begin{aligned} \langle \psi_l | &= \langle \psi_T | \hat{B}(\mathbf{x}^{(M)}) \hat{B}(\mathbf{x}^{(M-1)}) \cdots \hat{B}(\mathbf{x}^{(l+1)}) e^{-\Delta\tau \hat{K}/2} \\ |\psi_r\rangle &= e^{-\Delta\tau \hat{K}/2} \hat{B}(\mathbf{x}^{(l-1)}) \hat{B}(\mathbf{x}^{(l-2)}) \cdots \hat{B}(\mathbf{x}^{(1)}) |\psi_T\rangle, \end{aligned}$$

which are both single Slater determinant wave functions if we choose  $|\psi_T\rangle$  to be a Slater determinant. The integrand of the path-integral in the denominator of Eq. (C.1) then becomes

$$\mathcal{W}(\mathbf{x}) = p(\mathbf{x}) \langle \psi_l | \prod_{i=1}^{N_s} \hat{b}_i(x_i) | \psi_r \rangle, \quad (\text{C.5})$$

where  $\mathbf{x}$  denotes the collection of AF at time slice  $l$ . In the standard way of sampling  $\mathcal{W}$ , one proposes to flip each auxiliary-field  $x_i$  one by one, and sweeps through  $\mathbf{x}$ . We will update the entire configuration  $\mathbf{x}$  (or a sub-cluster of  $\mathbf{x}$  for very large system sizes),

simultaneously. We define a force bias [14]:

$$\bar{n}_{i\sigma} = \frac{\langle \psi_l | n_{i\sigma} | \psi_r \rangle}{\langle \psi_l | \psi_r \rangle}, \quad (\text{C.6})$$

and propose updates of the fields with the probability density:

$$\mathcal{P}(\mathbf{x}) \propto p(\mathbf{x}) \prod_{i=1}^{\mathcal{N}_s} e^{\gamma x_i (\bar{n}_{i\uparrow} + \bar{n}_{i\downarrow} - 1)} \quad (\text{C.7})$$

which can be sampled directly. Detailed balance then leads to a Metropolis acceptance probability given by

$$\mathcal{A}(\mathbf{x} \rightarrow \mathbf{x}') = \min\left\{1, \frac{\mathcal{W}(\mathbf{x}') \mathcal{P}(\mathbf{x})}{\mathcal{W}(\mathbf{x}) \mathcal{P}(\mathbf{x}')}\right\}. \quad (\text{C.8})$$

Note that the probability function for proposing transitions does not depend on the “current” configuration of AF, i.e.,  $\mathcal{P}(\mathbf{x} \rightarrow \mathbf{x}') = \mathcal{P}(\mathbf{x}')$ . If  $\mathcal{P} = W$ , all updates will be accepted. Because of the force bias,  $\mathcal{P}$  approximates  $\mathcal{W}$  up to  $\mathcal{O}(\sqrt{\Delta\tau})$ , leading to typically high acceptance ratio.

Although we have used the discrete charge HS decomposition, the algorithm generalizes straightforwardly to continuous HS transformations. We comment that the use of the dynamic force bias in Eq. (C.6) effectively introduces a background subtraction [69, 14] in the decomposition of Eq. (C.3). That is, if one were to employ the standard updating algorithms *without the force bias*, one would find Eq. (C.3) much less efficient than a continuous charge decomposition which subtracts a constant background. This discrepancy in efficiency grows more as the system density decreases, which is especially relevant since the systems studied here are at the low density limit. (See Ref. [69] for an analysis of the efficiency of HS transformations, and Ref. [30] for discussion on how the dynamic force bias automatically introduces an optimal constant background shift.)

Some other features of our algorithm are:

- Since we always work in the dilute limit, the memory is saved by only storing the wave function and calculating the Green function on the fly. We divide the path of  $M$  slices into  $\sqrt{M}$  blocks, and only track one block each time. The wave function at the beginning of each block is stored. The largest number of wave functions stored in our code is  $\sim 2\sqrt{M}$ .
- The wave function is transformed between real and momentum space by fast Fourier transformation, so that all the one-body operators during projection are diagonal, and Green functions in different space are easily obtained.
- When we only need the energy, we separate it into kinetic and potential energy. They are diagonal either in momentum or real space, where we do not need to calculate the whole Green function. To improve statistics, we measure the energy anywhere along the path and combine them, including the mixed estimator on both side.
- The standard determinantal QMC formalism as sketched above turns out to have a divergence of the Monte Carlo variance. We discuss the variance problem and its solution separately in chapter 4. The solution involves the introduction of a bridge link, which we have implemented in the calculations presented here. The force bias and basic sampling algorithm described above remain unchanged.

## APPENDIX D

# Extrapolation to the Continuum Limit in Fermi Gases

We have described the extrapolation procedure of our lattice results to the continuum limit, and the subsequent analysis to reach the thermodynamic limit. Here we illustrate the finite size extrapolation in few-body systems.

The extrapolation to the continuum limit, for a fixed number of particles, must be consistent and independent of the type of kinetic energy dispersion. For a two-body problem on the lattice, exact results can be obtained for large system sizes by mapping to a one-body problem in the center of mass system. The results are shown in Fig. D.1(a), which fit well a 4th-order polynomial function in  $1/L$ . We see from the inset that the coefficient on the linear term is zero within numerical precision.

We also show the finite size effect in the four-body problem from QMC, in Fig. D.1(b), reaching large lattice sizes. The same general behavior is seen as in the two-body problem. We have also studied the finite-size behavior of the BCS solution, finding similar trends but with different slopes. In the many-body system, our QMC data are consistent with

these observations as well. They are thus fitted with a 4th-order polynomial function with a vanishing  $1/L$  coefficient, as described in the main text.

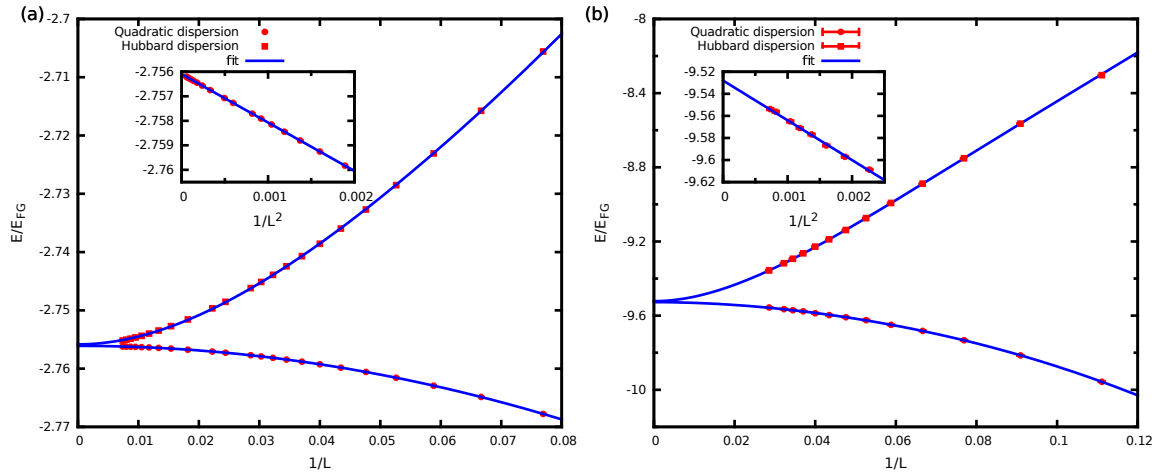


FIG. D.1: Extrapolation of finite-size lattice to the continuum limit in few body problems. Panel (a) shows exact diagonalization results for the two-body problem at  $\ln(ak_F) = 0.5$ , while panel (b) shows QMC solutions for the four-body problem at  $\ln(ak_F) = 0.0$ . In each case, results are obtained for both the Hubbard and the quadratic dispersions. A 4th-order polynomial function in  $1/L$  fits well both dispersions, and the extrapolated results in continuum limit agree well with each other. The insets indicate that the coefficients on  $1/L$  are negligible in both cases.

## BIBLIOGRAPHY

- [1] J. G. Bednorz and K. A. Müller, Z. Phys. B **64**, 189 (1986).
- [2] E. Dagotto, Science **309**, 257 (2005).
- [3] M. H. Y. Kamihara, T. Watanabe and H. Hosono, J. Am. Chem. Soc. **130**, 3296 (2008).
- [4] G. R. Stewart, Rev. Mod. Phys. **83**, 1539 (2011).
- [5] W. L. McMillan, Phys. Rev. **138**, A442 (1965).
- [6] D. Ceperley, G. V. Chester, and M. H. Kalos, Phys. Rev. B **16**, 3081 (1977).
- [7] C. J. Umrigar, K. G. Wilson, and J. W. Wilkins, Phys. Rev. Lett. **60**, 1719 (1988).
- [8] R. J. Bartlett and M. Musiał, Rev. Mod. Phys. **79**, 291 (pages 62) (2007).
- [9] S. R. White, Phys. Rev. Lett. **69**, 2863 (1992).
- [10] U. Schollwöck, Rev. Mod. Phys. **77**, 259 (2005).
- [11] U. Schollwöck, Ann. Phys. **326**, 96 (2011).
- [12] R. Blankenbecler, D. J. Scalapino, and R. L. Sugar, Phys. Rev. D **24**, 2278 (1981).
- [13] G. Sugiyama and S. Koonin, Annals of Physics **168**, 1 (1986).

- [14] S. Zhang, chapter in the OpenAccess book, Emergent Phenomena in Correlated Matter: Modeling and Simulation Vol 3, Eds. E. Pavarini and E. Koch and U. Schollwöck, <http://www.cond-mat.de/events/correl13> (2013).
- [15] S. Zhang, J. Carlson, and J. E. Gubernatis, Phys. Rev. B **55**, 7464 (1997).
- [16] E. Y. Loh, J. E. Gubernatis, R. T. Scalettar, S. R. White, D. J. Scalapino, and R. L. Sugar, Phys. Rev. B **41**, 9301 (1990).
- [17] S. Chandrasekharan and U.-J. Wiese, Phys. Rev. Lett. **83**, 3116 (1999), URL <http://link.aps.org/doi/10.1103/PhysRevLett.83.3116>.
- [18] Z. Y. Meng, T. C. Lang, S. Wessel, F. F. Assaad, and A. Muramatsu, Nature **464**, 847 (2010), ISSN 0028-0836, URL <http://dx.doi.org/10.1038/nature08942>.
- [19] S. Sorella, Y. Otsuka, and S. Yunoki, Scientific reports **2** (2012).
- [20] M. Hohenadler, T. C. Lang, and F. F. Assaad, Phys. Rev. Lett. **106**, 100403 (2011), URL <http://link.aps.org/doi/10.1103/PhysRevLett.106.100403>.
- [21] Z.-X. Li, Y.-F. Jiang, and H. Yao, Phys. Rev. B **91**, 241117 (2015), URL <http://link.aps.org/doi/10.1103/PhysRevB.91.241117>.
- [22] L. Wang, M. Iazzi, P. Corboz, and M. Troyer, Phys. Rev. B **91**, 235151 (2015), URL <http://link.aps.org/doi/10.1103/PhysRevB.91.235151>.
- [23] K. G. Wilson, Phys. Rev. D **10**, 2445 (1974), URL <http://link.aps.org/doi/10.1103/PhysRevD.10.2445>.
- [24] A. Bazavov, D. Toussaint, C. Bernard, J. Laiho, C. DeTar, L. Levkova, M. B. Oktay, S. Gottlieb, U. M. Heller, J. E. Hetrick, et al., Rev. Mod. Phys. **82**, 1349 (2010), URL <http://link.aps.org/doi/10.1103/RevModPhys.82.1349>.

- [25] P. Petreczky, Journal of Physics G: Nuclear and Particle Physics **39**, 093002 (2012), URL <http://stacks.iop.org/0954-3899/39/i=9/a=093002>.
- [26] C. Wu and S.-C. Zhang, Phys. Rev. B **71**, 155115 (2005), URL <http://link.aps.org/doi/10.1103/PhysRevB.71.155115>.
- [27] L. Wang, Y.-H. Liu, M. Iazzi, M. Troyer, and G. Harcos, Phys. Rev. Lett. **115**, 250601 (2015), URL <http://link.aps.org/doi/10.1103/PhysRevLett.115.250601>.
- [28] H. Shi, P. Rosenberg, S. Chiesa, and S. Zhang, Phys. Rev. Lett. **117**, 040401 (2016), URL <http://link.aps.org/doi/10.1103/PhysRevLett.117.040401>.
- [29] S. Zhang and H. Krakauer, Phys. Rev. Lett. **90**, 136401 (2003).
- [30] W. Purwanto and S. Zhang, Phys. Rev. E **70**, 056702 (2004).
- [31] W. A. Al-Saidi, S. Zhang, and H. Krakauer, J. Chem. Phys. **124**, 224101 (2006).
- [32] J. P. F. LeBlanc, A. E. Antipov, F. Becca, I. W. Bulik, G. K.-L. Chan, C.-M. Chung, Y. Deng, M. Ferrero, T. M. Henderson, C. A. Jiménez-Hoyos, et al. (Simons Collaboration on the Many-Electron Problem), Phys. Rev. X **5**, 041041 (2015), URL <http://link.aps.org/doi/10.1103/PhysRevX.5.041041>.
- [33] J. Hubbard, Proc. R. Soc. London Ser. A **276**, 238 (1963).
- [34] H. F. Trotter, Proc. Am. Math. Soc. **10**, 545 (1959).
- [35] M. Suzuki, Communications in Mathematical Physics **51**, 183 (1976).
- [36] S. Sorella, Phys. Rev. B **84**, 241110 (2011).
- [37] J. Hubbard, Phys. Rev. Lett. **3**, 77 (1959).

- [38] J. E. Hirsch, Phys. Rev. B **28**, 4059 (1983).
- [39] N. Metropolis, A. W. Rosenbluth, M. N. Rosenbluth, A. H. Teller, and E. Teller, The Journal of Chemical Physics **21**, 1087 (1953).
- [40] S. Jacobi and R. Baer, The Journal of Chemical Physics **120**, 43 (2004).
- [41] W. Purwanto, H. Krakauer, and S. Zhang, Phys. Rev. B **80**, 214116 (2009).
- [42] D. R. Hamann and S. B. Fahy, Phys. Rev. B **41**, 11352 (1990).
- [43] M. Calandra Buonaura and S. Sorella, Phys. Rev. B **57**, 11446 (1998).
- [44] S. R. White, D. J. Scalapino, R. L. Sugar, E. Y. Loh, J. E. Gubernatis, and R. T. Scalettar, Phys. Rev. B **40**, 506 (1989).
- [45] R. T. Scalettar, R. M. Noack, and R. R. P. Singh, Phys. Rev. B **44**, 10502 (1991).
- [46] J. Carlson, J. E. Gubernatis, G. Ortiz, and S. Zhang, Phys. Rev. B **59**, 12788 (1999).
- [47] C.-C. Chang and S. Zhang, Phys. Rev. B **78**, 165101 (2008).
- [48] M. Qin, H. Shi, and S. Zhang, Phys. Rev. B **94**, 235119 (2016), URL <http://link.aps.org/doi/10.1103/PhysRevB.94.235119>.
- [49] D. M. Ceperley and B. J. Alder, The Journal of Chemical Physics **81**, 5833 (1984).
- [50] F. F. Assaad, *Quantum Monte Carlo Methods on Lattices: The Determinantal method.*, Lecture notes of the Winter School on Quantum Simulations of Complex Many-Body Systems: From Theory to Algorithms. Publication Series of the John von Neumann Institute for Computing (NIC). NIC series Vol. 10. ISBN 3-00-009057-6 Pages 99-155.
- [51] W. Purwanto and S. Zhang, Phys. Rev. A **72**, 053610 (2005).

- [52] R. Baer, M. Head-Gordon, and D. Neuhauser, *The Journal of Chemical Physics* **109**, 6219 (1998).
- [53] G. M. Buendia, *Phys. Rev. B* **33**, 3519 (1986).
- [54] J. Carlson, S. Gandolfi, K. E. Schmidt, and S. Zhang, *Phys. Rev. A* **84**, 061602 (2011).
- [55] R. Rodríguez-Guzmán, K. W. Schmid, C. A. Jiménez-Hoyos, and G. E. Scuseria, *Phys. Rev. B* **85**, 245130 (2012).
- [56] H. Shi, C. A. Jiménez-Hoyos, R. Rodríguez-Guzmán, G. E. Scuseria, and S. Zhang, *Phys. Rev. B* **89**, 125129 (2014), URL <http://link.aps.org/doi/10.1103/PhysRevB.89.125129>.
- [57] W. Purwanto, W. A. Al-Saidi, H. Krakauer, and S. Zhang, *The Journal of Chemical Physics* **128**, 114309 (pages 7) (2008).
- [58] S. Zhang, *Phys. Rev. Lett.* **83**, 2777 (1999).
- [59] J. E. Hirsch, *Phys. Rev. B* **31**, 4403 (1985), URL <http://link.aps.org/doi/10.1103/PhysRevB.31.4403>.
- [60] C. J. Umrigar, *The Journal of Chemical Physics* **143**, 164105 (2015), URL <http://scitation.aip.org/content/aip/journal/jcp/143/16/10.1063/1.4933112>.
- [61] M. Boninsegni, N. V. Prokof'ev, and B. V. Svistunov, *Phys. Rev. E* **74**, 036701 (2006), URL <http://link.aps.org/doi/10.1103/PhysRevE.74.036701>.
- [62] J. Carlson and M. H. Kalos, *Phys. Rev. C* **32**, 1735 (1985), URL <http://link.aps.org/doi/10.1103/PhysRevC.32.1735>.

- [63] W. M. C. Foulkes, L. Mitas, R. J. Needs, and G. Rajagopal, Rev. Mod. Phys. **73**, 33 (2001), URL <http://link.aps.org/doi/10.1103/RevModPhys.73.33>.
- [64] C. J. Umrigar, M. P. Nightingale, and K. J. Runge, J. Chem. Phys. **99**, 2865 (1993).
- [65] D. M. Ceperley and B. J. Alder, Phys. Rev. Lett. **45**, 566 (1980), URL <http://link.aps.org/doi/10.1103/PhysRevLett.45.566>.
- [66] S. Moroni, S. Saccani, and C. Filippi, Journal of chemical theory and computation **10**, 4823 (2014).
- [67] R. R. d. Santos, Brazilian Journal of Physics **33**, 36 (2003), ISSN 0103-9733.
- [68] A. Georges, G. Kotliar, W. Krauth, and M. J. Rozenberg, Rev. Mod. Phys. **68**, 13 (1996), URL <http://link.aps.org/doi/10.1103/RevModPhys.68.13>.
- [69] H. Shi and S. Zhang, Phys. Rev. B **88**, 125132 (2013), URL <http://link.aps.org/doi/10.1103/PhysRevB.88.125132>.
- [70] D. M. Ceperley, Rev. Mod. Phys. **67**, 279 (1995), URL <http://link.aps.org/doi/10.1103/RevModPhys.67.279>.
- [71] P. Ring and P. Schuck, *The Nuclear Many-Body Problem* (SpringerVerlag, New York, 1980).
- [72] G. E. Scuseria, C. A. Jimnez-Hoyos, T. M. Henderson, K. Samanta, and J. K. Ellis, The Journal of Chemical Physics **135**, 124108 (2011), URL <http://scitation.aip.org/content/aip/journal/jcp/135/12/10.1063/1.3643338>.
- [73] G. F. Bertsch and L. M. Robledo, Phys. Rev. Lett. **108**, 042505 (2012), URL <http://link.aps.org/doi/10.1103/PhysRevLett.108.042505>.

- [74] D. Tahara and M. Imada, Journal of the Physical Society of Japan **77**, 114701 (2008), <http://dx.doi.org/10.1143/JPSJ.77.114701>, URL <http://dx.doi.org/10.1143/JPSJ.77.114701>.
- [75] T. M. Henderson, G. E. Scuseria, J. Dukelsky, A. Signoracci, and T. Duguet, Phys. Rev. C **89**, 054305 (2014), URL <http://link.aps.org/doi/10.1103/PhysRevC.89.054305>.
- [76] H. Shi and S. Zhang, Phys. Rev. B **95**, 045144 (2017), URL <http://link.aps.org/doi/10.1103/PhysRevB.95.045144>.
- [77] H. Shi, S. Chiesa, and S. Zhang, Phys. Rev. A **92**, 033603 (2015), URL <http://link.aps.org/doi/10.1103/PhysRevA.92.033603>.
- [78] J. Bonnard and O. Juillet, Phys. Rev. Lett. **111**, 012502 (2013), URL <http://link.aps.org/doi/10.1103/PhysRevLett.111.012502>.
- [79] S. Zhang, J. Carlson, and J. E. Gubernatis, Phys. Rev. Lett. **74**, 3652 (1995).
- [80] L. M. Robledo, Phys. Rev. C **79**, 021302 (2009), URL <http://link.aps.org/doi/10.1103/PhysRevC.79.021302>.
- [81] C. Gonzlez-Ballesteros, L. Robledo, and G. Bertsch, Computer Physics Communications **182**, 2213 (2011), ISSN 0010-4655, URL <http://www.sciencedirect.com/science/article/pii/S0010465511001627>.
- [82] N. Onishi and S. Yoshida, Nuclear Physics **80**, 367 (1966), ISSN 0029-5582, URL <http://www.sciencedirect.com/science/article/pii/0029558266900964>.
- [83] R. Balian and E. Brezin, Il Nuovo Cimento B (1965-1970) **64**, 37 (1969), ISSN 1826-9877, URL <http://dx.doi.org/10.1007/BF02710281>.

- [84] A. Y. Kitaev, Physics-Uspekhi **44**, 131 (2001).
- [85] H. Shi and S. Zhang, Phys. Rev. E **93**, 033303 (2016), URL <http://link.aps.org/doi/10.1103/PhysRevE.93.033303>.
- [86] D. Wang, Y. Li, Z. Cai, Z. Zhou, Y. Wang, and C. Wu, Phys. Rev. Lett. **112**, 156403 (2014), URL <http://link.aps.org/doi/10.1103/PhysRevLett.112.156403>.
- [87] F. F. Assaad and I. F. Herbut, Phys. Rev. X **3**, 031010 (2013), URL <http://link.aps.org/doi/10.1103/PhysRevX.3.031010>.
- [88] S. Giorgini, L. P. Pitaevskii, and S. Stringari, Rev. Mod. Phys. **80**, 1215 (2008), URL <http://link.aps.org/doi/10.1103/RevModPhys.80.1215>.
- [89] I. Bloch, J. Dalibard, and W. Zwerger, Rev. Mod. Phys. **80**, 885 (2008).
- [90] See, e.g., W. Ketterle and M. W. Zwierlein, *Making, probing and understanding ultracold Fermi gases*, in Ultracold Fermi Gases, Proceedings of the International School of Physics “Enrico Fermi”, Course CLXIV, Varenna, 20 - 30 June (2006), arXiv:0801.2500.
- [91] L. Luo and J. Thomas, Journal of Low Temperature Physics **154**, 1 (2009), ISSN 0022-2291.
- [92] M. J. H. Ku, A. T. Sommer, L. W. Cheuk, and M. W. Zwierlein, Science **335**, 563 (2012), <http://www.sciencemag.org/content/335/6068/563.full.pdf>, URL <http://www.sciencemag.org/content/335/6068/563.abstract>.
- [93] Y. Nishida, Phys. Rev. A **79**, 013627 (2009), URL <http://link.aps.org/doi/10.1103/PhysRevA.79.013627>.

- [94] M. G. Endres, D. B. Kaplan, J.-W. Lee, and A. N. Nicholson, Phys. Rev. A **87**, 023615 (2013), URL <http://link.aps.org/doi/10.1103/PhysRevA.87.023615>.
- [95] D. S. Petrov, M. A. Baranov, and G. V. Shlyapnikov, Phys. Rev. A **67**, 031601 (2003), URL <http://link.aps.org/doi/10.1103/PhysRevA.67.031601>.
- [96] S. S. Botelho and C. A. R. Sá de Melo, Phys. Rev. Lett. **96**, 040404 (2006), URL <http://link.aps.org/doi/10.1103/PhysRevLett.96.040404>.
- [97] W. Zhang, G.-D. Lin, and L.-M. Duan, Phys. Rev. A **78**, 043617 (2008), URL <http://link.aps.org/doi/10.1103/PhysRevA.78.043617>.
- [98] J.-P. Martikainen and P. Törmä, Phys. Rev. Lett. **95**, 170407 (2005), URL <http://link.aps.org/doi/10.1103/PhysRevLett.95.170407>.
- [99] W. Zhang, G.-D. Lin, and L.-M. Duan, Phys. Rev. A **77**, 063613 (2008), URL <http://link.aps.org/doi/10.1103/PhysRevA.77.063613>.
- [100] J. Tempere, M. Wouters, and J. T. Devreese, Phys. Rev. B **75**, 184526 (2007), URL <http://link.aps.org/doi/10.1103/PhysRevB.75.184526>.
- [101] G. J. Conduit, P. H. Conlon, and B. D. Simons, Phys. Rev. A **77**, 053617 (2008), URL <http://link.aps.org/doi/10.1103/PhysRevA.77.053617>.
- [102] G. Bertaina and S. Giorgini, Phys. Rev. Lett. **106**, 110403 (2011), URL <http://link.aps.org/doi/10.1103/PhysRevLett.106.110403>.
- [103] A. A. Orel, P. Dyke, M. Delehaye, C. J. Vale, and H. Hu, New Journal of Physics **13**, 113032 (2011), URL <http://stacks.iop.org/1367-2630/13/i=11/a=113032>.
- [104] K. Martiyanova, V. Makhalov, and A. Turlapov, Phys. Rev. Lett. **105**, 030404 (2010), URL <http://link.aps.org/doi/10.1103/PhysRevLett.105.030404>.

- [105] J. B. Anderson, *The Journal of Chemical Physics* **65**, 4121 (1976).
- [106] F. Werner and Y. Castin, *Phys. Rev. A* **86**, 013626 (2012), URL <http://link.aps.org/doi/10.1103/PhysRevA.86.013626>.
- [107] V. Makhlov, K. Martiyanov, and A. Turlapov, *Phys. Rev. Lett.* **112**, 045301 (2014), URL <http://link.aps.org/doi/10.1103/PhysRevLett.112.045301>.
- [108] M. Bauer, M. M. Parish, and T. Enss, *Phys. Rev. Lett.* **112**, 135302 (2014), URL <http://link.aps.org/doi/10.1103/PhysRevLett.112.135302>.
- [109] J. Levinsen and M. M. Parish, ArXiv e-prints (2014), [1408.2737](https://arxiv.org/abs/1408.2737).
- [110] J. R. Engelbrecht, M. Randeria, and L. Zhang, *Phys. Rev. B* **45**, 10135 (1992), URL <http://link.aps.org/doi/10.1103/PhysRevB.45.10135>.
- [111] L. He, *Phys. Rev. A* **90**, 053633 (2014), URL <http://link.aps.org/doi/10.1103/PhysRevA.90.053633>.
- [112] S. Tan, *Annals of Physics* **323**, 2952 (2008), ISSN 0003-4916, URL <http://www.sciencedirect.com/science/article/pii/S0003491608000456>.
- [113] S. Tan, *Annals of Physics* **323**, 2971 (2008), ISSN 0003-4916, URL <http://www.sciencedirect.com/science/article/pii/S0003491608000432>.
- [114] Y. Sagi, T. E. Drake, R. Paudel, and D. S. Jin, *Phys. Rev. Lett.* **109**, 220402 (2012), URL <http://link.aps.org/doi/10.1103/PhysRevLett.109.220402>.
- [115] R. J. Wild, P. Makotyn, J. M. Pino, E. A. Cornell, and D. S. Jin, *Phys. Rev. Lett.* **108**, 145305 (2012), URL <http://link.aps.org/doi/10.1103/PhysRevLett.108.145305>.

- [116] J. E. Drut, T. A. Lähde, and T. Ten, Phys. Rev. Lett. **106**, 205302 (2011), URL <http://link.aps.org/doi/10.1103/PhysRevLett.106.205302>.
- [117] C. N. Yang, Rev. Mod. Phys. **34**, 694 (1962), URL <http://link.aps.org/doi/10.1103/RevModPhys.34.694>.
- [118] M. Schick, Phys. Rev. A **3**, 1067 (1971), URL <http://link.aps.org/doi/10.1103/PhysRevA.3.1067>.
- [119] See, e.g., A. Bulgac, Superfluid Local Density Approximation: A Density Functional Theory Approach to the Nuclear Pairing Problem, chapter in "Fifty Years of Nuclear BCS", eds. R.A. Broglia and V. Zelevinsky, p. 100 (Singapore, World Scientific, 2013), arXiv:1204.2207.
- [120] Y.-J. Lin, R. L. Compton, K. Jimenez-Garcia, J. V. Porto, and I. B. Spielman, Nature **462**, 628 (2009), URL <http://dx.doi.org/10.1038/nature08609>.
- [121] Y.-J. Lin, K. Jimenez-Garcia, and I. B. Spielman, Nature **471**, 83 (2011), URL <http://dx.doi.org/10.1038/nature09887>.
- [122] L. W. Cheuk, A. T. Sommer, Z. Hadzibabic, T. Yefsah, W. S. Bakr, and M. W. Zwierlein, Phys. Rev. Lett. **109**, 095302 (2012), URL <http://link.aps.org/doi/10.1103/PhysRevLett.109.095302>.
- [123] P. Wang, Z.-Q. Yu, Z. Fu, J. Miao, L. Huang, S. Chai, H. Zhai, and J. Zhang, Phys. Rev. Lett. **109**, 095301 (2012), URL <http://link.aps.org/doi/10.1103/PhysRevLett.109.095301>.
- [124] L. Huang, Z. Meng, P. Wang, P. Peng, S.-L. Zhang, L. Chen, D. Li, Q. Zhou, and J. Zhang, Nature Physics **12**, 540 (2016), ISSN 1745-2473, URL <http://dx.doi.org/10.1038/nphys3672>.

- [125] T. D. Stanescu, C. Zhang, and V. Galitski, Phys. Rev. Lett. **99**, 110403 (2007), URL <http://link.aps.org/doi/10.1103/PhysRevLett.99.110403>.
- [126] G. Juzeliūnas, J. Ruseckas, and J. Dalibard, Phys. Rev. A **81**, 053403 (2010), URL <http://link.aps.org/doi/10.1103/PhysRevA.81.053403>.
- [127] G. Juzeliūnas, J. Ruseckas, M. Lindberg, L. Santos, and P. Öhberg, Phys. Rev. A **77**, 011802 (2008), URL <http://link.aps.org/doi/10.1103/PhysRevA.77.011802>.
- [128] D. L. Campbell, G. Juzeliūnas, and I. B. Spielman, Phys. Rev. A **84**, 025602 (2011), URL <http://link.aps.org/doi/10.1103/PhysRevA.84.025602>.
- [129] J. D. Sau, R. Sensarma, S. Powell, I. B. Spielman, and S. Das Sarma, Phys. Rev. B **83**, 140510 (2011), URL <http://link.aps.org/doi/10.1103/PhysRevB.83.140510>.
- [130] B. M. Anderson, I. B. Spielman, and G. Juzeliūnas, Phys. Rev. Lett. **111**, 125301 (2013), URL <http://link.aps.org/doi/10.1103/PhysRevLett.111.125301>.
- [131] Z.-F. Xu, L. You, and M. Ueda, Phys. Rev. A **87**, 063634 (2013), URL <http://link.aps.org/doi/10.1103/PhysRevA.87.063634>.
- [132] D. L. Campbell and I. B. Spielman, New Journal of Physics **18**, 033035 (2016), URL <http://stacks.iop.org/1367-2630/18/i=3/a=033035>.
- [133] G. Chen, M. Gong, and C. Zhang, Phys. Rev. A **85**, 013601 (2012), URL <http://link.aps.org/doi/10.1103/PhysRevA.85.013601>.
- [134] Z.-Q. Yu and H. Zhai, Phys. Rev. Lett. **107**, 195305 (2011), URL <http://link.aps.org/doi/10.1103/PhysRevLett.107.195305>.

- [135] H. Hu, L. Jiang, X.-J. Liu, and H. Pu, Phys. Rev. Lett. **107**, 195304 (2011), URL <http://link.aps.org/doi/10.1103/PhysRevLett.107.195304>.
- [136] L. He and X.-G. Huang, Phys. Rev. Lett. **108**, 145302 (2012), URL <http://link.aps.org/doi/10.1103/PhysRevLett.108.145302>.
- [137] J. P. Vyasanakere, S. Zhang, and V. B. Shenoy, Phys. Rev. B **84**, 014512 (2011), URL <http://link.aps.org/doi/10.1103/PhysRevB.84.014512>.
- [138] L. Han and C. A. R. Sá de Melo, Phys. Rev. A **85**, 011606 (2012), URL <http://link.aps.org/doi/10.1103/PhysRevA.85.011606>.
- [139] H.-K. Tang, X. Yang, J. Sun, and H.-Q. Lin, EPL (Europhysics Letters) **107**, 40003 (2014), URL <http://stacks.iop.org/0295-5075/107/i=4/a=40003>.
- [140] D. Podolsky and E. Demler, New Journal of Physics **7**, 59 (2005), URL <http://stacks.iop.org/1367-2630/7/i=1/a=059>.
- [141] D. Y. Qiu, T. Cao, and S. G. Louie, Phys. Rev. Lett. **115**, 176801 (2015), URL <http://link.aps.org/doi/10.1103/PhysRevLett.115.176801>.
- [142] H. Yu, G.-B. Liu, P. Gong, X. Xu, and W. Yao, Nat Commun **5** (2014), URL <http://dx.doi.org/10.1038/ncomms4876>.
- [143] E. McCann and V. I. Fal'ko, Phys. Rev. Lett. **96**, 086805 (2006), URL <http://link.aps.org/doi/10.1103/PhysRevLett.96.086805>.
- [144] H. Min, G. Borghi, M. Polini, and A. H. MacDonald, Phys. Rev. B **77**, 041407 (2008), URL <http://link.aps.org/doi/10.1103/PhysRevB.77.041407>.
- [145] M. Imada, A. Fujimori, and Y. Tokura, Rev. Mod. Phys. **70**, 1039 (1998), URL <http://link.aps.org/doi/10.1103/RevModPhys.70.1039>.

- [146] R. Peters and N. Kawakami, Phys. Rev. B **89**, 155134 (2014), URL <http://link.aps.org/doi/10.1103/PhysRevB.89.155134>.
- [147] E. Dagotto, Rev. Mod. Phys. **66**, 763 (1994), URL <http://link.aps.org/doi/10.1103/RevModPhys.66.763>.
- [148] E. H. Lieb and F. Y. Wu, Phys. Rev. Lett. **20**, 1445 (1968), URL <http://link.aps.org/doi/10.1103/PhysRevLett.20.1445>.
- [149] B.-X. Zheng, C.-M. Chung, P. Corboz, G. Ehlers, M.-P. Qin, R. M. Noack, H. Shi, S. R. White, S. Zhang, and G. Kin-Lic Chan, ArXiv e-prints (2017), 1701.00054.
- [150] L. F. Tocchio, F. Becca, A. Parola, and S. Sorella, Phys. Rev. B **78**, 041101 (2008), URL <http://link.aps.org/doi/10.1103/PhysRevB.78.041101>.
- [151] N. Trivedi and D. M. Ceperley, Phys. Rev. B **41**, 4552 (1990), URL <http://link.aps.org/doi/10.1103/PhysRevB.41.4552>.
- [152] R. Rodríguez-Guzmán, C. A. Jiménez-Hoyos, R. Schutski, and G. E. Scuseria, Phys. Rev. B **87**, 235129 (2013), URL <http://link.aps.org/doi/10.1103/PhysRevB.87.235129>.
- [153] R. J. Bartlett and M. Musiał, Rev. Mod. Phys. **79**, 291 (2007), URL <http://link.aps.org/doi/10.1103/RevModPhys.79.291>.
- [154] G. Knizia and G. K.-L. Chan, Phys. Rev. Lett. **109**, 186404 (2012), URL <http://link.aps.org/doi/10.1103/PhysRevLett.109.186404>.
- [155] T. Maier, M. Jarrell, T. Pruschke, and M. H. Hettler, Rev. Mod. Phys. **77**, 1027 (2005), URL <http://link.aps.org/doi/10.1103/RevModPhys.77.1027>.

- [156] A. N. Rubtsov, M. I. Katsnelson, and A. I. Lichtenstein, Phys. Rev. B **77**, 033101 (2008), URL <http://link.aps.org/doi/10.1103/PhysRevB.77.033101>.
- [157] N. Prokof'ev and B. Svistunov, Phys. Rev. Lett. **99**, 250201 (2007), URL <http://link.aps.org/doi/10.1103/PhysRevLett.99.250201>.
- [158] M. Qin, H. Shi, and S. Zhang, Phys. Rev. B **94**, 085103 (2016), URL <http://link.aps.org/doi/10.1103/PhysRevB.94.085103>.
- [159] A. H. MacDonald, S. M. Girvin, and D. Yoshioka, Phys. Rev. B **37**, 9753 (1988), URL <http://link.aps.org/doi/10.1103/PhysRevB.37.9753>.
- [160] D. S. Fisher, Phys. Rev. B **39**, 11783 (1989), URL <http://link.aps.org/doi/10.1103/PhysRevB.39.11783>.
- [161] H. Neuberger and T. Ziman, Phys. Rev. B **39**, 2608 (1989), URL <http://link.aps.org/doi/10.1103/PhysRevB.39.2608>.
- [162] A. W. Sandvik, Phys. Rev. B **56**, 11678 (1997), URL <http://link.aps.org/doi/10.1103/PhysRevB.56.11678>.
- [163] C. N. Varney, C.-R. Lee, Z. J. Bai, S. Chiesa, M. Jarrell, and R. T. Scalettar, Phys. Rev. B **80**, 075116 (2009), URL <http://link.aps.org/doi/10.1103/PhysRevB.80.075116>.
- [164] D. A. Huse, Phys. Rev. B **37**, 2380 (1988), URL <http://link.aps.org/doi/10.1103/PhysRevB.37.2380>.
- [165] A. Moreo, D. J. Scalapino, R. L. Sugar, S. R. White, and N. E. Bickers, Phys. Rev. B **41**, 2313 (1990), URL <http://link.aps.org/doi/10.1103/PhysRevB.41.2313>.

- [166] E. Fradkin, S. A. Kivelson, and J. M. Tranquada, Rev. Mod. Phys. **87**, 457 (2015), URL <http://link.aps.org/doi/10.1103/RevModPhys.87.457>.
- [167] C.-C. Chang and S. Zhang, Phys. Rev. Lett. **104**, 116402 (2010), URL <http://link.aps.org/doi/10.1103/PhysRevLett.104.116402>.
- [168] E. Vitali, H. Shi, M. Qin, and S. Zhang, Phys. Rev. B **94**, 085140 (2016), URL <http://link.aps.org/doi/10.1103/PhysRevB.94.085140>.
- [169] K. Hara and S. Iwasaki, Nuclear Physics A **332**, 61 (1979), ISSN 0375-9474, URL <http://www.sciencedirect.com/science/article/pii/0375947479900940>.

## VITA

### Hao Shi

Hao Shi was born in Rugao, China, on July 13, 1986. He is fascinated with science and math since he was a kid. In 2008, he graduated with a Bachelor of Science degree in Physics from Nanjing University in Nanjing, China. In the same year, he joined Renming University in Beijing, China to study computational physics. He entered the College of William and Mary and joined Dr. Shiwei Zhangs computational condensed matter physics group in Fall 2011. His research focuses on studying strongly correlated systems by Auxiliary Field Quantum Monte Carlo and other numerical methods. After graduation, he will work as a postdoctoral fellow at Center for Computational Quantum Physics in Flatiron Institute.